DUSTY STAR-FORMING GALAXIES WITHIN HIGH-REDSHIFT GALAXY CLUSTERS

Allison Germaine Noble

Doctor of Philosophy

Department of Physics
McGill University
Montréal, Québec
Canada

November 11, 2013

A Thesis submitted to McGill University
in partial fulfillment of the requirements of the degree of
Doctor of Philosophy

CONTENTS

ABSTRACT **xiii**

RÉSUMÉ **xiv**

ACKNOWLEDGMENTS **xv**

CONTRIBUTIONS OF AUTHORS **xvi**

1 INTRODUCTION **2**

1.1 Motivation 2

1.2 Environmental Trends 6

1.3 Infrared/Submillimetre Observations 9

1.3.1 Spectral Energy Distributions and the Negative k-correction . 13

2 METHODOLOGY **17**

2.1 Cluster Surveys 17

2.1.1 The Red-sequence Cluster Survey 19

2.1.2 The Spitzer Adaptation of the Red-sequence Cluster Survey . 21

2.2 Infrared Luminosity and Star Formation Rates 25

2.3 Stellar Masses 28

3 A KINEMATIC STUDY OF INFRARED GALAXIES IN A $z \sim 0.9$ CLUSTER **32**

3.1 Introduction 34

3.2 Observations and Data Reduction 37

3.2.1 The SpARCS Survey 37

3.2.2 SpARCS J161314+564930 and the GCLASS Cluster Sample . 37

3.2.3 Spitzer-MIPS Imaging 38

3.2.4 Source Detection and Photometry 38

3.3 Analysis 39

3.3.1 Counterpart Identification 39

3.3.2 Stellar Masses 40

3.3.3 $24\,\mu$m Star Formation Rates 41

3.3.4 Active Galactic Nucleus Contamination 42

3.4 Results 43

3.4.1 Age as a Function of Stellar Mass 43

3.4.2 Relative Velocity as a Function of Radius 44

3.4.3 Environmental Dependence on the Specific Star Formation Rate 46
3.4.4 The Correlation between Star Formation Rate and Stellar Mass 51
3.5 Discussion 56
3.5.1 Velocity Distributions of Two Star-Forming Populations . . . 58
3.5.2 Utilizing Caustic Diagrams as Accretion History Predictors . . 63
3.5.3 A Kinematic Approach to the Environmental Dependence on the Specific Star Formation Rate 67
3.6 Conclusions 70

4 A VIEW OF $z \sim 1.2$ CLUSTERS FROM *Herschel* 73
4.1 Introduction 74
4.2 Observations and Data Reduction 76
4.2.1 A $z \sim 1.2$ Sample from GCLASS 76
4.2.2 *Herschel*-PACS Imaging 76
4.2.3 *Herschel*-SPIRE Data 78
4.3 Analysis 81
4.3.1 PACS Stacking 81
4.3.2 PACS Aperture Photometry 82
4.3.3 SPIRE Stacking 85
4.4 Results and Discussion 87
4.4.1 Infrared Spectral Energy Distributions 87
4.4.2 Specific Star Formation Rate as a Function of Phase-Space . . 89
4.4.3 Dust Temperatures for Dynamically-Isolated Populations . . . 91
4.4.4 A Simple Interpretation for Quenching 96
4.5 Conclusions 101

5 A SUBMILLIMETRE-BRIGHT $z \sim 3$ OVERDENSITY 103
5.1 Introduction 104
5.2 Observations and Data Reduction 106
5.2.1 The RCS 2319+00 Supercluster 106
5.2.2 850μm SCUBA–2 Observations 106
5.2.3 *Herschel*-SPIRE Observations 107
5.3 Analysis and Results 109
5.3.1 SCUBA–2/SPIRE Source Identification 109
5.3.2 Evidence of a Line-of-sight, Submillimetre-bright Protocluster 112
5.3.3 A Submillimetre-bright, Strongly Lensed Galaxy 120
5.4 Summary 123

6 CONCLUSIONS 125
6.1 Summary 125
6.2 Future Work 127

BIBLIOGRAPHY 129

List of Figures

1.1 The simulated evolution of the primordial dark matter density field from $z = 3$ to $z = 0$. The region depicts a comoving scale of $15h^{-1}$ Mpc on a side. At early times, only the smallest modes collapse. Cluster-sized peaks collapse later, accreting halos along bound filaments. At $z = 0$, the cluster has amassed to $\mathrm{M}_{200} \simeq 1.2 \times 10^{15}h^{-1}\,\mathrm{M}_{\odot}$. Taken from Kravtsov and Borgani (2012). 4

1.2 The phase-space diagram for 30 massive clusters in the Millennium Simulations. The orbiting galaxies are colour-coded by accretion histories, as observed at $z = 0.21$. Red through yellow points denote galaxies that were accreted earliest, some of which formed in-situ within the cluster; green points correspond to the back-splash population that is outward bound after reaching pericenter; blueish points are the most recently accreted population and primarily fall outside the trumpet-shaped profile. Taken from Haines et al. (2012). 10

1.3 The spectral energy distribution of the extragalactic background light from ultraviolet to submillimetre wavelengths (excluding the CMB). The contributions from the COB and CIB are roughly equal, with $23\,\mathrm{nW\,m^{-2}\,sr^{-1}}$ from the former, between 0.1–8 μm (Dole et al., 2006), and $27\,\mathrm{nW\,m^{-2}\,sr^{-1}}$ from the latter, between 8–1000μm (Béthermin et al., 2012). Taken from Soifer et al. (2008). 12

1.4 The spectral energy distribution for Arp220, a local ULIRG, redshifted from $z = 1.0$ (pink) to $z = 10.0$ (red). The bands correspond to the wavelengths addressed in this thesis: 24 μm (*Spitzer*-MIPS); 100, 160 μm (*Herschel*-PACS); 250, 350, 500 μm (*Herschel*-SPIRE); and 850 μm (SCUBA-2). The 850 μm flux is nearly constant at all redshifts from redshifts 1–10 due to the negative k-correction, while the other bands all suffer from cosmological dimming to some extent. 16

2.1 Colour magnitude diagrams illustrating the power of the cluster red sequence method in the RCS1 survey, over a wide range of redshift. The thicker points correspond to all galaxies within 0.5 Mpc of the cluster center. The solid line depicts the fiducial red sequence, estimated from the Bruzual and Charlot (1993) stellar population models with a 0.1 Gyr starburst ending at $z = 2.5$. Taken from Gladders and Yee (2005). 22

2.2 The evolution of the spectral energy distribution of an elliptical galaxy template from $z = 0$ to $z = 2.0$, with the redshifted value of 4000 Å highlighted with gold. The observed transmission filters for r' and z' from the CFHT, along with 3.6 μm from IRAC, are shown with ascending wavelength, respectively. The upper panel illustrates the success of RCS at $z < 1$ with r' (blue) and z' (red), while the bottom panel depicts why IRAC is necessary to replace z' as the red filter at $z > 1$. Also clear is the monotonic increase towards red colours using the respective filters for each wavelength regime, yielding a non-degenerate photometric estimate of the cluster redshift. 23

3.1 The 24 μm differential number counts of our catalog, normalized to the Euclidean slope (filled squares). We compare to published counts from Papovich et al. (2004) to determine a completeness limit of 70 μJy. . 39

3.2 The strength of the 4000-Å break as a function of stellar mass for the cluster ($z = 0.872$; filled circles) and coeval field ($0.84 < z < 1.0$; open squares) population. The galaxies with [OII] emission (star forming) are plotted in cyan, while those without any [OII] emission are purple. A green diamond denotes coincident 24 μm emission; there are three MIPS detections, all with [OII] emission, at the location of the thickest green diamond with a D4000 of 1.3 and stellar mass of $\sim 1.7 \times 10^9$ M$_\odot$. The dashed vertical line illustrates our mass limit of 2.0×10^9 M$_\odot$, and the dotted horizontal line indicates our cut in D4000 in subsequent plots. We note that the two most massive cluster members have both been identified as the brightest cluster galaxies, although only one is detected at 24 μm. 45

3.3 The relative velocity as a function of clustercentric radius for all spectroscopic members. Red circles corresponds to older galaxies with D4000 > 1.4 and blue circles denote younger galaxies, D4000 < 1.4. The histograms correspond to the number of galaxies within 900 km s^{-1} velocity bins; the colours correspond to the same types of galaxies in the legend on the left. The black histogram represents the population of old galaxies with the MIPS sources removed (6 in total). The green histogram shows all MIPS sources, regardless of age. 47

3.4 Upper panels—The individual SSFRs for all cluster members as a function of clustercentric radius (left panel) and density using the 10th nearest neighbor (right panel). The green stars correspond to MIPS cluster members, and the black circles with arrows are 3σ upper limits on the SSFR given the stellar mass for the cluster members without MIPS detections. Lower panels—The SSFR in bins of clustercentric radius (left) and density (right). The green stars correspond to the average SSFR of detected MIPS members in each bin, i.e., the SFR divided solely by the mass of MIPS members and averaged over the number of MIPS galaxies in each bin. Black circles represent the average SSFR for all cluster members, assuming a 3σ upper limit on the SSFR for undetected MIPS members. Cyan triangles denote the integrated SFR (above our SFR-limit) per total unit stellar mass: a sum of the total 24um-derived SFR divided by the total stellar mass of all spectroscopic members in each radial bin, which essentially probes the fraction of star-forming galaxies. The horizontal solid green line illustrates the best fit line to the green stars with the slope fixed to zero, i.e., the normalization of the average MIPS SSFR. The dot-dashed horizontal line corresponds to the required SSFR for the mass to double by $z = 0$. The two remaining lines in the lower right panel depict the best linear fits to the corresponding binned values with density. The open squares represent the stacked IR SSFRs from Patel et al. (2009) in a $z = 0.834$ cluster, where teal squares correspond to galaxies with masses of $2.0 \times 10^{10} < \mathrm{M}/\mathrm{M}_{\odot} < 6.3 \times 10^{10}$, and the grey squares represent all galaxies with $\mathrm{M} > 6.3 \times 10^{10}\,\mathrm{M}_{\odot}$. 52

3.5 Top—SFR versus stellar mass for MIPS cluster galaxies, separated in colour by D4000. Open squares are the field population from $0.84 < z < 1.0$. The dotted, solid, and dashed black lines correspond to the field trends at $z = 0, 1, 2$, respectively (converted to a Chabrier IMF). The pink dot-dashed line denotes the boundary between the two populations of the cluster galaxies: main-sequence vs sub-main sequence, as defined by their star formation rate. The vertical and horizontal gray dashed lines indicate our mass completeness, $\mathrm{M} > 2.0 \times 10^{9}\,\mathrm{M}_{\odot}$, and SFR detection limit, respectively. Bottom—SSFR versus stellar mass. Symbols and lines are the same as the top panel. 54

3.6 The resulting stacked spectra of MIPS cluster members from each population identified in §3.4.4: main sequence population (cyan spectrum) and sub-main sequence population (pink spectrum). Individual spectra are weighted by their spectroscopic completeness, as determined by their stellar mass and clustercentric radius. 56

3.7 Left—The absolute line-of-sight velocity as a function of projected radius. MIPS members belonging to the main (sub-main) sequence of SFR are highlighted with cyan (pink) squares. The horizontal lines correspond to σ_v and $2\sigma_v$, and the vertical line represents $0.5r_{200}$. The boxed areas correspond to the divisions in Mahajan et al. (2011) and are identical in both panels. Right—The first number on the left in each rectangle corresponds to the fraction of galaxies classified as virialized (orange), infall (purple), and backsplash (gray) in projected phase space bins from dark matter simulations in Mahajan et al. (2011). We then apply the fractions to the total number of spectroscopically confirmed cluster members in each bin and list it after the colon. The third number represents the actual number of each type of galaxy within that phase space based on its age and SFR (for MIPS-detected members). We assume a simple classification in which: virialized galaxies consist of non-star forming older galaxies (red circles) and MIPS-detected older galaxies on the sub-main sequence (red circles with pink squares); infalling galaxies include non-star forming younger galaxies (blue circles) and MIPS-detected galaxies on the main sequence, both young (blue circles with cyan squares) and old (red circles with cyan squares); and backsplash galaxies comprise younger MIPS-detected galaxies on the sub-main sequence (blue circles with pink squares). The last column in each bin (green number in parentheses) represents the number of MIPS sources of that galaxy type that are included in the actual number counts based on the classification scheme stated above. 61

3.8 The strength of the 4000-Å break versus $(r/r_{200}) \times (\Delta v/\sigma_v)$ for all cluster members, divided in two mass bins. The MIPS members on the main and sub-main sequence are highlighted with cyan and pink squares, respectively. The solid gray line shows the best fit line for all galaxies. The median D4000 values for both mass bins in each region (denoted by the vertical dashed lines) are plotted as filled stars and indicate a declining accretionary sequence with $(r/r_{200}) \times (\Delta v/\sigma_v)$. The error bars are taken from the standard deviation on the bootstrapped median in each bin. We have labeled the regions based on accretion times. We note the three galaxies with the lowest caustic values are artificially plotted at $(r/r_{200}) \times (\Delta v/\sigma_v) = 0.006$ to reduce the size of the plot, but in fact have even lower values. 65

3.9 A caustic diagram for all spectroscopically confirmed cluster members. The symbols are the same as in Figure 3.7. We plot caustic profiles—lines of constant $(r/r_{200}) \times (\Delta v/\sigma_v)$—at 0.1 and 0.4 to isolate virialized (within the inner caustic), backsplash (between caustics), and infall galaxies (along and outside the outer caustic). 68

3.10 The SSFR for star-forming galaxies as a function of caustic environment, $(r/r_{200})\times(\Delta v/\sigma_v)$. The sub-main sequence galaxies (pink squares) primarily inhabit low values of $(r/r_{200})\times(\Delta v/\sigma_v)$ compare to the main-sequence galaxies. In contrast to Figure 3.4, there is now a clear depression (0.9 dex) of the average SSFR (green stars) towards low caustic values, where we expect to isolate galaxies accreted at earlier times. The gray vertical lines indicate the limits of the bins. 69

4.1 *Herschel*-PACS maps at 100 (left column) and 160 μm (right column) for EN1-349 (top row), EN2-111 (middle row) and EN2-119 (bottom row). We plot spectroscopically confirmed cluster members with [OII] emission in yellow, and those without in pale green. 79

4.2 Stacked images for each phase-space bin at 100 μm. The left, middle, and right column show lower to higher phase-space bins: $(r/r_{200})\times(\Delta v/\sigma_v) < 0.1$, $0.1 < (r/r_{200})\times(\Delta v/\sigma_v) < 0.4$, and $(r/r_{200})\times(\Delta v/\sigma_v) > 0.4$, respectively. The upper panel displays the resulting stack from a simple average, while the lower panel represents a weighted, clipped, and trimmed average, as described in Section 4.3.1. The removal of contamination in the lower stacks is evident. We also include the radius used for aperture photometry, 5.6 arcsec, with the yellow circle. The colour bar shows the gray scale in janskys per pixel. 83

4.3 Stacked images for each phase-space bin similar to those in Figure 4.2, but at 160 μm. The purple circles represent apertures of 10.5 arcsec. . 84

4.4 Stacked flux densities in the SPIRE maps using our modified version of SIMSTACK. We simultaneously stack seven catalogs, three of which include star-forming cluster members in phase-space bins (upper panel; filled circles), and four from MIPS prior positions separated by flux (lower panel; filled squares). The flux at the lowest phase-space bin (orange circles) is only detected at 250 μm; the 70–100 μJy MIPS bin is not detected at any wavelength and therefore is not plotted; and the 100–200 μJy MIPS bin (cyan squares) lacks a stacked detection at 500 μm. 88

4.5 Modified blackbody fits to the thermal portion of the spectral energy distribution using five wavelengths from stacked *Herschel*-PACS (100 and 160 μm) and *Herschel*-SPIRE (250, 350, and 500 μm) fluxes, shown as solid circles. The best fit for each phase-space bin is represented by the solid line, with the resulting parameter values for dust temperature (in units of Kelvin) and reduced χ^2 listed. The orange, purple, and blue colours correspond the ascending phase-space bins: $(r/r_{200}) \times (\Delta v/\sigma_v) < 0.1$; $0.1 < (r/r_{200}) \times (\Delta v/\sigma_v) < 0.4$; and $(r/r_{200}) \times (\Delta v/\sigma_v) > 0.4$, respectively. The lowest phase-space bin (orange curve) does not have detections at 350 and 500 μm, and therefore is fit solely with the remaining three flux values. These fits allow for determination of the integrated infrared luminosity, given in units of $L_\odot$. 90

4.6 The star formation rate (upper panel) and specific star formation rate (lower panel) for star-forming galaxies as a function of phase-space. Star formation rates are derived from PACS and SPIRE fits to the thermal portion of the spectral energy distribution. Uncertainties are estimated from shifting the best fit dust temperature by $\pm 1\sigma$ and recalculating the infrared luminosity. We find the specific star formation to be constant between recently accreted and intermediate galaxies, but declines with the earliest accreted cluster galaxies. 92

4.7 The best-fit dust temperature for each stacked population in phase-space. The intermediate galaxies (middle phase-space bin) display the coldest dust temperature ($\sim 30\,K$). The uncertainties are 1σ errors on the temperature from fits to the spectral energy distribution assuming β is fixed at 1.7. 93

4.8 An infrared colour-colour diagram for the three phase-space bins: orange ($r \times \Delta v < 0.1$); purple ($0.1 < r \times \Delta v < 0.4$); and blue ($r \times \Delta v > 0.4$). The observed f_{250}/f_{160} colour corresponds to f_{114}/f_{73} at $z = 1.2$, and observed f_{160}/f_{100} corresponds to a rest-frame colour of f_{73}/f_{45}. We see a rough trend of increasing f_{114}/f_{73} with decreasing f_{73}/f_{45}. The intermediate population (purple star) has the coldest f_{114}/f_{73} and warmest f_{73}/f_{45} ratio. 97

5.1 Left: 850μm signal-to-noise ratio map of the RCS 2319+00 supercluster overlaid with the red-sequence contours indicating the cluster positions in red. We highlight all SMGs detected at $>3.5\sigma$ in the 850μm map with orange circles. The green contours show the fractional overdensity of SMGs compared to the average density over the field, starting at $\delta = -0.3$ and increasing by levels of 0.7. The white circle represents the region from which sources are extracted. Right: a zoom-in on the overdensity of SMGs surrounding RCS 2319–C, labeled with their ID in the 850μm catalog. Given its proximity to the centre of RCS 2319–C (the BCG is marked by the green cross), the brightest source in the catalog, SMM J2319.1, is possibly lensed by the cluster potential. . . 108

5.2 *Herschel*-SPIRE maps of the RCS 2319 cluster field at 250 (blue), 350 (green), and 500μm(red). The red-sequence contours are overlaid in yellow to illustrate the three cluster components. 110

5.3 Differential source counts at 850μm within the RCS 2319 cluster field for all 3.5σ detected SMGs (red circles). The error bars are standard Poisson uncertainties. The source counts from SHADES (purple X) are plotted as a consistency check. 111

5.4 Postage stamps of $36'' \times 36''$ for the four SMGs detected with the highest significance in the overdensity centered on RCS 2319–C. The gray scales correspond to 850 μm, 250 μm, 24 μm, 3.6 μm, and 2.2 μm, from left to right. The white circles represent the $10''$ search radius used to identify likely counterpart emission to each SMG. The pink contours on the 850 μm image represent 1.4 GHz detections from the radio map, starting at 45 μJy and increasing by levels of 20 μJy. Overlaid on the 250 μm image are 350 μm and 500 μm contours in blue and orange, respectively. The levels of the contours differ between each image, but are shown to illustrate the increased level of blending and confusion at longer wavelengths, especially for the lower signal-to-noise sources. The green circles represent 24 μm detections with the $6''$ radius signifying the MIPS point spread function. The cyan (purple) squares correspond to detections at 3.6 μm (2.2 μm), and have a $2''$ radius. These last two wavelengths (3.6 and 2.2 μm) are not used in the counterpart identification process but are shown for completeness. The pink cross in all images marks the position of the SMG. 113

5.5 Postage stamps for the four remaining SMGs within the overdensity. The symbols are the same as Figure 5.4. 114

5.6 The angular autocorrelation function for SMGs with a linear bias of 3.37 ± 0.82 (solid gray band) as derived in Hickox et al. (2012). Also shown is the dark matter correlation function (dashed line). We compute the Landy-Szalay estimator in our simulated dark matter density field with an input bias of 3.37 to check the clustering is consistent with that of SMGs from Hickox et al. (2012). 116

5.7 The surface density map showing the fractional over density of SMGs in the real map (top panel), and for two of the 1000 realisations of simulated clustered catalogs (bottom panel). The left map illustrates a case where the simulations produce a peak of $\geqslant 3.5$ ($< 1\%$ of the time), while the right map demonstrates the remainning 99% of the catalogs that show less clustering than the real map. The contours shows fractional over density levels starting at -0.25 and increasing by 1.0. 117

5.8 Submm/far-IR colour ratios for all SMGs that have unblended SPIRE counterpart emission in the top panel, and solely SPIRE colours in the bottom panel. Both plots show the change of these colour ratios (gray line) with redshift using the median luminosity template from Chary and Elbaz (2001), where the navy squares denote $z = 2.5, 2.9, 3.5$. The possible protocluster members are highlighted in pink, and are at the higher-z end of the distribution with similar far-IR/submm colours. Confusion errors are not shown for clarity. 118

5.9 Modified blackbody fits to the SPIRE and SCUBA-2 fluxes for the three possible protocluster members, using the technique described in Section 5.3.2. The parameters for the best fit values with β fixed at 1.5 (blue), 1.75 (green) and 2.0 (red) are listed in each panel. The lowest reduced χ^2 values are given by $z = [3.5, 2.9, 2.5] \pm 0.6$ and $T_{\rm d} = [48, 43, 41] \pm 8$ K for SMMs J2319.1, 2319.6, and 2319.16, respectively. We note that SMM J2319.1 has only a weak radio detection, just below the catalogue limit; we therefore assign it the 3σ rms limit of 45μJy. . 121

5.10 A gK[4.5] colour composite (from CFHT and IRAC) of the centre of RCS 2319–C, showing the position of with SMM J2319.1, the possible lensed SMG (850μm S/N contours starting at 5σ, increasing by levels of 1σ), Note the very red optical/near-IR emission coincident with the SCUBA-2 detection. We highlight the BCG, with a blue arc-like feature to the south, further indicating that this could be a strong-lensing cluster. 122

List of Tables

3.1 Spectroscopic measurements from the weighted, stacked spectra. . . . 55

4.1 The *Herschel*-GCLASS sample at $z \sim 1.2$. 76
4.2 The *Herschel*-SPIRE fields. 80
4.3 *Herschel* stacked flux densities in phase-space bins. 87
4.4 Best fit spectral energy distributions for stacked cluster members in phase-space bins. 89

ABSTRACT

We present a multi-wavelength perspective of star-forming galaxies within high-redshift galaxy clusters. The clusters derive from the Red-sequence Cluster Survey (RCS) and the Spitzer Adaptation of the Red-sequence Cluster Survey (SpARCS), and possess ample spectroscopic coverage, yielding numerous confirmed cluster members. This thesis consists of a collection of distinct but related works, focusing on environmental effects within the dense regions of clusters—some of the rarest structures in the Universe. We exploit the high sensitivities of cutting-edge infrared and submillimeter telescopes to glean the wealth of information encoded within the thermal portion of the spectral energy distribution, including infrared luminosities and dust temperatures. This allows us to uncover various trends within the star-forming population as a function of environment. Moreover, we develop a novel definition of environment, based on the phase space of radius and velocity, to account for the various accretion histories of galaxies onto clusters; it thereby probes the time-averaged density that each galaxy population has experienced. Using this tracer of environment, we find a significant depression in the star formation rate per unit stellar mass for star-forming galaxies within cluster cores at $z \sim 0.9$ and $z \sim 1.2$, in contrast to the flat trend that results from conventional definitions of environment. We also discover a population of galaxies that have lower dust temperatures compared to both infalling galaxies and those that were accreted at the earliest stages of the formation of the cluster. Taken together, these trends in star formation rate and dust temperature can help elucidate which, if any, quenching mechanisms are active within cluster environments. Finally, we report the serendipitous detection of an overdensity of submillimeter-bright galaxies located behind a merging $z \sim 0.9$ supercluster, which could signify a highly star-forming protocluster at $z \sim 3$.

Résumé

Nous présentons une analyse multi-fréquentielle de galaxies à formation d'étoiles situées l'intérieur d'amas de galaxies fortement décalés vers le rouge. Ces amas en provenance du sondage Red-sequence Cluster Survey (RCS) et de son adaptation par Spitzer (SpARCS) possèdent une large couverture spectroscopique et contiennent plusieurs membres confirmés. Cette thèse représente une collection de travaux distincts mais reliés, qui se concentrent sur les effets environnementaux présents l'intérieur des régions denses d'amas de galaxies, des structures parmi les plus rares de l'Univers. Nous exploitons la sensibilité élevée des télescopes infrarouges et submillimétriques de pointe pour collecter l'information encodée dans la portion thermale de la distribution spectrale d'énergie, ce qui inclue des mesures de luminosité infrarouge et des températures de poussière. Cette méthode nous permet de dévoiler plusieurs tendances en cours l'intérieur de la population de galaxies formation d'étoiles en fonction de l'environnement où se trouvent ces galaxies. De plus, nous développons une nouvelle définition de ce qui constitue l'environnement d'une galaxie basée sur l'espace de phase du rayon et de la vitesse. Cette définition tient compte des nombreux épisodes d'accrétion de galaxies par les amas de galaxies, traçant ainsi la densité moyenne connue par chaque population de galaxies. En utilisant ce nouveau traceur d'environnement, nous trouvons un manque important dans le taux de formation d'étoiles par unité de masse stellaire pour les galaxies formation d'étoiles situées au coeur d'amas de galaxies entre $z \sim 0.9$ et $z \sim 1.2$, ce qui contraste avec le taux constant résultant d'une définition conventionnelle de l'environnement. Nous avons aussi découvert une population de galaxies ayant des températures de poussire plus basse que celles associées des galaxies qui tombent ou qui ont été accrétées au début de la formation de l'amas de galaxies. Considérées ensemble, ces tendances caractérisant le taux de formation d'étoiles et la température de poussière peuvent aider à mettre en lumière les mécanismes de relaxation actifs l'intérieur des amas de galaxies. Pour terminer, nous rapportons la détection fortuite d'une surdensité de galaxies submillimétriques situées derrière un superamas de galaxies $z \sim 0.9$, ce qui pourrait indiquer la présence d'un proto-amas à haute formation d'étoiles à $z \sim 3$.

ACKNOWLEDGMENTS

Most importantly, I thank my supervisor, Tracy Webb. She has provided me with endless support, encouragement, and discussions throughout my entire graduate career. I will always appreciate the time she has invested as a mentor, inspiring confidence and wisdom. I also thank Adam Muzzin and Jim Geach, both of whom made many beneficial contributions to the work in this thesis. I appreciate all the members of the SpARCS and RCS collaborations, who provided many useful comments during the writing stages. I acknowledge Gabrielle Simard for translating my abstract into French. I am grateful for many friends over the course of my PhD who made life outside of work more enjoyable. Finally, I thank my parents and twin sister, Lindsay, for their invaluable guidance and encouragement, and Alex, who is always there for me.

CONTRIBUTIONS OF AUTHORS

CHAPTER 3

The SpARCS collaboration performed the cluster detection and estimated all cluster properties for SpARCS J161314+564930. Tracy Webb reduced the MIPS observations and created a 24 μm source catalog with photometry. Adam Muzzin handled the spectroscopy for individual galaxies, determining cluster membership and stellar masses. I contributed to fitting of the equivalent widths for the spectra, improving the automated algorithm for the entire GCLASS sample, including SpARCS J161314+564930. I also stacked the spectra within this chapter, and estimated all properties on the stacked spectra. Except for the stellar masses (Section 3.3.2), I performed the remaining MIPS analysis in Section 3.3, which includes counterpart identification, star formation rate estimates, and AGN diagnostics (using IRAC photometry from Remco van der Burg). I also developed the phase-space definition for environment and determined all results in Sections 3.4 and 3.5. All text was written by me, and I created all the figures.

CHAPTER 4

The clusters were detected by the SpARCS collaboration. Gillian Wilson determined velocity dispersions and cluster masses, and Adam Muzzin performed the spectroscopic analysis. I reduced all *Herschel* data from PACS and SPIRE. The SPIRE maps were downloaded from public archival data, but the PACS maps resulted from observing time that was awarded based on a proposal for which I wrote the science and technical justifications. I modified a public SPIRE stacking code, and developed and wrote the entire code for PACS stacking and photometry. I performed all remaining work (the entirety of Section 4.4), including the fits to the spectral energy distributions, and subsequent estimates of the dust temperatures and infrared luminosities. I also developed a possible interpretation for quenching mechanisms within galaxy populations. I wrote the entirety of the text and made all figures.

Chapter 5

The supercluster was discovered by the RCS team. Jim Geach reduced the SCUBA-2 data, did the 850 μm photometry, and estimated false-detection rates. The SCUBA-2 data were observed by myself and Alexander van Engelen at the JCMT, and I wrote and planned the proposal. I reduced the *Herschel*-SPIRE map, and subsequent 250–500 μm photometry. The SPIRE map resulted from a proposal written by Jim Geach. As for the ancillary data sets, Rob Ivison reduced the radio map, while I created the source catalog and photometry. Tracy Webb reduced the MIPS map and performed 24 μm photometry. Alexander van Engelen created the simulated catalogs of clustered sources, which I then used to calculate the probability of finding a similar overdensity. I performed the remaining analysis: counterpart identification, convolved surface density estimation, Landy-Szalay analysis, and spectral energy distribution fitting. I created all figures. The text was mostly written by me, but Jim Geach wrote Section 5.2.2 and contributed to the text in Sections 5.1, 5.3.3, and 5.4.

Dusty Star-Forming Galaxies within High-Redshift Galaxy Clusters

1

INTRODUCTION

"In all things of nature there is something of the marvelous."

Aristotle

1.1 MOTIVATION

The environment in which a galaxy resides has emerged as a fundamental parameter in the study of galaxy evolution. It represents a unifying crossroad between observational and theoretical astronomy, by advancing the current technological boundaries while providing a testing ground for the latest cosmological predictions. As with many other scientific disciplines, the study of galaxy environment has incited the age-old battle of nature versus nurture—are galaxies subject to their own destiny, governed by their inherent properties, or do external forces dictate their ultimate fate? The largest bound structures in the Universe, clusters of galaxies, offer the best laboratory with which to study environmental effects.

To understand how environment might impact galactic evolution, we must first delve into both the key ingredients that comprise a cluster and the formation mechanisms of clusters. Galaxy clusters are reservoirs for the bulk of the baryonic matter in the Universe. This luminous matter primarily lies within the confines of the intracluster medium, a hot plasma of electrons, which dominates over the cluster stellar mass by a factor of ten on average (Kravtsov and Borgani, 2012). However, the prevailing matter component is non-baryonic, in the form of diffuse dark matter which accounts for most of the cluster mass.

A cornerstone of cosmology has been the development of hierarchical structure formation theory, a recipe for galaxy and cluster formation (Press and Schechter, 1974). In this paradigm, astrophysical sources grow from a bottom-up perspective: tiny fluctuations in the very early Universe seed the growth of structure through gravitational amplification, as matter (both baryonic and non-baryonic) collapses into its own potential wells. The shortest wavelength modes in the initial density field collapse first; these structures evolve into galaxy-sized dark matter haloes which continually accrete matter along cosmic filaments and merge with neighboring galaxies and groups, building up mass. This sea of collapsed dark matter haloes are atop the underlying longer-wavelength modes which collapse last, forming the largest gravitationally bound structures, galaxy clusters.

This complex process is simulated from $z = 3$ to the present day in Figure 1.1 from Kravtsov and Borgani (2012), with the smallest objects collapsing first at the nodes of density peaks in the primordial field. The cosmic web of filamentary structure is also visible at early epochs. These small collapsed objects gradually amass matter through merging activity, and eventually the larger-scale peaks collapse into a massive cluster at late times. The cluster builds up mass, preferentially accreting matter along the cosmic filaments.

Thus, in the most basic picture, galaxy clusters consist of hundreds of galaxies belonging to one of two populations: an older collection of galaxies that formed in situ, some of which merged; and a nascent population that was accreted over cosmic time. This is of much importance—it signifies the potential of clusters as laboratories with which to gauge differences between galaxies formed in distinct environments. For example, how do galaxies born in the isolated field compare to those born in the densest environments, and additionally, how does accreted matter evolve as it falls deeper into the cluster potential well?

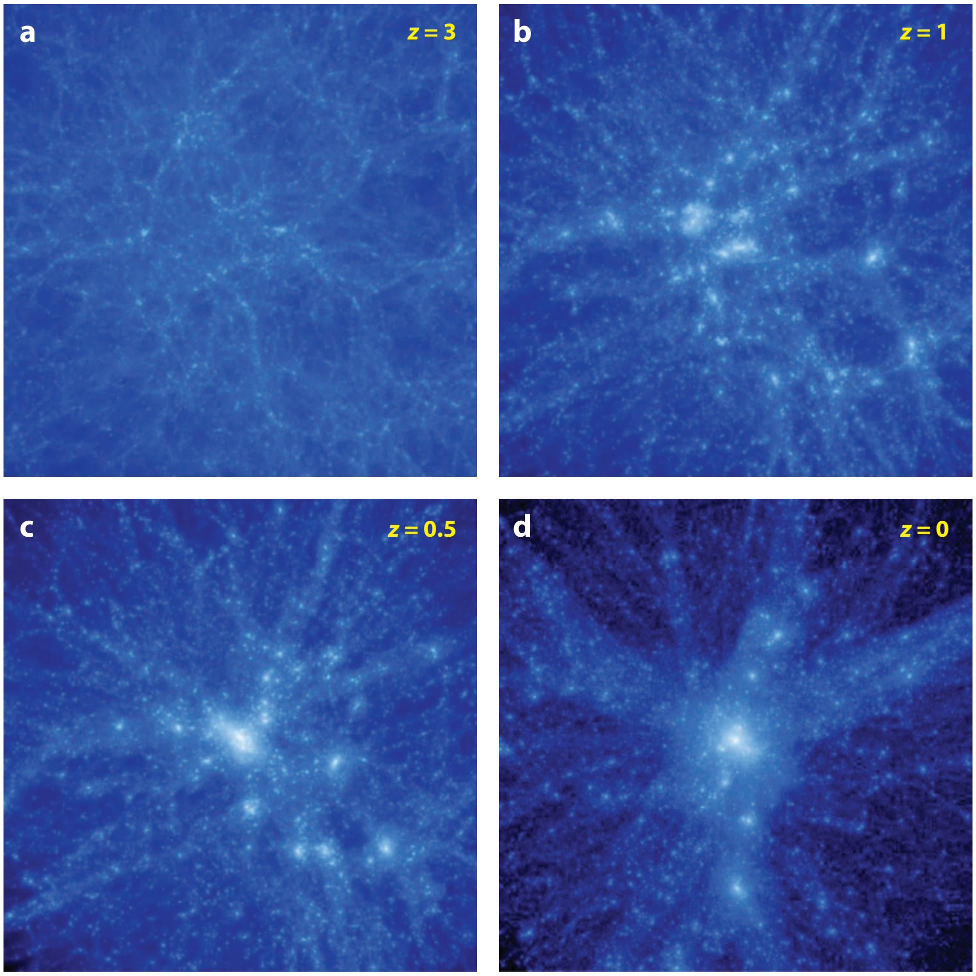

Figure 1.1 The simulated evolution of the primordial dark matter density field from $z = 3$ to $z = 0$. The region depicts a comoving scale of $15h^{-1}$ Mpc on a side. At early times, only the smallest modes collapse. Cluster-sized peaks collapse later, accreting halos along bound filaments. At $z = 0$, the cluster has amassed to $\mathrm{M}_{200} \simeq 1.2 \times 10^{15} h^{-1}\,\mathrm{M}_{\odot}$. Taken from Kravtsov and Borgani (2012).

The evolution of a galaxy falling into the cluster potential is most likely a volatile one. The hostile cluster environment exerts much of its influence through the intracluster medium. The most widely invoked of such mechanisms are strangulation and ram-pressure stripping. The milder of the two processes, strangulation (sometimes referred to as starvation) involves the removal of the hot halo of low-density gas enveloping a satellite galaxy (Larson et al., 1980; Balogh et al., 2000). This results in a gradual depletion of the galaxy's gas supply which would otherwise cool, condense, and settle onto a cold disk—the breeding ground for star formation. Ram-pressure stripping is a more violent process, occurring when high-velocity galaxies move through the dense intracluster medium (Gunn and Gott, 1972; Quilis et al., 2000). The intracluster medium exerts a strong dynamical pressure on these galaxies, capable of stripping the cold disk of gas, thereby directly exhausting the fuel for star formation. This process only operates deep within the cluster potential as it requires high galactic velocities, while strangulation functions at all radii, including in the peripheral regions, since the halo is more diffuse and therefore easier to remove than the disk (Treu et al., 2003).

Other mechanisms that are not related to the conditions of the intracluster medium can also alter the properties of cluster galaxies. For example, deep within the cluster core, gravitational tidal effects can disrupt gas and stellar components that lead to truncated star formation rates or morphological transformations (Moore et al., 1999). Another viable mechanism for galactic structural changes, which can greatly damage galaxy disks, are high-speed encounters between galaxies. This is known as galaxy harassment (Moore et al., 1996, 1998). Lastly, in the cluster outskirts and within galaxy group scales, low-speed galaxy-galaxy mergers can trigger starbursts and active galactic nucleus activity, and also possibly lead to the transformation of a disk galaxy into an elliptical (Icke, 1985; Mihos, 1995).

In this thesis, we will present a cosmic narrative of the significance of environment within the extreme densities of galaxy clusters and their influence on the constituent galaxies. This first chapter offers a historical review over the last few decades on what has been gleaned thus far in the field of galaxy clusters, with particular attention to environmental trends over cosmic time. We also highlight the utility of infrared and submillimetre studies. We reserve the second chapter for a description of the theoretical and observational methods that are of relevance to the work in this thesis.

The third chapter focuses on a single galaxy cluster at $z \sim 0.9$ and environmental effects from an infrared perspective at $24\,\mu$m. We introduce an approach to assessing these effects through a novel definition of environment based on galaxy dynamics. We utilize a combination of galaxy clustercentric radii with line-of-sight velocities to extract accretion histories, rather than using the standard measures of environment: density or clustercentric radius.

We extend this analysis in the fourth chapter to a sample of three clusters at $z \sim 1.2$ with multi-wavelength coverage from 100–500$\,\mu$m. Extended coverage of the thermal domain of the spectral energy distribution allows for more accurate estimates of star formation rates and dust temperature constraints.

The fifth chapter progresses to even longer wavelengths, larger structures, and higher redshifts. We present an 850$\,\mu$m study of three merging galaxy clusters—a supercluster, at $z \sim 0.9$—and unveil an overdensity of galaxies at $z \sim 3$, which may be a protocluster.

We conclude the thesis in Chapter 6 with an outlook on where the most promising science lies in the years ahead, focusing particularly on the exciting prospects with molecular gas studies from the Atacama Large Millimeter Array (ALMA).

1.2 ENVIRONMENTAL TRENDS

The significance of clusters as nurseries for galaxy transformations, rather than dormant environments, dates back to the pioneering work of Edwin Hubble; he not only assigned a morphological sequence for galaxies (Hubble, 1926), but also recognized the prominence of elliptical galaxies within clusters (Hubble and Humason, 1931). This phenomenon, quantified half a century later, is now known as the canonical morphology-density relation and states that galaxies with spheroidal morphologies (i.e., elliptical or early-type galaxies) preferentially live in denser regions, with their fraction increasing in clusters (Dressler, 1980). The converse is also true, with late-type spiral galaxies (i.e., galaxies with a spheroidal component surrounded by a flat disk of stars, gas, and dust) populating the lower-density field. Lenticular galaxies, or S0s, lie between ellipticals and spirals on the Hubble tuning fork with central bulges and gas-poor disks; Dressler et al. (1997) found that this intermediary class represents a constant fraction of the galaxy population over all cluster densities.

Large spectroscopic campaigns in the local Universe have offered homogenous galaxy samples with which to unveil many other galaxy correlations. The Sloan Digital Sky Survey (SDSS; York et al., 2000) has had a significant impact on this field with a wealth of photometric and spectroscopic data on $\sim 10^6$ local galaxies, and, consequently, many physical scaling laws have been simultaneously mapped out with environment. For example, a colour bimodality of galaxy populations has been well-established (Strateva et al., 2001; Baldry et al., 2004) and is a strong tracer of density at fixed luminosity (Balogh et al., 2004b; Hogg et al., 2004; Blanton et al., 2005) with the redder distribution in higher-density regions. Additionally, the star formation history of a galaxy trends with environment, as seen through Hα emission (Gómez et al., 2003; Balogh et al., 2004a), and the depth of the 4000-Å break (Kauffmann et al., 2004). These trends seem to be rooted in earlier epochs as well, and many intermediate- and high-redshift cluster surveys (e.g., the Red-sequence Cluster Survey, the ESO Distant Cluster Survey, the *Spitzer*/MIPS Infra-Red Cluster Survey, the Canadian Network for Observational Cosmology, the *Spitzer* Adaptation of the Red-sequence Cluster Survey) have found the same environmental dependencies (e.g., Poggianti et al., 2008; Tran et al., 2009; Finn et al., 2010; Vulcani et al., 2010; Muzzin et al., 2012; Webb et al., 2013).

Mass segregation is also prominent with environment, as massive galaxies are found in increasingly denser regions (Kauffmann et al., 2004; Baldry et al., 2006). Moreover, Kauffmann et al. (2003b) uncovered a characteristic mass scale of 3×10^{10} M$_\odot$ where many galaxy properties change abruptly with stellar mass in the local Universe. Indeed, once the star formation history is accounted for, either through stellar age or mass, many of the aforementioned environmental trends appear to flatten out (Blanton and Moustakas, 2009). For instance, the ages of all types of galaxies (quiescent and star-forming), and the star formation rate per unit stellar mass of star-forming galaxies are all correlated with stellar mass, but lack any dependence on environment at fixed stellar mass (e.g., Kauffmann et al., 2004; Peng et al., 2010; Muzzin et al., 2012; Wetzel et al., 2012). However, the fraction of star-forming galaxies is a strong function of environment and stellar mass, with fewer star-forming galaxies in dense regions and of high mass. This covariance between stellar mass and environment lies at the pinnacle of the very debate mentioned earlier: nature versus nurture.

The key to disentangling this covariance requires systematically mapping out trends with each parameter, while fixing the other, over cosmic time. Peng et al. (2010) have implemented such an analysis with the vast amount of SDSS and zCOSMOS (Lilly et al., 2007) data, creating an empirical account of galaxy evolution from $z \lesssim 1$ to present day. More recently, Muzzin et al. (2012) has extended this type of analysis to $z \sim 1.2$. They both find that the two effects are separable, each with its own mechanism for suppressing star formation, coined "mass quenching" (or "self quenching"), and "environmental quenching." While the effect of environment quenching remains unchanged from $z \sim 1$, mass quenching seems to be a more varied and continual process.

Further elucidation of these processes relies primarily on two criteria: the extension of cluster surveys beyond $z \sim 1$, and a coherent definition of environment. Indeed, it is now clear that the peak epoch of star formation occurred at $1 < z < 3$ (e.g., Madau et al., 1996; Hopkins, 2004; Hopkins and Beacom, 2006; Bouwens et al., 2007). Moreover, the fraction of star-forming galaxies within clusters increases with redshift, as seen in optical (Butcher and Oemler, 1978; Ellingson et al., 2001) and infrared

(Saintonge et al., 2008; Haines et al., 2009; Finn et al., 2010; Webb et al., 2013) studies out to $z \sim 1$, and even rises with increasing galaxy density in a $z = 1.6$ cluster (Tran et al., 2010). This steep evolution appears to be dominated by the infalling population as it mimics the changes in the coeval field population (Haines et al., 2009; Webb et al., 2013). As such, proper definitions of environment that isolate the recently accreted infalling population from the older in-situ population are crucial to accurately assess the effect of environmental quenching.

Utilizing the Millennium Simulation from Springel et al. (2005), Haines et al. (2012) trace out galaxy accretion histories for orbiting galaxies of 30 massive clusters as a function of phase space—line-of-sight velocity versus clustercentric radius (Figure 1.2). These diagrams can reveal the distinct loci occupied by the older, virialized population (red and orange points) with respect to the more recently accreted infall population (green and blue points). This latter population consists of galaxies that have not yet entered into the virial cluster radius, those that have already reached pericenter and are on their way back out, known as back-splash galaxies (Balogh et al., 2000; Mamon et al., 2004), and everything in between. The regions occupied by each of these populations are marked by trumpet-shaped caustic lines that trace the expected orbital velocities within massive clusters (Regos and Geller, 1989). Thus, a phase-space analysis for environment can effectively account for distinctive cluster populations and alleviate some of the projection effects that bias the traditional probes for environment: clustercentric radius and local density. This type of analysis is the focus of Chapters 3 and 4 of this thesis.

1.3 INFRARED/SUBMILLIMETRE OBSERVATIONS

The importance of infrared and submillimetre observations (∼1–1000 μm) is intrinsically linked to the ubiquitous presence of dust throughout the Universe. While historically, ultraviolet and optical studies have paved the way for galaxy evolution

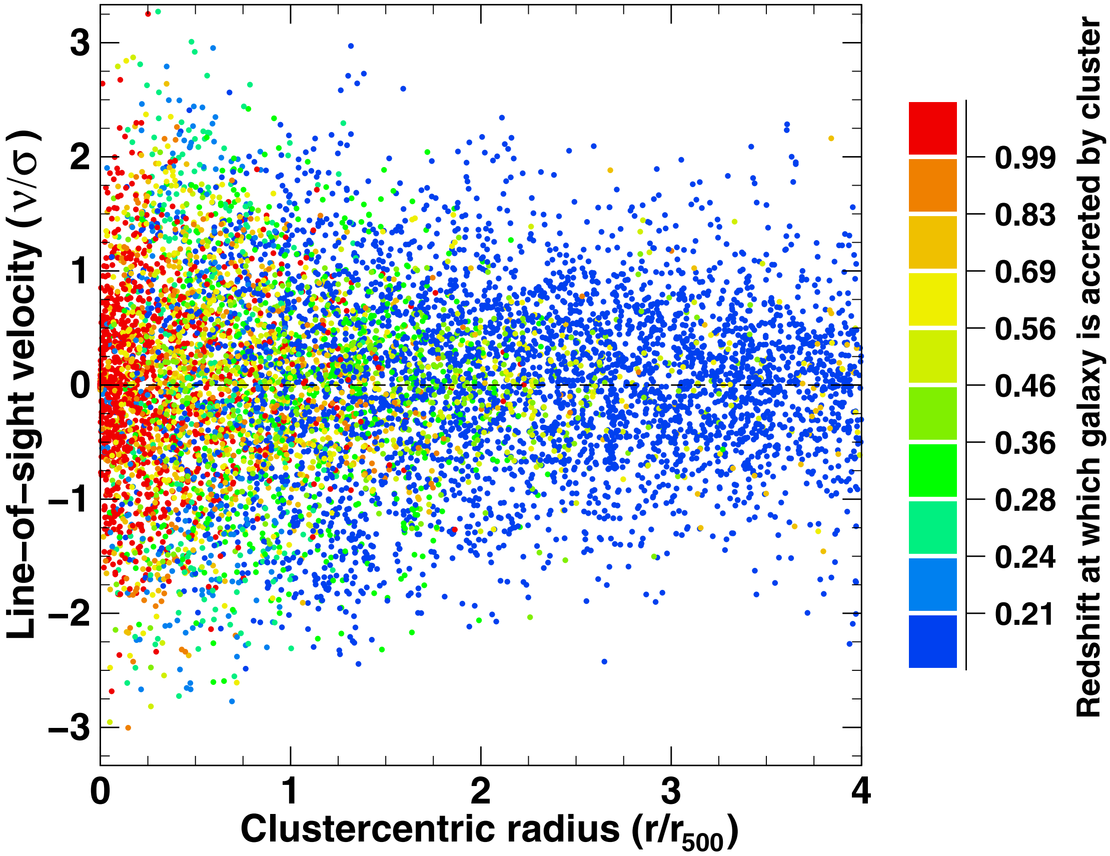

Figure 1.2 The phase-space diagram for 30 massive clusters in the Millennium Simulations. The orbiting galaxies are colour-coded by accretion histories, as observed at $z = 0.21$. Red through yellow points denote galaxies that were accreted earliest, some of which formed in-situ within the cluster; green points correspond to the backsplash population that is outward bound after reaching pericenter; blueish points are the most recently accreted population and primarily fall outside the trumpet-shaped profile. Taken from Haines et al. (2012).

and cluster surveys, a complete view was unattainable due to heavy dust obscuration, which reddens and attenuates optical starlight. Dust grains, typically on the order of ∼10–1000 Å and composed of silicon, graphite, or polycyclic aromatic hydrocarbons (PAHs), absorb light at ultraviolet and optical wavelengths. The grains are heated from the incident light and subsequently re-emit thermal radiation at infrared and submillimetre wavelengths (Draine, 2003).

Indeed, it is now known that approximately half of the starlight ever emitted is ultimately absorbed by intervening dust and emanates in the thermal infrared regime (e.g., Hauser and Dwek, 2001; Lagache et al., 2005). The cosmic background of diffuse extragalactic radiation over the history of the Universe comprises two primary peaks (short-ward of the Cosmic Microwave Background which peaks at 2 mm) of roughly equal brightness. The peaks are located in the optical and infrared regimes, with a minimum at 5 μm (see Figure 1.3). The former peak results from the stellar emission of all extragalactic sources throughout time (the Cosmic Optical Background), while the latter emerges from small dust grains shining thermally (with some contribution from active galactic nucleus emission), and is known as the Cosmic Infrared Background (CIB). Discovered in 1996 with the FIRAS instrument on the Cosmic Background Explorer (COBE) Satellite (Puget et al., 1996; Fixsen et al., 1998; Hauser et al., 1998), the CIB has since spawned countless studies aimed at resolving this background and determining the nature and redshift distribution of the infrared/submillimetre sources that dominate it (e.g., Hughes et al., 1998; Borys et al., 2003; Webb et al., 2003; Coppin et al., 2006; Dole et al., 2006; Knudsen et al., 2008; Devlin et al., 2009; Marsden et al., 2009; Viero et al., 2009; Amblard et al., 2011; Berta et al., 2011; Béthermin et al., 2012; Chen et al., 2013; Holder et al., 2013; Viero et al., 2013—to name a few), which has important implications for cosmological structure formation (Partridge and Peebles, 1967).

The launch of the Infrared Astronomical Satellite (*IRAS*) in 1983 opened a new window onto the dusty Universe, detecting hundreds of thousands of new infrared sources, including some of the first ultra-luminous infrared galaxies (ULIRGs; Aaronson and Olszewski, 1984; Houck et al., 1985). These dusty, star-forming galaxies along with the general population of luminous infrared galaxies (LIRGs; 10^{11} $L_{\odot} < L_{\rm IR} < 10^{12}$ $L_{\odot}$) dominate the CIB, particularly at longer wavelengths ($\lambda \gtrsim 100$ μm;

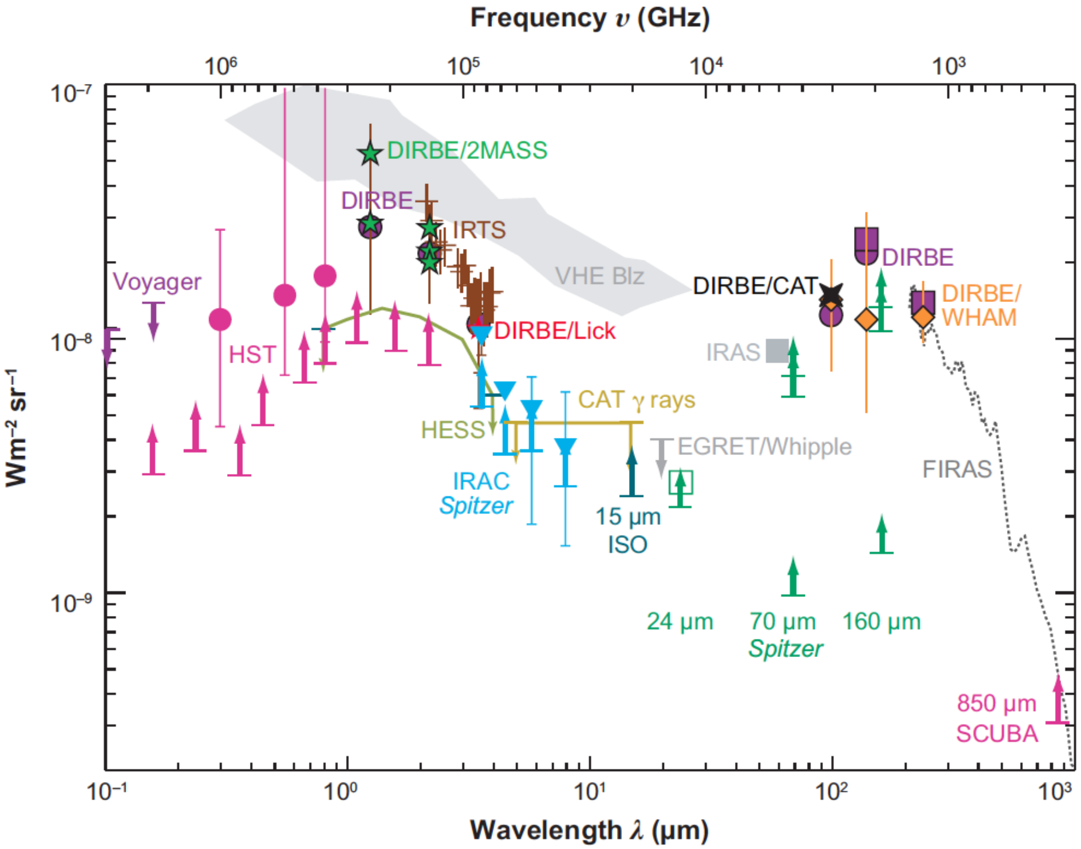

Figure 1.3 The spectral energy distribution of the extragalactic background light from ultraviolet to submillimetre wavelengths (excluding the CMB). The contributions from the COB and CIB are roughly equal, with 23 $\mathrm{nW\,m^{-2}\,sr^{-1}}$ from the former, between 0.1–8 μm (Dole et al., 2006), and 27 $\mathrm{nW\,m^{-2}\,sr^{-1}}$ from the latter, between 8–1000μm (Béthermin et al., 2012). Taken from Soifer et al. (2008).

Viero et al., 2013), and contribute to the majority of the infrared energy density at $z > 0.5$ (Le Floc'h et al., 2005). An upsurge of infrared astronomy followed with subsequent satellites that had vast improvements in sensitivity and resolution: the *Infrared Space Observatory* (ISO), *AKARI*, and the *Spitzer Space Telescope.*

A simultaneous wave of ground-based submillimetre instruments (e.g., SCUBA, LABOCA) extended the study of the dusty portion of the galactic spectral energy distribution, albeit at colder temperatures. The first of its kind, the Submillimetre

Common-User Bolometer Array (SCUBA), discovered a new population of dusty high-redshift galaxies, coined submillimetre galaxies (SMGs), over a decade ago (Smail et al., 1997; Barger et al., 1998b; Hughes et al., 1998), which has had strong implications for galaxy evolution, structure formation, and molecular gas studies. The past discoveries from infrared and submillimetre observations have heralded an exciting future of revelations for the current generation of telescopes, namely the *Herschel Space Observatory* (which just exhausted its helium supply) and the Atacama Large Millimeter Array (ALMA). The utility of these long wavelength telescopes stems from the rich information encoded within the spectral energy distribution of galaxies.

1.3.1 Spectral Energy Distributions and the Negative k-correction

It is now known that the infrared to submillimetre regime of the spectral energy distribution dominates the energy output of many galaxies. The various contributions arise from a gamut of dust grain sizes and distributions that emit thermal radiation at various temperatures. The near-infrared portion of the spectrum ($\sim$1–5 μm) is closest to visible wavelengths, and primarily originates from the photospheres of cooler low mass stars (T $\sim$1000 K). The mid-infrared regime ($\sim$5–40 μm) comprises three primary components: a warm dust continuum (T $\sim$ 100 K); broad emission lines from the vibrational modes of large PAH molecules at 3.3, 6.2, 7.7, 8.6, and 11.3 μm (Leger and Puget, 1984; Tielens, 2008); and silicate absorption peaking at $\sim$9.7 μm with an additional feature at 18 μm (Draine, 2003). These features are all associated with star-forming regions, as young ionizing stars embedded in molecular clouds emit UV/optical photons that heat up the interstellar dust (e.g., Calzetti et al., 2005, 2007), excite PAHs (due to their low heat capacity) (Peeters et al., 2004), and undergo absorption in a dusty screen of silicate material surrounding hot regions. However, active galactic nuclei (AGN), which are encompassed by a dusty torus, can also heat the dust to these temperatures (Rowan-Robinson and Crawford, 1989), and thus are often a source of contamination for estimates of star formation activity with single-band measurements. Multi-wavelength continuum measurements can help disentangle AGN from star-forming systems through colour-colour diagrams or spectral energy distribution fitting (e.g., Lacy et al., 2004; Sajina et al., 2005; Kirkpatrick et al., 2012, 2013)

The longer wavelength emission associated with the far-infrared and submillimetre regimes (∼40–1000 μm) emerges from larger grains. It probes warm and cool dust components (T < 100 K) that are heated by young stars and the more evolved stellar population, respectively. The spectrum in this regime, which monotonically increases up to ∼100 μm and falls off red-ward of the peak, is typically described by three parameters: α, the slope of the power-law at shorter wavelengths; β, the slope of the emissivity at longer wavelengths; and T_d, the dust temperature, which describes the position of the peak. The general shape is that of a blackbody,

$$B_\nu(T_d) = \frac{2h\nu^3}{c^2}\frac{1}{e^{h\nu/kT_d} - 1}, \tag{1.1}$$

although slightly modified to account for the emissivity of the dust grains (Hildebrand, 1983). Blue-ward of the spectral peak (i.e., toward higher frequencies), the Wien spectrum transitions to a power law, $S_\nu \propto \nu^\alpha$ with $\alpha \simeq 2$ (Blain et al., 2002), in order to avoid exponential fall-off down to mid-infrared wavelengths. For optically thin emitters, the modification to the single-temperature Planck spectrum is manifested in a frequency-dependent emissivity term:

$$S_\nu \propto \epsilon_\nu B_\nu(T_d), \tag{1.2}$$

where $\epsilon_\nu \propto \nu^\beta$. A slightly more sophisticated version of the modified blackbody also incorporates the optical depth of the gas cloud and is given by:

$$S_\nu \propto [1 - e^{-\tau_\nu}]B_\nu(T_d). \tag{1.3}$$

This form must assume a crossover frequency (ν_0) at which the cloud becomes optically thick ($\tau_\nu = 1$), which is often fixed to 3 THz (100 μm) (Blain et al., 2003). It relates the emissivity to the optical depth by $\epsilon_\nu = 1 - \exp(-\tau_\nu)$, where $\tau_\nu = (\nu/\nu_0)^\beta$. Values of β typically range between 1–2 (e.g., Dunne et al., 2000).

Red-ward of the spectral peak, there exists a unique aspect of far-infrared and submillimetre studies, known as the negative k-correction. This effect is a natural consequence of bandwidth-limited extragalactic observations, as bluer portions of the spectral energy distribution are sampled over the same observing filter with increasing redshift. This results in an emitted frequency-dependent measurement of the observed flux, given by:

$$S_{\nu_o} = (1+z)\frac{L_\nu(\nu_e)}{4\pi D_L^2}, \tag{1.4}$$

where ν_e is the emitted frequency, $\nu_e = (1+z)\nu_o$. Moreover, the measured flux (over the entire spectral energy distribution) is attenuated with redshift due to an increase in the luminosity distance (D_L). Fortunately, these two effects cancel each other out if the bandpass is far enough down the Rayleigh-Jeans tail of the blackbody: as the bandpass shifts towards shorter wavelengths (with increasing redshift), the flux increases by an amount that is equal to the attenuation from the square of the luminosity distance, yielding a negative k-correction. This effect has favorably been exploited at submillimetre wavelengths, and allows the measurement of a roughly constant flux for constant intrinsic luminosity out to $z \sim 10$. We illustrate this effect in Figure 1.4 with the spectral energy distribution from a local ULIRG, and highlight the bandpasses used in this thesis.

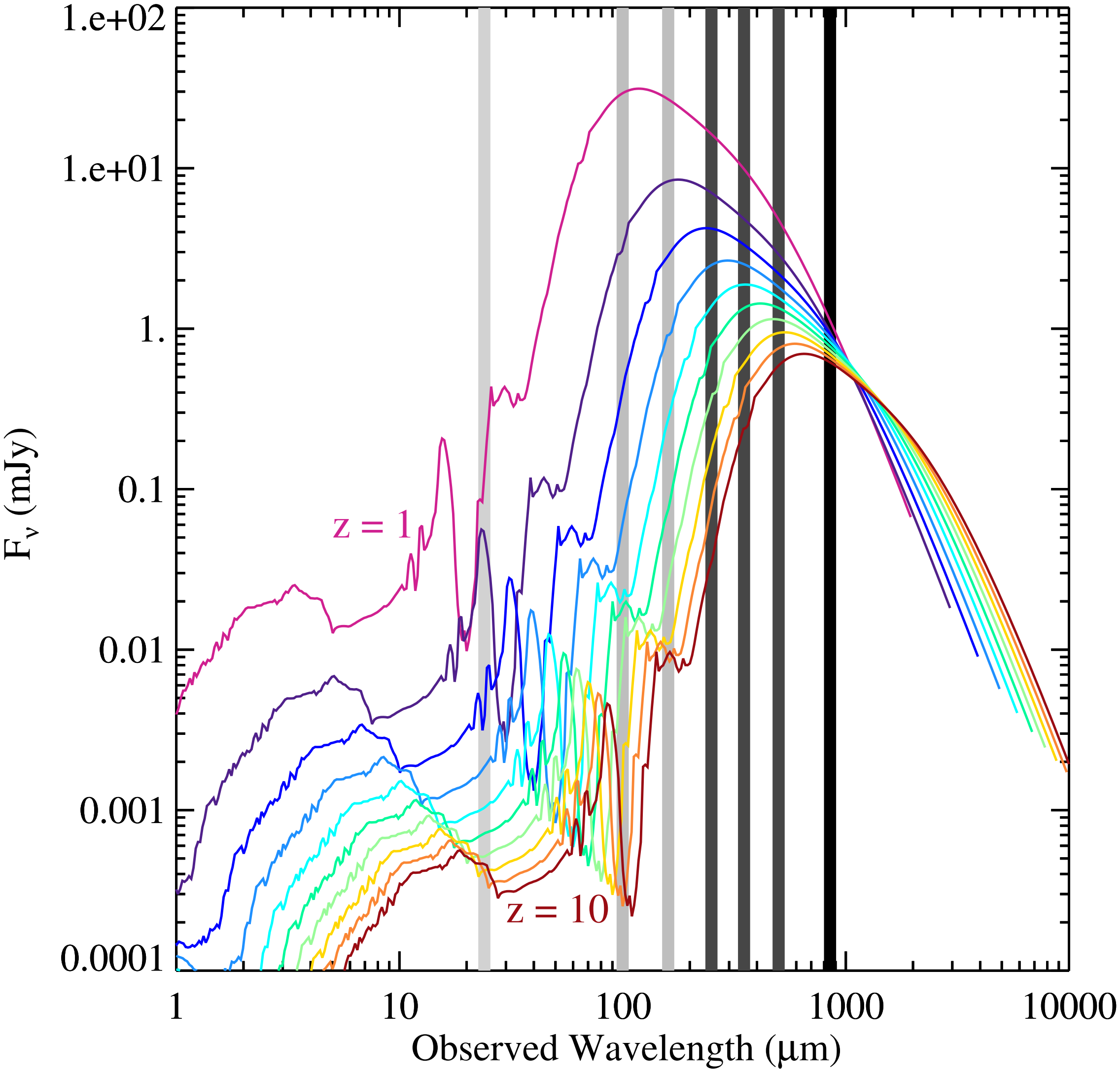

Figure 1.4 The spectral energy distribution for Arp220, a local ULIRG, redshifted from $z = 1.0$ (pink) to $z = 10.0$ (red). The bands correspond to the wavelengths addressed in this thesis: 24 μm (*Spitzer*-MIPS); 100, 160 μm (*Herschel*-PACS); 250, 350, 500 μm (*Herschel*-SPIRE); and 850 μm (SCUBA-2). The 850 μm flux is nearly constant at all redshifts from redshifts 1–10 due to the negative k-correction, while the other bands all suffer from cosmological dimming to some extent.

2

METHODOLOGY

2.1 CLUSTER SURVEYS

In order to accurately assess the importance of cluster environment on constituent galaxies, homogenous samples of clusters over cosmic time and mass are essential. Historically, cluster finding techniques have relied on X-ray or optical observations; however, recently, near-infrared and millimetre studies have opened a new window on the high-redshift Universe. Each method offers its own advantages and probes a slightly different cluster population due to varying selection functions.

Optical studies pioneered the field of galaxy cluster surveys over 50 years ago with photographic plates (Abell, 1958; Zwicky et al., 1968; Gunn et al., 1986), but were limited to low redshift. A resurgence of the field occurred with the development of large charge-coupled devices (e.g., Lidman and Peterson, 1996; Postman et al., 1996). These surveys were complementary to concurrent X-ray studies as they were sensitive to optically-rich but potentially X-ray-weak clusters (Castander et al., 1994). However, they suffered from high false-positive rates due to projection effects. This contamination can also adversely affect the cluster mass estimate, which is based on the cluster richness—typically defined as the number of galaxies within the detection aperture normalized by the luminosity function. The parameter often used to estimate the optical richness is $B_{\rm gc}$, defined as the amplitude of the correlation function between the cluster center and photometrically or spectroscopically confirmed cluster members (Yee and López-Cruz, 1999).

A more robust estimate of cluster mass, free of projection-induced contamination, arises from X-ray observables. The majority of baryons in the Universe are confined to the regions between galaxies, within the diffuse gas of the intracluster medium. This hot ionized gas ($\sim 10^7$ K) emits Bremsstrahlung radiation and thus becomes luminous at X-ray wavelengths in spatially extended regions, making clusters detectable with X-ray satellites, such as *Einstein* (e.g., Gioia et al., 1990), *ROSAT*, (e.g., Ebeling et al., 1998, 2001; Böhringer et al., 2000, 2001) and more recently, *XMM-Newton* (e.g., Romer et al., 2001; Mehrtens et al., 2012) and *Chandra* (e.g., Giacconi et al., 2002). As the X-ray emissivity is proportional to the gas temperature and the square of the electron density, it provides a clean estimate of the cluster mass (which dominates the baryonic mass by $\sim$ 10 times) (Böhringer and Werner, 2010); however, observations are expensive as they must be conducted from space, hindering the ability to detect rarer high-redshift clusters as the cosmological dimming increases.

Recently, more than 1000 cluster candidates have been identified via ground- and space-based millimeter-wave telescopes: the South Pole Telescope (SPT; Vanderlinde et al., 2010; Reichardt et al., 2013), the Atacama Cosmology Telescope (ACT; Marriage et al., 2011; Hasselfield et al., 2013), and the Planck Satellite (Planck Collaboration et al., 2011, 2013). These dedicated experiments were designed to detect the Sunyaev-Zel'dovich (SZ) effect, a distortion in the Cosmic Microwave Background spectrum as photons scatter off the hot thermal distribution of electrons in the intracluster medium of a massive galaxy cluster and gain a boost of energy. The amplitude of the thermal distortion in the Planckian spectrum stems from the amount of time the photon spends in the electron distribution and is proportional to the kinetic pressure of the ICM gas along the line of sight. Therefore, integrating the thermal SZ distortion over the solid angle of the cluster yields an estimate of the total number of electrons in the cluster weighted by temperature, or equivalently, the total thermal energy of the cluster. Thus, the thermal SZ detection is not dependent on redshift, but rather, is limited by cluster mass. Although the CMB itself suffers cosmological dimming with redshift, the ratio of the SZ effect to the CMB is impervious to this effect, allowing for the detection of high redshift clusters above a certain mass threshold (Carlstrom et al., 2002).

While both X-ray and SZ cluster surveys suffer from less projection contamination than optical cluster detection, they have their own limitations. Specifically, wide-field X-ray surveys are usually restricted to lower-redshift clusters, as deep wide-field X-ray observations are too expensive from space to conduct blind high-redshift cluster searches. SZ surveys overcome this shortfall, but are only sensitive to the most massive clusters at all redshifts, typically only complete above $M_{500} \sim 5 \times 10^{14}\,\mathrm{M}_{\odot}$ (Reichardt et al., 2013).

2.1.1 The Red-sequence Cluster Survey

In order to benefit from the affordable nature of wide-field optical surveys, and simultaneously thwart contamination from projection effects, Gladders and Yee (2000) developed a two-filter algorithm called the Cluster Red-Sequence (CRS) method. The technique relies on the homogeneous nature of starlight from elliptical cluster galaxies on a colour-magnitude diagram with very little scatter (Bower et al., 1992; Smail et al., 1998). These galaxies are dominated by old stellar populations, and exhibit strong metal absorption lines just below 4000 Å as they lack young, hotter stars to fill in absorbed flux (Poggianti and Barbaro, 1997). This produces a strong discontinuity in the spectrum, with the depth of the break (D4000) indicating the time since the last starburst. As such, cluster ellipticals display the reddest colours at any given redshift, in stark contrast to star-forming field galaxies (see Figure 2.1).

Furthermore, elliptical galaxies dominate the bright end of the cluster luminosity function (e.g., Barger et al., 1998a) and increase in luminosity (for a given size) toward higher redshift (e.g., Schade et al., 1997); they therefore possess a high detectability rate in flux-limited samples. As galaxy density increases radially toward dynamically relaxed clusters (Dressler et al., 1997), elliptical galaxies also provide a natural tracer of dense cluster overdensities.

Given the aforementioned properties, the CRS method can effectively sift through large volumes of observations in two filters bracketing the 4000-Å break and pinpoint clusters via simultaneous overdensities of colour, magnitude, and angular position, thereby eliminating contamination from projection ($< 5\%$; Gilbank et al., 2007). Moreover, the colour of this elliptical-populated red sequence evolves with time and can therefore serve as a photometric redshift estimator to an accuracy of 10% (Gladders and Yee, 2000).

The first Red-Sequence Cluster Survey (RCS1; Gladders and Yee, 2005) exploited this method to produce a large, uniform sample of ~ 1000 galaxy clusters over 92 square degrees. The observations utilize the CFH12K camera on the Canada-France-Hawaii Telescope (CFHT) and the MOSAIC-II instrument on the 4 meter Cerro Tololo Inter-American Observatory (CTIO). The two filters, centered at 6500 Å (R_c) and 9100 Å (z'), sample the 4000-Å break up to $z \sim 1.2$.

Building on the success of RCS-1, the second Red-Sequence Cluster Survey was launched (RCS2; Yee et al., 2007; Gilbank et al., 2011) with a ten-fold increase in survey area. Imaging was taken over ~ 1000 square degrees with MegaCam (Boulade et al., 2003) on the CFHT using the z' and r' filters, with the inclusion of the g filter for optimizing the colours of $z < 0.4$ clusters.

Both generations of the RCS have spawned numerous scientific results: including the measurement of weak-lensing signals over a large cluster survey (Hoekstra et al., 2002b), thereby constraining various cosmological parameters (Hoekstra et al., 2002a); the discovery of numerous strong lensing high-redshift clusters with multiple arc systems (Gladders et al., 2003); the discovery of a $z = 0.9$ supercluster (Gilbank et al., 2008; Faloon et al., 2013); and the evolution of the integrated star formation in clusters per cluster mass out to $z \sim 1$ (Webb et al., 2013). However, it is becoming clear that cluster surveys must be extended beyond $z \sim 1$ to understand environmental processes through a narrative of galaxy evolution.

2.1.2 The Spitzer Adaptation of the Red-sequence Cluster Survey

To this end, the Spitzer Adaptation of the Red-sequence Cluster Survey (SpARCS) incorporated infrared imaging to the red sequence method in order to extend cluster surveys to $z > 1$. At higher redshifts, the z' filter traverses the 4000-Å break to the blue-ward side. Therefore, a longer wavelength filter is required to detect red ellipticals in $z \gtrsim 1.2$ clusters. The advent of the Infrared Array Camera (IRAC; Fazio et al., 2004) aboard the *Spitzer Space Telescope* (Werner et al., 2004) offered a means with which to explore high-redshift clusters, given its sensitivity and fairly large field of view of $5.2' \times 5.2'$ over four passbands at 3.6, 4.5, 5.8, and 8.0 μm.

The first studies to harness this technique with *Spitzer* were carried out over small areas (< 9 deg^2), but quickly demonstrated the great potential of infrared cluster detection (e.g., Stanford et al., 2005; Brodwin et al., 2006; Wilson et al., 2006; Eisenhardt et al., 2008; Muzzin et al., 2008). However, clusters become more rare at high redshift, and deep, large field surveys are required to systematically detect a significant sample. The 50 deg^2 *Spitzer* Wide-area Infrared Extragalatic Survey (SWIRE; Lonsdale et al., 2003; Surace et al., 2005) affords this opportunity with sufficiently deep imaging over seven passbands: the four IRAC channels, and additionally, the Multiband Imaging Photometer for *Spitzer* (MIPS; Rieke et al., 2004) at 24, 70, and 160 μm.

The 3.6 μm filter provides the most sensitive *Spitzer* channel for $z > 1$ cluster detection on the red-ward side of the rest-frame 4000-Å break, while z' offers a complementary blue filter, as even by $z = 2$, it only gets as blue as ~ 3000 Å. The SpARCS collaboration obtained deep z' imaging (~ 24 AB) from MegaCam on CFHT for the

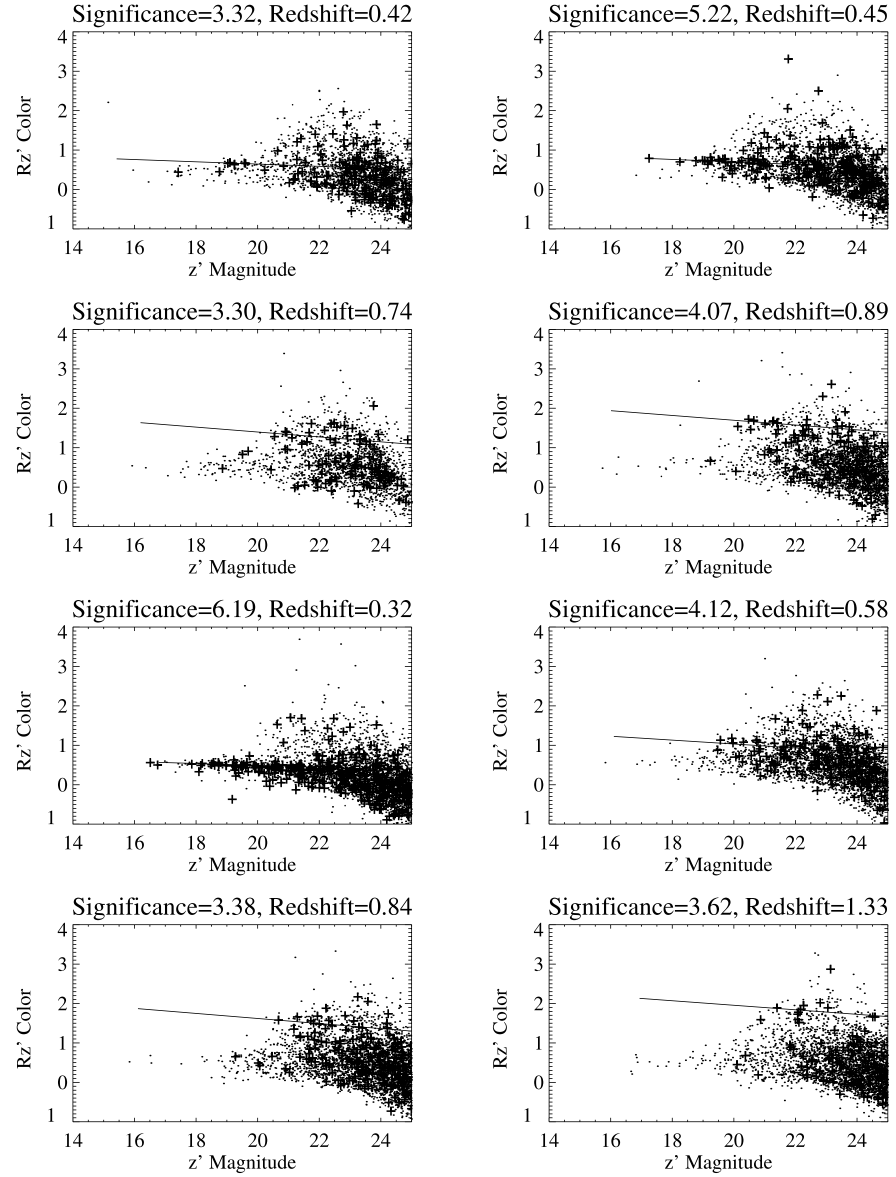

Figure 2.1 Colour magnitude diagrams illustrating the power of the cluster red sequence method in the RCS1 survey, over a wide range of redshift. The thicker points correspond to all galaxies within 0.5 Mpc of the cluster center. The solid line depicts the fiducial red sequence, estimated from the Bruzual and Charlot (1993) stellar population models with a 0.1 Gyr starburst ending at $z = 2.5$. Taken from Gladders and Yee (2005).

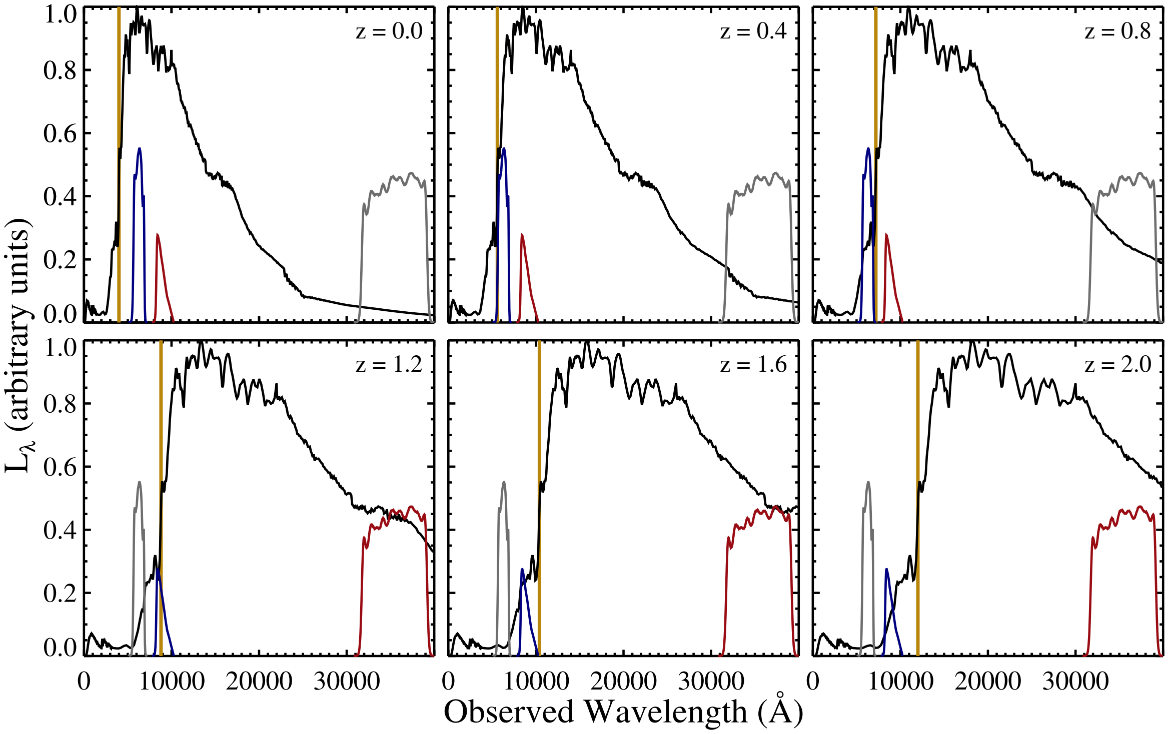

Figure 2.2 The evolution of the spectral energy distribution of an elliptical galaxy template from $z = 0$ to $z = 2.0$, with the redshifted value of 4000 Å highlighted with gold. The observed transmission filters for r' and z' from the CFHT, along with 3.6 μm from IRAC, are shown with ascending wavelength, respectively. The upper panel illustrates the success of RCS at $z < 1$ with r' (blue) and z' (red), while the bottom panel depicts why IRAC is necessary to replace z' as the red filter at $z > 1$. Also clear is the monotonic increase towards red colours using the respective filters for each wavelength regime, yielding a non-degenerate photometric estimate of the cluster redshift.

four northern SWIRE fields and MOSAICII on the Blanco telescope at CTIO for the two southern fields, yielding a total survey area of 41.9 deg^2 with both 3.6 μm and z' data. SpARCS has successfully identified > 200 massive ($\gtrsim 10^{14}\,\mathrm{M}_\odot$) cluster candidates up to $z \sim 1.4$ with this method (deeper z' imaging is needed beyond $z \sim 1.4$ as the $z' - 3.6$ μm colour becomes very red; Muzzin et al., 2013). This represents an impressive data set; only a handful of clusters have thus far been detected above

$z \sim 1.4$ (e.g., Stanford et al., 2005; Papovich et al., 2010; Tanaka et al., 2010; Stanford et al., 2012; Zeimann et al., 2012; Muzzin et al., 2013; Newman et al., 2013), with the current limit for a spectroscopically-confirmed cluster at $z \sim 2$ (Gobat et al., 2011). Spectroscopic confirmation of individual cluster galaxies is crucial for properly assessing environmental effects in this redshift range.

The first six spectroscopically confirmed SpARCS clusters were presented in Muzzin et al. (2009) at $z = 1.1798$ and $z = 1.1963$; Wilson et al. (2009) at $z = 1.335$; and Demarco et al. (2010) at $z = 0.871$, $z = 1.161$, and $z = 1.210$. More recently, the SpARCS team embarked on an ambitious spectroscopic and photometric follow-up survey of some of the richest candidate clusters over the range $0.85 < z < 1.2$: the Gemini Cluster Astrophysics Spectroscopic Survey (GCLASS; Muzzin et al., 2012). This program has successfully obtained redshifts for ~ 800 galaxies within ten rich cluster fields, including ~ 430 cluster members, utilizing the Gemini Multi-Object Spectrographs (GMOS) on 8.1 meter telescopes at the both the northern and southern Gemini Observatories. The slits were prioritized based on three criteria: low clustercentric radius; proximity in observed $z' - 3.6$ μm colour to the cluster red-sequence; and higher 3.6 μm flux. A 3.6 μm-flux selected sample is advantageous at $z \sim 1$ as it probes rest-frame H band (1.6μm) and is thus similar to a stellar mass limited sample.

The extensive spectroscopy in GCLASS also allows for an estimate of the dynamical cluster mass via the velocity dispersion, σ_v. The basic process involves isolating cluster members from nearby field galaxies by using a friends-of-friends algorithm within a specified velocity width, and slowly incrementing the width. This is repeated until the distribution of galaxies is no longer Gaussian at 95% confidence, as determined from a Shapiro-Wilk test (G. Wilson et al., in preparation). From the estimated velocity dispersion, R_{200}, the radius at which density is 200 times the critical density of the Universe, $\rho_c(z)$, is estimated using the relation in Carlberg et al.

(1997):

$$R_{200} = \frac{\sqrt{3}\sigma_v}{10H(z)}, \tag{2.1}$$

where $H(z)$ is the value of the Hubble parameter at redshift z. The dynamical mass contained within R_{200} is then given by:

$$M_{200} = \frac{4}{3}\pi R_{200}^3 \times 200\rho_c. \tag{2.2}$$

SpARCS and GCLASS have generated many important science results: Muzzin et al. (2012) analyzed $z \sim 1$ environmental effects in optical star-forming galaxies; Lidman et al. (2012) calculated a factor of 1.8 growth in stellar mass of brightest cluster galaxies from $z = 0.9$ to $z = 0.2$, most likely due to major mergers (Lidman et al., 2013); Muzzin et al. (2013) discovered a rich $z = 1.63$ cluster using an improved detection method that incorporates 4.5 μm imaging for $z > 1.4$ clusters; van der Burg et al. (2013) measured the stellar mass functions for quiescent and star-forming galaxies and found that although each population has a similar shape in both clusters and the field, 45% of star-forming galaxies are quenched by the cluster. Each of these studies focuses on the extensive optical to near-infrared imaging of SpARCS/GCLASS clusters. In this thesis, we focus on results from an infrared/submillimetre perspective of high-redshift clusters, which measures dust-enshrouded star formation, ultizing the GCLASS survey in Chapters 3 and 4, and the RCS in Chapter 5.

2.2 INFRARED LUMINOSITY AND STAR FORMATION RATES

A major objective in the study of galaxy evolution is to trace the nodes of star formation in the Universe over cosmic time, in order to relate them to the underlying environment and structure formation. Since much of this activity occurs within dusty regions, infrared and submillimetre observations (1—1000 μm), which are not plagued by extinction, are crucial. Moreover, since (U)LIRGs emit $\gtrsim$70–90% of their bolometric luminosity at far-infrared wavelengths ($40 \lesssim \lambda \lesssim 400\,\mu$m), accurate star formation rates must account for this dust-enshrouded activity. However, the large beams (i.e., poor resolution) at longer wavelengths ($\gtrsim 200\,\mu$m) can compromise reliable star formation estimates due to high confusion and blending with multiple sources (though ALMA can now help alleviate this issue). The mid-infrared regime (5–40 μm), on the other hand, offers better resolution and is also directly correlated with UV starlight: the low heat capacity of small dust grains that comprise the infrared continuum implies that they are stochastically heated by the ambient radiation field, even by single photons. AGN also contribute to dust heating at these wavelengths, but can be identified through infrared colours (e.g., Lacy et al., 2004).

Using *IRAS* data, Chary and Elbaz (2001) illustrated the potential of deriving the total infrared luminosity (8–1000 μm) in (U)LIRGs from a single continuum measurement in the mid-infrared. Given the strong evolution of the mid-infrared luminosity function with redshift, $L_{\rm MIR} \propto (1+z)^{4.5}$ (e.g., Xu, 2000), they developed a set of 105 spectral energy distributions of varying luminosity classes, fit to observational data from the Infrared Camera (ISOCAM) on *ISO*, *IRAS*, and SCUBA. These templates can then be normalized to the measured mid-infrared flux to find the best fit infrared luminosity at a given redshift. However, these templates have been calibrated to local galaxies, therefore, any unaccounted-for evolution in the spectral energy distributions could lead to inaccurate measurements of the total infrared luminosity.

With the advent of the *Herschel* Space Observatory, improved characterization of the peak of the thermal spectral energy distribution (70–500 μm rest-frame) has become feasible. The 24-μm extrapolated infrared luminosity from the Chary and Elbaz (2001) templates has now been confirmed to be an accurate representation for (U)LIRGS up to $z \simeq 1.3$ using extensive *Herschel* data (Elbaz et al., 2010, 2011). However, beyond this redshift, 24 μm falls into the PAH-dominated region of the spectrum, causing highly variable scatter in the extrapolated luminosities. In particular, there seems to be a mid-infrared excess at high redshifts, with monochromatically-extrapolated luminosities overestimated by factors of 2–7 (Elbaz et al., 2010; Nordon et al., 2010). Elbaz et al. (2011) attributes this excess to a secondary branch of SEDs for starburst galaxies with compact activity.

Once the infrared luminosity is determined, either through single-band extrapolation or thermal spectral energy distribution fits, it can be converted into a star formation rate using stellar population synthesis models. These are created from the temporal evolution of spectral luminosity models for a range of stellar masses, that are weighted by an initial mass function (see Section 2.3) and summed. Assuming continuous bursts of star formation that last 10–1000 Myr and synthesis models from Leitherer and Heckman (1995), Kennicutt (1998b) derived a simple relation between the infrared luminosity and star formation rate for starbursts:

$$\begin{aligned} \mathrm{SFR}\ (\mathrm{M_\odot\,yr^{-1}}) &= 4.5 \times 10^{-44} L_{\mathrm{IR}}\ (\mathrm{ergs\,s^{-1}}) \qquad (2.3) \\ &= 1.7 \times 10^{-10} L_{\mathrm{IR}}\ (\mathrm{L_\odot}), \qquad (2.4) \end{aligned}$$

where $\mathrm{L_{IR}}$ represents the total integrated luminosity from rest-frame 8–1000 μm. This relation assumes that young stars are the dominant contributors to the interstellar radiation field that heats the dust, which is a good approximation for dense circumnuclear starbursts; an older stellar population would most likely reduce the value of the coefficient (Kennicutt, 1998a).

Often, a more useful parameter for studying galaxy evolution is given by the star formation rate per unit stellar mass, known as the specific star formation rate (SSFR). The SSFR is a proxy for the timescale in which a galaxy will double its mass, given its current star formation rate:

$$\tau\ (Gyr) = \frac{M_\star\ (\mathrm{M_\odot})}{SFR\ (\mathrm{M_\odot\,Gyr^{-1}})} = \frac{1}{SSFR\ (\mathrm{Gyr^{-1}})}. \qquad (2.5)$$

The efficiency of a typical galaxy in converting gas into stars is fairly universal for all stellar masses; the narrow locus of specific star formation rates with mass at a given redshift has been coined the star-forming main-sequence (Noeske et al., 2007; Elbaz et al., 2007; Daddi et al., 2007). Galaxies that fall significantly off this trend are typically powered by an active galactic nucleus or burst of star formation.

2.3 Stellar Masses

Galactic evolution is inherently tied to stellar mass, which traces the chemical enrichment, baryonic content, and ultimately, the star-formation history of the galaxy. As such, determining accurate stellar masses has garnered much attention in the field, all of which rely on estimating stellar mass-to-light-ratios (M/L) of galaxies.

If extensive multi-wavelength data are available, fitting the spectral energy distribution from ultraviolet to near-infrared can yield robust stellar masses within 0.3 dex (Conroy, 2013). This approach, pioneered by Sawicki and Yee (1998) and Giallongo et al. (1998), utilizes broadband colours to find the best fit stellar population synthesis model for a given star formation history and metallicity to extract the M/L. This can then be multiplied by the luminosity to obtain a stellar mass.

A simpler technique employs only two filters to estimate the M/L from colour, drawing on the formative work of Bell and de Jong (2001). They showed that there is a strong correlation between M/L and colour, regardless of the star formation history, and that dust-reddening vectors are parallel to this relation, meaning it is not significantly affected by extinction. This occurs as dust dims the light while simultaneously reddening the colour (which acts to increase the M/L ratio), thereby canceling the effect out to first order. Therefore, robust stellar masses can be determined from the colour with negligible effect from dust extinction. Near-infrared photometry is the logical choice for colour estimates, as long-lived low-mass stars, which dominate the mass distribution, peak at near-infrared wavelengths. Moreover, K'-band luminosity

($\sim$2.2 μm) is less affected by extinction than optical light by a factor of 5–10 (Bell and de Jong, 2001; Bell et al., 2003). Many studies have corroborated the strong correlation between near-infrared luminosity and stellar mass: Kauffmann and Charlot (1998) showed that the K'-band can predict stellar masses out to $z \sim 2$, only varying within a factor of two between different star formation histories; Verheijen (2001) found that K' magnitudes are the best tracers of dark matter halo masses.

Alternatively, Kauffmann et al. (2003a) developed a novel procedure to constrain stellar masses in 10^5 galaxies in the Sloan Digital Sky Survey through two spectral absorption features: the strength of the 4000 Å break (D4000) and the Balmer line Hδ. The former is a proxy for stellar age, as the opacity blue-ward of the break increases for old metal-rich stellar populations. The latter determines if a burst of star formation occurred sometime within the last Gyr. The D4000-Hδ plane shows little dependence on metallicity or dust, while simultaneously providing a handle on the elapsed time since the most recent burst, thus making it a good predictor of M/L ratios.

The SpARCS-GCLASS team has adopted a similar method to both Bell and de Jong (2001) and Kauffmann et al. (2003a), but without the reliance on the Hδ absorption line; it is too weak to measure in faint galaxies with low signal-to-noise spectra, and, in the cluster redshift range ($0.8 < z < 1.4$), it is shifted into a region with many sky emission lines, further complicating the situation. Therefore a M/L ratio is inferred solely from D4000, which is fairly insensitive to dust extinction effects for a range of star formation histories. The benefits of near-infrared wavelengths are also exploited by using the observed 3.6 μm luminosity to determine the M/L ratio, as this roughly corresponds to rest-frame H- and K-band within the redshift range of interest. The predicted M/L ratios for a given D4000 are computed from the Bruzual and Charlot (2003) stellar population synthesis models, assuming solar metallicity, a Chabrier initial mass function (Chabrier, 2003), and an exponential decline in star formation, SFR $\propto e^{-t/\tau}$. A star formation timescale of $\tau = 0.3$ Gyr is adopted; this timescale model is used in many high-redshift studies (e.g., Förster Schreiber et al., 2004; Marchesini et al., 2009). Further details are provided in Muzzin et al. (2012).

While many studies from the nearby Universe (e.g., Kauffmann et al., 2003a; Bell et al., 2003) to z ∼4–5 (e.g., Pérez-González et al., 2008; Marchesini et al., 2009) have exploited these techniques to examine the stellar mass function, they are not without faults; specifically, stellar synthesis models must assume a dust extinction law (usually the Calzetti law; Calzetti et al., 2000), a metallicity, and an initial mass function, all of which introduce various systematic uncertainties in mass estimates. The last parameter has undergone particular examination (see e.g., Bastian et al., 2010 for a thorough review) as it is often the largest source of uncertainty, and therefore deserves a brief discussion.

The initial mass function (IMF; ϕ) describes the number of stars in a galaxy as a function of mass, often in logarithmic bins. This seminal work of Salpeter (1955) predicted a single power-law for the IMF based on main-sequence stars in the solar neighborhood, with contributions from stars over the range 0.1–100 $\mathrm{M}_\odot$:

$$\phi(\log m) = \frac{dN}{d\log m} \propto m^{\Gamma}, \tag{2.6}$$

where $\Gamma \sim 1.35$, and $dN/d\log m$ is the number of stars in a given logarithmic mass bin. A few decades later, two additional functional forms for the IMF were introduced as precision measurements of low mass stars became more feasible, though the Salpeter relation still remains as one of the more widely adopted forms. As a slight alteration to the Salpeter IMF, a segmented power-law was proposed, which was found to be a better fit empirically for the low-mass end of the IMF, typically at $M < 1\,\mathrm{M}_\odot$ (Kroupa et al., 1993; Kroupa, 2001) .

Another popular representation of the IMF is in log-normal form, first suggested by Miller and Scalo (1979), and more recently popularized by Chabrier (2003). This form usually assumes a power-law given by the Salpeter IMF above a high-mass break ($\sim$1 M$_\odot$), and a Gaussian distribution in logarithmic mass below:

$$\phi(\log m) \propto \exp\left[-\frac{(\log m - \log m_c)^2}{2\sigma^2}\right], \tag{2.7}$$

where m_c is a characteristic mean mass, and σ^2 is the variance in $\log m$. These IMFs (Kroupa/Chabrier) are sometimes referred to as bottom-light, given their shallower slope compared to the Salpeter IMF at low masses. As a result of having fewer low mass stars, Kroupa- and Chabrier-based IMFs predict lower stellar masses and star formation rates, by a factor of 1.4–1.8, for a given luminosity (Chabrier, 2003; Kennicutt et al., 2009).

The SpARCS-GCLASS team has adopted the Chabrier IMF in stellar population synthesis models to ultimately derive stellar masses. This is a logical choice given numerous studies of similar objects that find bottom-light IMFs to be a better representation of their data. For example, Goldader et al. (1997) found that the steeper Salpeter slope below 1 M$_\odot$ underpredicts gas depletion timescales for a sample of ULIRGS. On the other hand, fewer low mass stars (i.e., from a bottom-light IMF) would result in lower SFRs and thus longer gas consumption times. Tacconi et al. (2008) also favor a Chabrier IMF for $z \sim 2$ SMGs and star-forming galaxies, suggesting the existence of a universal IMF. Moreover, by comparing dynamical masses of $z \sim 2$ early-type galaxies with those from stellar synthesis population models, Cappellari et al. (2009) find consistency with a Kroupa/Chabrier, or bottom-light, IMF.

3

A Kinematic Study of Infrared Galaxies in a $z \sim 0.9$ Cluster

In this chapter, we present an infrared study of a $z = 0.872$ cluster, SpARCS J161314+564930, with the primary aim of distinguishing the dynamical histories of spectroscopically confirmed star-forming members to assess the role of cluster environment. We utilize deep MIPS imaging and a mass-limited sample of 85 spectroscopic members to identify 16 $24\,\mu$m-bright sources within the cluster, and measure their $24\,\mu$m star formation rates (SFRs) down to $\sim 6\,\mathrm{M}_{\odot}\,\mathrm{yr}^{-1}$. Based on their line-of-sight velocities and stellar ages, MIPS cluster members appear to be an infalling population that was recently accreted from the field with minimal environmental dependency on their star formation. However, we identify a double-sequenced distribution of star-forming galaxies amongst the members, with one branch exhibiting declining specific SFRs with mass. The members along this sub-main sequence contain spectral features suggestive of passive galaxies. Using caustic diagrams, we kinematically identify these galaxies as a virialized and/or backsplash population. Moreover, we find a mix of dynamical histories at all projected radii, indicating that standard definitions of environment (i.e., radius and density) are contaminated with recently accreted interlopers, which could contribute to a lack of environmental trends for star-forming galaxies. A cleaner narrative of their dynamical past begins to unfold when using a proxy for accretion histories through profiles of constant $(r/r_{200}) \times (\Delta v/\sigma_v)$; galaxies accreted at earlier times possess lower values of $(r/r_{200}) \times (\Delta v/\sigma_v)$ with minimal contamination from the distinct infalling population. Therefore, adopting a time-averaged definition for density (as traced by accretion histories) rather than an instantaneous density yields a depressed specific SFR within the dynamical cluster core.

This work was originally published as:

“A Kinematic Approach to Assessing Environmental Effects: Star-forming Galaxies in a $z \sim 0.9$ SpARCS Cluster Using *Spitzer* 24 μm Observations”

Noble, A. G., Webb, T. M. A., Muzzin, A., Wilson, G., Yee, H. K. C., van der Burg, R. F. J., 2013, ApJ, 768, 118

3.1 Introduction

A hallmark of cosmology has been the establishment of hierarchical formation (White and Frenk, 1991) in which growth of structure in the Universe proceeds via a "bottom-up" scenario: matter condenses into low mass haloes which eventually merge to form larger structures, culminating with galaxy clusters. Clusters subsequently evolve through the accretion of galaxies and groups along cosmic filaments. This continual build-up of the cluster gives rise to distinct populations: a virialized component of older galaxies, and a younger population that was recently accreted from the surrounding low-density field (Balogh et al., 1998; Ellingson et al., 2001). As clusters are thought to be hostile environments, member galaxies are exposed to various mechanisms that could potentially suppress their star formation, including ram-pressure stripping (e.g., Gunn and Gott, 1972), strangulation (e.g., Larson et al., 1980), and galaxy harassment, perhaps preceded by an initial burst (e.g., Barnes and Hernquist, 1991; Moore et al., 1998). These mechanisms should induce marked differences in the young and in-situ population, as the latter has long endured the harsh conditions of the dense cluster.

Indeed, the local environment in which a galaxy resides is known to strongly correlate with several galaxy properties, such as star formation rate, stellar mass, colour, and morphology. Extensive observational efforts at low redshift have yielded a paradigm for galaxy dependencies, such that the densest regions at $z \sim 0$ are devoid of star formation activity (e.g., Gómez et al., 2003; Balogh et al., 2004a) and instead harbor massive (e.g., Kauffmann et al., 2004), red (e.g., Balogh et al., 2004b; Hogg et al., 2004; Baldry et al., 2006), early-type passive galaxies (Dressler, 1980).

Recently, the nature of these correlations at higher redshift, $z \sim 1$, has become a rather contentious issue. While it is well established that higher redshift clusters contain increased star formation activity compared to their local counterparts (e.g., Butcher and Oemler, 1978, 1984; Ellingson et al., 2001; Saintonge et al., 2008, Webb et al. in preparation) in parallel to the rapid decline of the cosmic star formation rate (SFR) since $z \sim 1$ (e.g., Lilly et al., 1996; Madau et al., 1996; Le Floc'h et al., 2005), there has not yet been a clear convergence on the SFR-density relation at this epoch. Some studies have observed a reversal of the $z \sim 0$ relation such that the predominant sites of star formation have migrated to denser regions by $z \sim 1$ (Elbaz et al., 2007; Cooper et al., 2008; Li et al., 2011), while many other groups find the local relation is already in place in $z \sim 1$ clusters (e.g., Patel et al., 2009, 2011; Koyama et al., 2010; Muzzin et al., 2012, Webb et al. in preparation). These discrepancies most likely stem from differing selection effects (stellar mass versus luminosity limited samples) and the varying degrees of densities probed (cluster versus group environments).

Moreover, the situation is muddled by the interdependence between environment and stellar mass—whether these correlations with environment are causal or incidental is still ambiguous, since massive galaxies preferentially reside in dense regions. Indeed, many properties seem to be also governed by stellar mass, including colour (e.g., Bell and de Jong, 2001; Kauffmann et al., 2003a) and SFR (e.g., Brinchmann et al., 2004; Noeske et al., 2007). As surveys have attempted to untangle this covariance between stellar mass and environment, a host of trends have been revealed to depend unilaterally on one, or equally on each property. For instance, both mass and environment have a separable effect on the fraction of star forming galaxies as seen by a decline in star-forming galaxies with increasing density and mass while the other parameter remains fixed (e.g., Poggianti et al., 2008; Peng et al., 2010; Sobral et al., 2011; Muzzin et al., 2012). In contrast, many studies have found that the specific star formation rate (SSFR; the star formation rate per stellar mass) for star-forming galaxies is correlated with stellar mass in different environments but fails to exhibit any dependence on the local environment (e.g., Kauffmann et al., 2004; Poggianti et al., 2008; Peng et al., 2010; Lu et al., 2012; Muzzin et al., 2012). A possible explanation for this discordance that has been adopted by many groups is a rapid quenching timescale that suddenly alters the host galaxy's star-forming classification (e.g., colour) preceding a decline in the observed SSFR (Peng et al., 2010; Muzzin et al., 2012; Wetzel et al., 2012).

Alternatively, a flat trend in SSFR with environment could suffer from radial projection effects. If radial/density bins harbor a mixture of both physically high and low radius galaxies, any correlation with star forming properties could potentially get washed out in projection space. Moreover, this could preferentially affect star forming galaxies over the quiescent population if they are inherently more biased towards radial contamination. This is similar to the rationale put forward by Patel et al. (2011), who attributed a declining SFR-density (over all quiescent and star-forming galaxies) at $0.6 < z < 0.9$ to a combination of two effects: a varying fraction of passive and active galaxies with density, and suppressed SFRs at higher densities.

The recent work of Haines et al. (2012) provides further insight into this contamination scenario via the accretion histories of cluster galaxies. Utilizing caustic diagrams from the Millennium Simulations, Haines et al. (2012) effectively isolate active galactic nuclei in projected velocity/radius space and determine that they are primarily an infalling population in spite of their low projected radii. Applying the results of accretion histories from their work could potentially incite the emergence of an alternative environmental trend for star-forming galaxies that relies on more of a time-averaged rather than an instantaneous definition of density.

Here, we present an infrared study of a $z = 0.872$ galaxy cluster drawn from the Spitzer Adaptation of the Red-sequence Cluster Survey (SpARCS; Wilson et al., 2009; Muzzin et al., 2009; Demarco et al., 2010). We utilize extensive optical spectroscopy (Muzzin et al., 2012) and deep *Spitzer*-MIPS $24\,\mu$m observations to pinpoint dusty star-forming cluster galaxies. By adapting a kinematic approach to the star formation histories of these galaxies via caustic diagrams, we intend to alleviate some of the confusion in environmental trends caused by radial projection effects.

The paper is outlined as follows. In §3.2 we present the SpARCS survey and 24 μm observations. We briefly describe our computation of stellar masses and star formation rates in §4.3. Our results are presented in §4.4, including stellar age, kinematic, and star formation trends. We discuss the implications of these trends in §3.5, and introduce a kinematic approach to classifying the star formation histories of cluster galaxies, along with a new interpretation of the environmental dependence on the SSFR of star-forming galaxies. We conclude in §4.5. Throughout the paper we assume a cosmology with $H_0 = 70\,\mathrm{km\,s^{-1}\,Mpc^{-1}}$, $\Omega_\mathrm{M} = 0.3$, $\Omega_\Lambda = 0.7$. Stellar masses and SFRs are based on a Chabrier initial mass function (Chabrier, 2003).

3.2 OBSERVATIONS AND DATA REDUCTION

3.2.1 The SpARCS Survey

The Spitzer Adaptation of the Red-sequence Cluster Survey (SpARCS) is a $\sim$ 45 sq. deg. survey with deep z'-band imaging from the CFHT and CTIO, designed to produce a large, homogeneously selected sample of massive galaxy clusters at $z > 1$. By combining the z'-passband observations with IRAC imaging from the Spitzer Wide-area InfraRed Extragalactic (SWIRE) survey, SpARCS has discovered high-z massive cluster candidates using either the red-sequence method (Gladders and Yee, 2000; Muzzin et al., 2008) or the stellar bump sequence method (Muzzin et al., 2013). With $\sim$ 200 massive cluster candidates, including ~ 12 $z > 1$ spectroscopically confirmed clusters (Wilson et al., 2009; Muzzin et al., 2009; Demarco et al., 2010), SpARCS currently has one of the largest repositories of $z > 1$ galaxy clusters.

3.2.2 SpARCS J161314+564930 and the GCLASS Cluster Sample

This work presents an infrared study of SpARCS J161314+564930, a rich galaxy cluster at $z = 0.872$ from the Gemini Cluster Astrophysics Spectroscopic Survey (GCLASS; Muzzin et al., 2012) that was discovered using the red-sequence method.

It is an extremely massive cluster with: a velocity dispersion of $1350 \pm 100\,\mathrm{km\,s^{-1}}$; r_{200}, the radius at which the cluster density is 200 times the critical density, of 2.1 ± 0.2 Mpc; and $\mathrm{M}_{200} = 26.1^{+6.3}_{-5.4} \times 10^{14}\,\mathrm{M}_{\odot}$ (Wilson et al. in preparation). This cluster field has ∼180 spectroscopic redshifts from GMOS-N on Gemini. Galaxies within $3375\,\mathrm{km\,s^{-1}}$ of the cluster velocity dispersion ($2.5\sigma_v$) are considered to belong to the cluster, yielding 95 confirmed cluster members. As GCLASS is a $3.6\,\mu$m-selected survey, the spectroscopic data is rest-frame H-band selected and therefore close to a stellar mass-selected sample. The final sample includes 85 cluster galaxies above our mass completeness limit of $2.0 \times 10^{9}\,\mathrm{M}_{\odot}$ (see §3.3.2).

3.2.3 Spitzer-MIPS Imaging

Our primary data set derives from the Multiband Imaging Photometer for *Spitzer* (MIPS; Rieke et al., 2004) aboard the *Spitzer Space Telescope* (Werner et al., 2004) at $24\,\mu$m with the aim to detect any dusty emission associated with the spectroscopically confirmed members. With a 5.4 sq. arcmin field of view, MIPS provides sufficient coverage of the entire spectroscopic area. The observations were part of the Guaranteed Time Observer program and completed in 2008 (proposal ID 50161) with an exposure of 1200 seconds per pixel. The MIPS image was reduced using a combination of the Spitzer Science Center's MOPEX software and a suite of IDL routines we developed to further optimize background subtraction (Webb et al. in preparation will provide more details).

3.2.4 Source Detection and Photometry

A source catalog of the entire MIPS field contains flux densities estimated with DAOPHOT (Stetson, 1987), and positions using a photometry pipeline (Yee, 1991). We plot the $24\,\mu$m differential number counts for our catalog in Figure 5.3; they are in good agreement with the published $24\,\mu$m counts from Papovich et al. (2004). We determine the catalog completeness limits by locating the flux at which our counts deviate by $> 2\sigma$ from the expected value of Papovich et al. (2004), which occurs at fluxes below $\sim$70 μJy. This corresponds to an infrared luminosity of $\sim 3 \times 10^{10}\,L_\odot$ at $z = 0.872$.

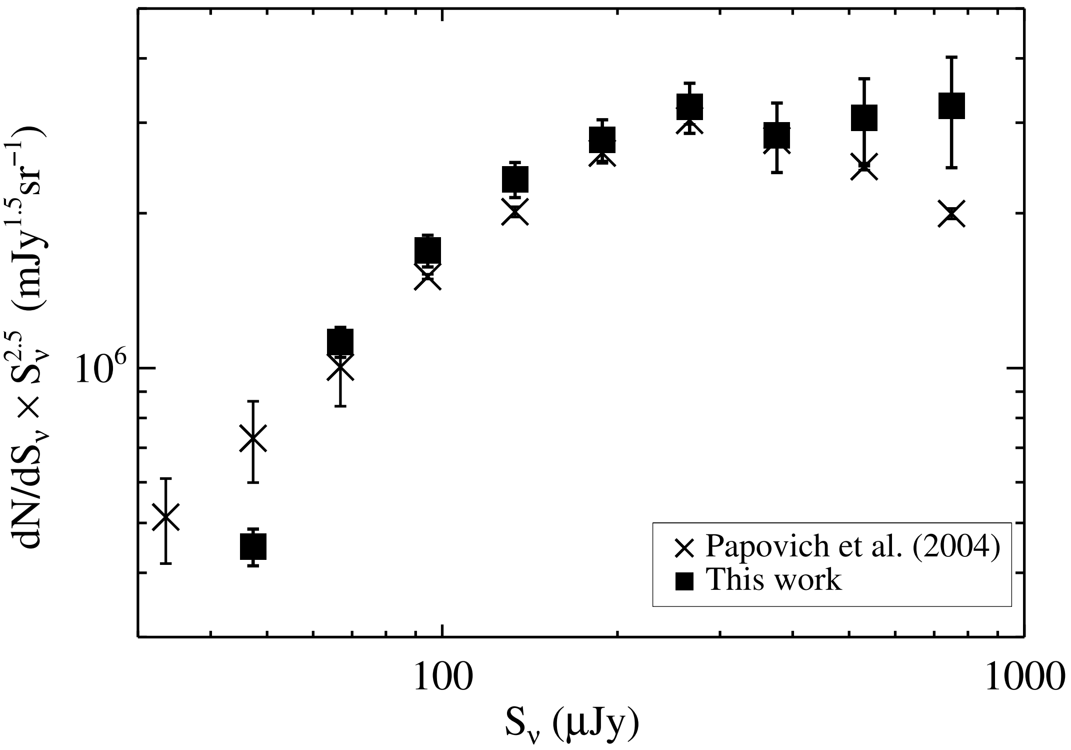

Figure 3.1 The 24 μm differential number counts of our catalog, normalized to the Euclidean slope (filled squares). We compare to published counts from Papovich et al. (2004) to determine a completeness limit of 70 μJy.

3.3 ANALYSIS

3.3.1 Counterpart Identification

We search for optical counterparts within $\sim 2''$ to locate cluster members with 24 μm emission; we detect 16 MIPS cluster members which constitute the focus of our study.

To quantify the number of chance alignments between $24\,\mu$m and optical sources, we drop $2''$ apertures at random positions on the MIPS field and count the number of times we find one or more source. We perform 100 realizations at each flux level within 40–400$\,\mu$Jy in $10\,\mu$Jy steps. At $70\,\mu$Jy, the completeness depth of our MIPS catalog, we expect 5% of MIPS counterparts to be falsely identified. This translates into one chance alignment in our counterpart sample of 16 MIPS cluster members.

In order to assess the effect of the cluster environment on its constituent galaxies, it is essential to have a control sample of field galaxies that are distinct from the cluster. Our spectroscopic campaign for the entire GCLASS survey successfully obtained redshifts for a significant number of foreground and background sources in the fields of the clusters with identical selection effects as cluster galaxies; these sources constitute our field sample (see Muzzin et al. 2012). We employ the same criteria to search for MIPS counterpart emission to the field and cluster galaxies, but restrict the field redshift range to $0.84 < z < 1.0$ in order to probe the same epoch as the $z = 0.872$ cluster. This leaves us with ten $24\,\mu$m-bright field galaxies above our flux limit.

3.3.2 Stellar Masses

We compute stellar masses using a technique similar to Bell and de Jong (2001) and Kauffmann et al. (2003a). In particular, we utilize a spectral feature that provides information on the age of the stellar population but is fairly insensitive to dust, the 4000-Å break. Using the Bruzual and Charlot (2003) stellar population synthesis models with solar metallicity, assuming a Chabrier IMF, and adopting a star formation timescale of $\tau = 0.3\,$Gyr, we infer a M/L ratio at $3.6\,\mu$m from the strength of the 4000-Å break. We than convert to a stellar mass using the measured $3.6\,\mu$m luminosity (for more details see Muzzin et al., 2012). In order to obtain a mass-limited sample, we do not include sources below our mass completeness limit of $2 \times 10^9\,\mathrm{M}_\odot$

(Muzzin et al., 2012).

3.3.3 24 μm Star Formation Rates

The mid-infrared luminosity of a galaxy probes thermal emission from dust grains that has been reprocessed from UV light, and therefore offers a clean measurement of the star formation rate (SFR) that is minimally affected by dust extinction (Kennicutt, 1998a). Moreover, rest-frame 24 μm traces dust heated by younger stars and therefore provides a measure of the instantaneous SFR (Calzetti et al., 2007). However, at $z = 0.872$, 24 μm corresponds to 13 μm rest-frame, which has recently been shown to contain a higher contribution of dust heated from intermediate age stars, which is evidence for star formation over longer timescales (∼1–2 Gyrs; Salim et al., 2009). As there is a rapid decline in the cosmic star formation since $z \sim 1$ (Lilly et al., 1996; Madau et al., 1996; Le Floc'h et al., 2005), this could result in an overestimate of the star formation as derived from observed 24 μm flux. In parallel, Rodighiero et al. (2010) found that extrapolating an infrared luminosity from the monochromatic 24 μm flux leads to an underestimate by a factor of $\sim$ 1.6 compared to Herschel measurements observed at 100 and 160 μm for $0.5 < z < 1.0$ galaxies. Despite some potential systematic effects in the 24 μm-derived SFRs, the results from this study are minimally affected, as we rely solely on relative differences within our own sample (see also Patel et al., 2011).

We calculate the 24 μm-derived SFR by converting the MIPS flux into a total infrared luminosity using an average of the Chary and Elbaz (2001) and Dale and Helou (2002) templates. We employ the relation in Kennicutt (1998a) to calculate a SFR and convert to a Chabrier-IMF based SFR using a factor of 1.65. Based on the depth of our MIPS images, we probe down to $\sim 6\,\mathrm{M}_\odot\,\mathrm{yr}^{-1}$.

3.3.4 Active Galactic Nucleus Contamination

We assume that the MIPS sources are dominated by star formation, with little or no contamination from active galactic nuclei (AGN); this seems reasonable given that only $\sim 5\%$ of infrared field galaxies at $z \sim 1$ have their total IR luminosity dominated by AGN emission (Fadda et al., 2010), and the contribution declines drastically with low mid-infrared flux. In fact, AGNs only begin to dominate the infrared emission for $24\,\mu$m fluxes above 1.2 mJy at $z \sim 0.8$, and are missing below 0.8 mJy (Fu et al., 2010). We note that our sample contains only two sources at the high flux end, at 0.83 mJy and 0.91 mJy, both of which are still below the level where AGNs prevail. Moreover, Martini et al. (2009) measured the occurrence of AGNs in cluster galaxies and found that while the AGN fraction increases with redshift, it is still only 1.5% at $z = 0.81$.

Regardless, we have performed two quick checks for obvious AGN sources. We first compare the equivalent width of the [OII] line and the depth of the 4000-Å break, following Stasińska et al. (2006). Our sample contains ten MIPS sources with measurable [OII] emission, all of which are all consistent with the normal star forming galaxies shown in fig. 7 from Stasińska et al. (2006). We also exploit infrared colour diagnostics (e.g., Lacy et al., 2004; Sajina et al., 2005) using data from the Infrared Array Camera (IRAC; Fazio et al., 2004). All but two MIPS cluster members display infrared colours consistent with stellar- and PAH-dominated sources (i.e., star-forming) at $z \sim 0.9$. The other two sources lie on the edge of the region encompassed by AGN, but we note there is a high contamination from PAH-dominated sources at this location; these are the same two sources described previously with high mid-infrared fluxes. In the absence of any concrete evidence for pure AGNs, we assume the MIPS flux is dominated by star formation.

3.4 RESULTS

This analysis presents an infrared study of a single GCLASS cluster at $z = 0.872$. As such, we focus primarily on the properties of the MIPS population and utilize the extensive spectroscopy for verification of MIPS cluster membership and an estimate of stellar age. We refer the reader to Muzzin et al. (2012) for a detailed description of the spectroscopic selection criteria and completeness, as well as a comprehensive analysis of the GCLASS clusters as seen through optical spectroscopic measures, for example, [OII] star-formation rates.

3.4.1 Age as a Function of Stellar Mass

Here we investigate the depth of the 4000-Å break (D4000) as a function of stellar mass for the MIPS-detected cluster members compared to the larger sample of spectroscopic members. The 4000-Å break, defined as the ratio of the integrated flux density at 4000 Å–4100 Å to that blue-ward of the break, 3850 Å–3950 Å (Balogh et al., 1999), arises from an accumulation of absorption lines and increases in depth for old and metal-rich stellar populations. It can therefore be used as a proxy for stellar age. In Figure 3.2 we plot the depth of the 4000-Å break for all cluster galaxies (filled circles), as well as a field population over the same epoch, $0.84 < z < 1.0$ (open squares). We highlight cluster and field galaxies detected at 24 μm with green diamonds. The MIPS cluster galaxies are primarily coincident with the coeval field population, spanning the same range of stellar mass and D4000. A Kolmogorov-Smirnov test between the MIPS cluster members and general field population reveals a 76% chance they derive from the same parent population, in stark contrast to that of cluster members without MIPS detections, where the null hypothesis is rejected at a high significance of 0.02%. Compared to the spectroscopically-confirmed members not detected at 24 μm, MIPS members form a young envelope of the cluster population at a given mass, which suggests they were recently accreted from the field.

We also distinguish between galaxies with [OII] emission and those without (i.e., below ~ 1 (3) Å equivalent width for the highest (lowest) signal-to-noise spectra); in Figure 3.2 cyan circles have measurable [OII] which is indicative of ongoing star formation, while purple circles represent quiescent (or extremely dust-enshrouded) galaxies. The majority of MIPS galaxies are [OII]-detected in the cluster and field, albeit at a slightly reduced fraction in the cluster (70 and 90%, respectively). This is not surprising given the recent conclusion from Webb et al. (in preparation) that optical studies are not significantly biased against dusty star formation. We define a D4000 limit of 1.4 (dotted line), above which $> 90\%$ of cluster members without [OII] emission reside, signifying a minimum age for the older, quiescent cluster galaxies. We note that a variable D4000 as a function of stellar mass does not significantly affect our conclusions, and therefore adopt the simpler flat delineation. In all subsequent plots, we differentiate galaxies by their nominal age as traced by the strength of the 4000-Å break, rather than [OII] detections as in Figure 3.2.

3.4.2 Relative Velocity as a Function of Radius

In the left panel of Figure 3.3 we plot the relative velocity of all cluster members as a function of clustercentric radius, as defined by the projected distance to the brightest cluster galaxy (BCG), the brightest $3.6\,\mu$m cluster member, which is also the most massive (see Lidman et al., 2012 for a detailed discussion of the BCG selection in SpARCS, including this cluster). As discussed in §3.4.1, we now separate the galaxies into old (red circles) and young (blue circles) cluster populations based on D4000, and highlight $24\,\mu$m-bright members with green diamonds. Barring two MIPS galaxies at low projected velocities and radii (both of which are classified as older), MIPS sources tend to display larger velocities on average ($|\overline{\Delta v}| = 1422 \pm 205.8\,\mathrm{km\,s^{-1}}$), in contrast to a tighter distribution expected from a virialized population ($|\overline{\Delta v}| = 995.1 \pm 89.60\,\mathrm{km\,s^{-1}}$ for older galaxies without a MIPS detection). Therefore, the

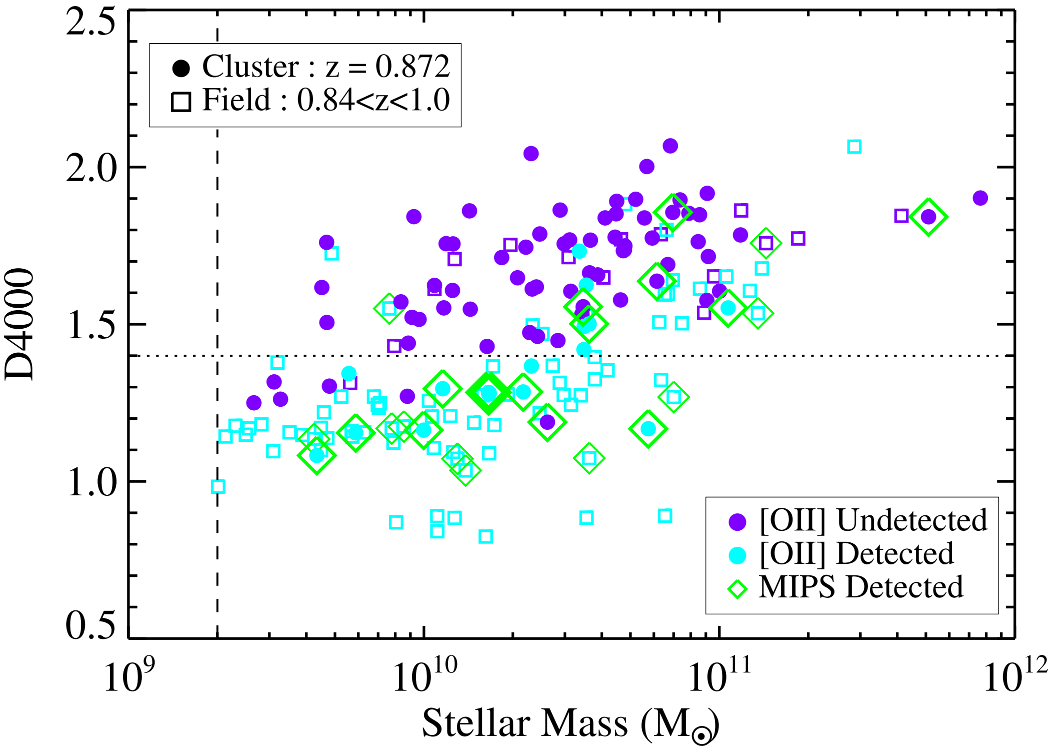

Figure 3.2 The strength of the 4000-Å break as a function of stellar mass for the cluster ($z = 0.872$; filled circles) and coeval field ($0.84 < z < 1.0$; open squares) population. The galaxies with [OII] emission (star forming) are plotted in cyan, while those without any [OII] emission are purple. A green diamond denotes coincident 24 μm emission; there are three MIPS detections, all with [OII] emission, at the location of the thickest green diamond with a D4000 of 1.3 and stellar mass of $\sim 1.7 \times 10^9$ $M_\odot$. The dashed vertical line illustrates our mass limit of 2.0×10^9 $M_\odot$, and the dotted horizontal line indicates our cut in D4000 in subsequent plots. We note that the two most massive cluster members have both been identified as the brightest cluster galaxies, although only one is detected at 24 μm.

velocity-radial space encompassed by MIPS galaxies further supports the idea that they have been recently accreted.

The histogram in the right panel of Figure 3.3 emphasizes this point: the older cluster population (red hashed histogram) displays a Gaussian distribution of velocities and primarily falls within the cluster velocity dispersion ($1350\,\mathrm{km\,s^{-1}}$), while the young (blue hashed histogram) and MIPS (solid green histogram) galaxy populations exhibit bimodal and/or flat distributions, peaking at velocities greater than $\pm 1000\,\mathrm{km\,s^{-1}}$. Moreover, the younger members within the cluster avoid the central velocity bin completely.

Given that 38% of MIPS cluster galaxies have a steep 4000-Å break with D4000 > 1.4 (red circles with green diamonds), we might expect to see some overlap in their velocities compared to those in the larger spectroscopic sample of older galaxies (i.e., the confirmed members that are not detected by MIPS; red circles without a green diamond). However, a Kolmogorov-Smirnov test between the velocities of all MIPS galaxies (green diamonds) and older cluster galaxies (the black histogram shows old cluster members with old MIPS sources removed) rejects the null hypothesis with marginal significance—there is only a 6% probability that the two distributions derive from the same parent population. It therefore seems likely that the MIPS galaxies trace a younger, recently accreted population that is not yet virialized with the cluster.

3.4.3 Environmental Dependence on the Specific Star Formation Rate

Given the implication that MIPS galaxies represent a younger, infalling population of cluster members, we might expect to detect a correlation between the specific star formation rate (SSFR; star formation rate per stellar mass) of MIPS galaxies and local environment. If the majority of MIPS galaxies do in fact belong to an infall population, there should be more star formation in the cluster outskirts compared to the cluster core, where galaxies have had their star formation shut off as they fall deep into the cluster.

In Figure 3.4, we plot the SSFR as a function of local environment, with binned averages shown in the lower panels. The upper panels show the SSFR for every MIPS

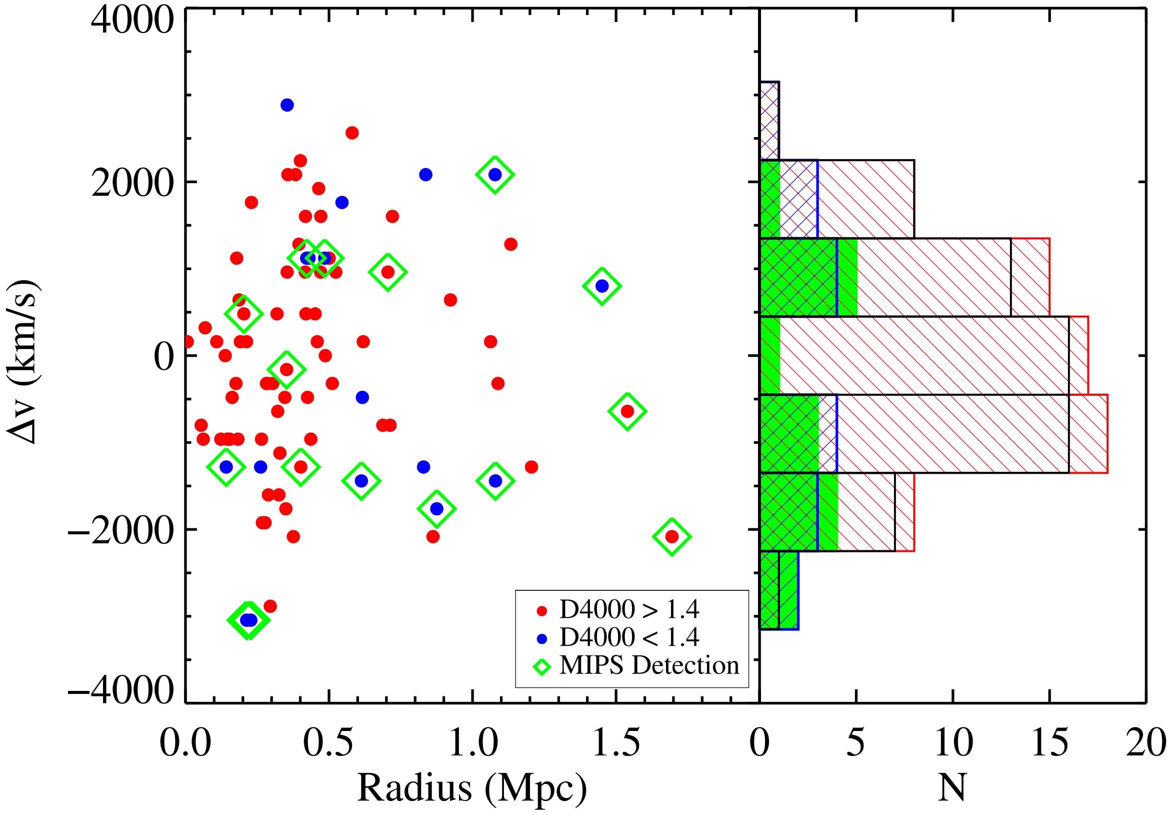

Figure 3.3 The relative velocity as a function of clustercentric radius for all spectroscopic members. Red circles corresponds to older galaxies with D4000 $>$ 1.4 and blue circles denote younger galaxies, D4000 $<$ 1.4. The histograms correspond to the number of galaxies within 900 $\mathrm{km\,s^{-1}}$ velocity bins; the colours correspond to the same types of galaxies in the legend on the left. The black histogram represents the population of old galaxies with the MIPS sources removed (6 in total). The green histogram shows all MIPS sources, regardless of age.

member (green stars), as well as an upper limit for every spectroscopic member, determined from the 3σ completeness limit of the SSFR for a given stellar mass. Errors on the averages are determined from 100 bootstrap resamplings of the data in each bin.

We use two different proxies for environment in order to compare to previous studies, and to confirm we are not substantially biased with either parameterization.

In the left panels we show clustercentric radius, where the core of the cluster is defined by the location of the BCG. The right panels contain local galaxy density calculated from the distance to the 10th nearest neighbor. Although in the literature these two parameters are often used interchangeably, they sample different mechanisms: the former is a better indicator of the global environment and cluster potential, whereas the local density has a proximate effect on galaxies. However, both parameters still play a significant role in the properties of cluster galaxies, and we therefore investigate trends with each separately (see Li et al., 2012 for a detailed discussion on the two methods). While both measurements suffer from projection effects, the benefit of using local density is that it is straight-forward to correct each galaxy for spectroscopic completeness given its stellar mass and radius (Muzzin et al., 2012), which essentially provides us with a 100% complete sampling of density. We note that our radial measurement does not require a completeness correction as the completeness bias for mass is similar at all radii (see fig. 4 in Muzzin et al., 2012). To compute density, each galaxy is first given a weight based on its completeness. We then interpolate the distance to the 10th nearest neighbor for each source by summing the weighted values for galaxies above our mass limit of $2.0 \times 10^9\,\mathrm{M}_\odot$, and compute the density as $\Sigma = 10/(\pi d_{10}^2)$. The drawback of this method is that we lose information on smaller density scales.

Nevertheless, our two environment parameterizations convey the same trend: the average SSFR of star-forming galaxies (i.e., MIPS galaxies; green stars) is mostly independent of environment (see lower panels of Figure 3.4). A best-fit line to the average MIPS SSFR in radial and density bins reveals a slope consistent with zero at the level of 1.6σ (-0.29 ± 0.18) and 1.2σ (-0.23 ± 0.20), respectively. In Figure 3.4, we show the best fit to the normalization of the SSFR with the slope fixed at zero. Though seemingly surprising, this flat trend is consistent with other cluster surveys over many redshifts and using various star formation tracers, including UV studies at $0.16 < z < 0.36$ (Lu et al., 2012) and optical star formation indicators at $z \sim 1$ (Peng et al., 2010; Muzzin et al., 2012).

However, our MIPS sample is SFR-limited, and thus not complete in SSFR for any given mass except at the highest SSFR values, $\log(\mathrm{SSFR}) \gtrsim -9$. The flat trend in SSFR might be the result of skimming the high SSFR galaxies off the top of a deeper correlation. For example, if we assume that more massive galaxies reside at lower radii, probing deeper in SFR could preferentially bring down the average SSFR at low radii compared to outer radii, uncovering a non-flat SSFR trend. We check for this effect by assigning a 3σ upper limit for the SSFR of cluster members without a MIPS detection (black arrows in upper panels of Figure 3.4) and include these limits in the average SSFR (black circles in lower panels). The upper panels of Figure 3.4 reveal that there is no underlying mass segregation in the radial/density properties in the population not detected by MIPS (i.e., the limits are flat with environment), which suggests that a lower SSFR-limit would not necessarily result in a non-flat trend for star-forming galaxies galaxies. Moreover, the slope of the average SSFR assuming all cluster members have some star formation flattens out even further with density (-0.08 ± 0.10, dotted black line in lower right panel).

If we instead treat the galaxies without MIPS detections as quiescent (i.e., non-star forming) and investigate the integrated SFR (above our SFR-limit) per total unit stellar mass as a function of environment (cyan triangles), namely the total MIPS SFR divided by the total stellar mass of all cluster members in each bin, we find a decreasing SSFR with increasing (decreasing) density (radius). We note that both spectroscopic and MIPS members have the same target selection, so they have the same completeness rates as a function of mass and radius. The integrated SFR per total stellar mass is a proxy for the number of star forming galaxies compared to quiescent galaxies at each radius and reveals a lower fraction at denser environments. A fit to the integrated SSFR versus density yields a slope of -0.61 ± 0.19 (dashed cyan line), and is therefore inconsistent with zero at the $> 3\sigma$ level.

This depression of star formation in the cluster core is in accordance with local clusters (e.g., Kauffmann et al., 2004) and suggests that the SSFR-density relation is already established in the highest-density regions at $z \sim 0.9$. This is in contrast to $z \sim 1$ field studies that found a reversal in the SFR-density relation (Elbaz et al., 2007; Cooper et al., 2008), although they were limited to lower density environments. Instead, we compare our results to a similar IR study of a $z = 0.834$ cluster from Patel et al. (2009) who probe a wide-range of environments and utilize a $24\,\mu$m stacking analysis on all cluster members to determine SSFRs. They uncover a trend of decreasing SSFR with increasing density (open squares in the right panel of Figure 3.4), analogous to our total SSFR. This relation prevails even when controlling for stellar mass: the open, teal squares correspond to lower masses of $2.0 \times 10^{10} < \mathrm{M/M_{\odot}} < 6.3 \times 10^{10}$, and the open orange squares represent all galaxies with $\mathrm{M} > 6.3 \times 10^{10}\,\mathrm{M_{\odot}}$ in the Patel et al. (2009) sample. We note the normalization of our trend is higher, but we probe down to an order of magnitude lower in stellar mass ($2.0 \times 10^{9}\,\mathrm{M_{\odot}}$); as lower-mass systems typically display slightly higher SSFRs (see §3.4.4 below), a higher SSFR in our data is expected.

In Figure 3.4 we also plot the SSFR required for stellar mass to double (assuming a constant SFR) by $z = 0$ (dot-dashed horizontal line). We note that the integrated SSFR per total stellar mass (cyan triangles) is consistent with or below this limit in all environments, signifying that a majority of cluster members (including quiescent galaxies) have already experienced most of their mass growth. However, the average MIPS SSFR (and average SSFR for all members with limits) lie above this line: the star-forming galaxies have yet to undergo the bulk of their activity, assuming they can sustain their SFR. Perhaps we are witnessing the primal growth stage of these galaxies, before they have properly assimilated into the cluster and been exposed to any environmental quenching. Alternatively, if any of these galaxies have already experienced a suppression of their star formation, the quenching timescale must be rapid enough that any environmental trend with SSFR gets washed out: SSFRs are immediately terminated, precluding an intermediate phase. In other words, why is there a lack of variation in the star-forming population despite a changing fraction of star-forming galaxies with environment? We will return to this flat environmental trend in §3.5 and provide an alternative explanation.

3.4.4 The Correlation between Star Formation Rate and Stellar Mass

We can investigate whether any MIPS members deviate from their expected SFRs and SSFRs given the tight correlation of increasing SFR with stellar mass for star-forming galaxies, which retains only 0.2 dex scatter at $z \sim 1$. Recent studies have observed this star-forming main sequence in the field out to $z \sim 2$, which monotonically shifts to higher SFRs with increasing redshift (Noeske et al., 2007; Elbaz et al., 2007; Daddi et al., 2007). In Figure 3.5 we plot the main sequence trend in the field at various redshifts: $z = 0.1$ from the Sloan Digital Sky Survey (SDSS; Brinchmann et al., 2004) as analyzed by Elbaz et al. (2007); $z \sim 1$ from the Great Observatories Origins Deep Survey (GOODS; Elbaz et al., 2007); and $z \sim 2$ from GOODS (Daddi et al., 2007); we have converted each trend to Chabrier-IMF based masses and SFRs for consistency with our own sample. We also plot our $24\,\mu$m-derived SFRs for MIPS cluster members at $z \sim 0.9$ along with our field sample over $0.84 < z < 1.0$. Due to systematic differences in SFRs, stellar masses, and selection criteria (e.g. mass-limited versus luminosity-limited samples), we refrain from quantitative comparisons between our trend and the field samples from GOODS and SDSS. Our own field sample offers a more suitable comparison, and in fact, displays a similar trend as the larger GOODS sample at $z \sim 1$, albeit with slightly higher SFRs.

Immediately obvious in Figure 3.5 is the distinction between the old and young MIPS populations: the majority of massive, older members (filled red circles) lie

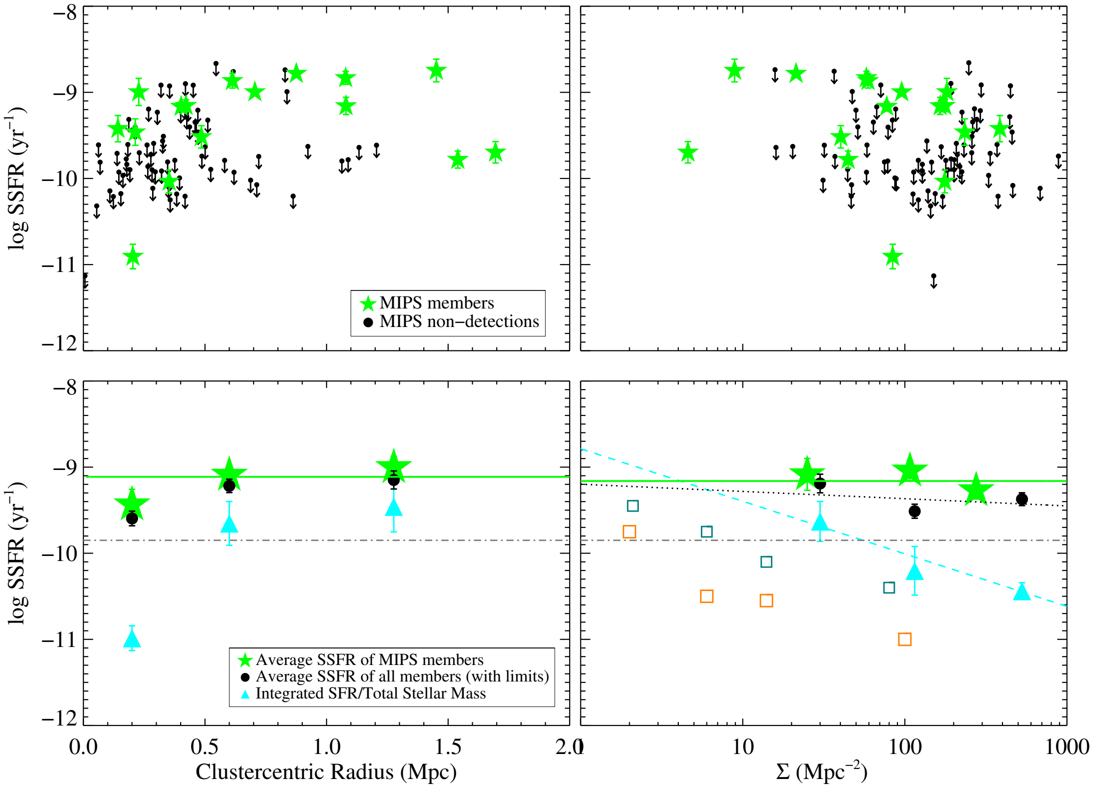

Figure 3.4 Upper panels—The individual SSFRs for all cluster members as a function of clustercentric radius (left panel) and density using the 10th nearest neighbor (right panel). The green stars correspond to MIPS cluster members, and the black circles with arrows are 3σ upper limits on the SSFR given the stellar mass for the cluster members without MIPS detections. Lower panels—The SSFR in bins of clustercentric radius (left) and density (right). The green stars correspond to the average SSFR of detected MIPS members in each bin, i.e., the SFR divided solely by the mass of MIPS members and averaged over the number of MIPS galaxies in each bin. Black circles represent the average SSFR for all cluster members, assuming a 3σ upper limit on the SSFR for undetected MIPS members. Cyan triangles denote the integrated SFR (above our SFR-limit) per total unit stellar mass: a sum of the total 24um-derived SFR divided by the total stellar mass of all spectroscopic members in each radial bin, which essentially probes the fraction of star-forming galaxies. The horizontal solid green line illustrates the best fit line to the green stars with the slope fixed to zero, i.e., the normalization of the average MIPS SSFR. The dot-dashed horizontal line corresponds to the required SSFR for the mass to double by $z = 0$. The two remaining lines in the lower right panel depict the best linear fits to the corresponding binned values with density. The open squares represent the stacked IR SSFRs from Patel et al. (2009) in a $z = 0.834$ cluster, where teal squares correspond to galaxies with masses of $2.0 \times 10^{10} < \mathrm{M}/\mathrm{M}_{\odot} < 6.3 \times 10^{10}$, and the grey squares represent all galaxies with $\mathrm{M} > 6.3 \times 10^{10}\,\mathrm{M}_{\odot}$.

well below the expected correlation, while the younger members (filled blue circles) tend to follow the main sequence trend observed in the $z \sim 1$ GOODS field (solid black line) and the GCLASS field (open squares). Moreover, this double-sequence in SFRs is unique to the cluster as there is only one field galaxy in our sample with a significantly low SFR for its stellar mass.

The double-branched distribution is similarly manifested in the SSFR, plotted in the lower panel of Figure 3.5. The least massive galaxies, which are inherently younger (see Figure 3.2), have the highest SSFRs, while more massive galaxies have substantially lower SSFRs. While this is consistent with the evolution of the mass function (e.g., Kodama et al., 2004) which shows that the massive end of the galaxy mass function in clusters is in place by $z \sim 1$ and the evolution between $z = 0 - 1$ consists of a build-up of the $< 10^{11}\mathrm{M}_\odot$ end, it could also be a completeness effect as we do not probe the region of low mass and low SSFR (Figure 3.5).

In hopes of identifying further differences, we split the $24\,\mu$m members into two cases based on their proximity to the expected SFR for their given mass at $z \sim 1$, as shown by the dot-dashed pink line in Figure 3.5. This line corresponds to log(SSFR)$=-9.3$. We designate the population above the line as the main sequence population, and those below the line as the sub-main sequence given they are in fact closer to the $z \sim 0$ field trend and lie in a substantially disparate space from the GCLASS $z \sim 1$ field sample.

In Figure 3.6 we stack the spectra in each population separately (nine and seven members in the main sequence and sub-main sequence groups, respectively) with an inverse weighting based on the spectroscopic completeness. Specifically, we investigate the equivalent widths of the [OII] doublet (3727 Å) and a Balmer absorption line, Hδ at 4100 Å (see Table 3.1); their relative strengths impart a timescale of star formation, with strong [OII] indicating current activity and Hδ representing more prolonged star formation. The striking contrast in the stacked spectra hints at differences in the star

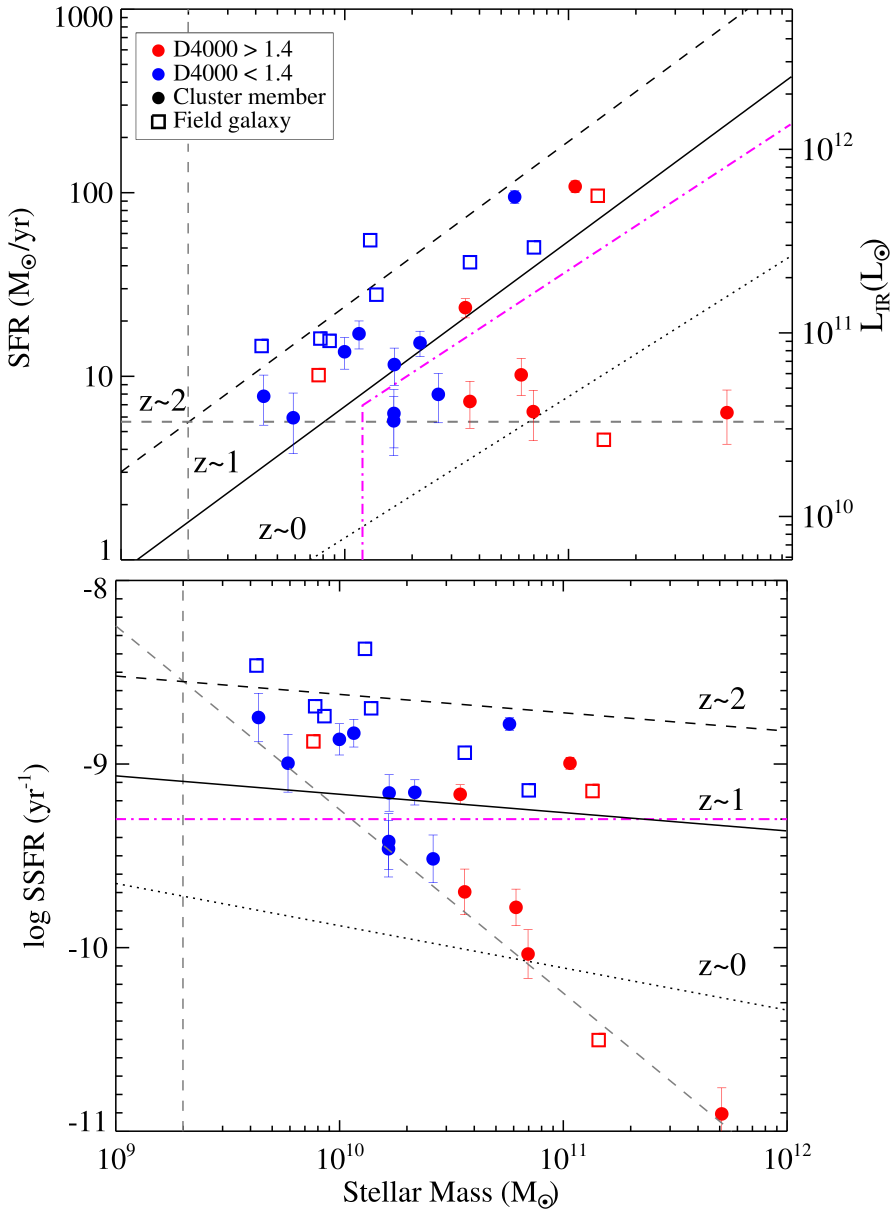

Figure 3.5 Top—SFR versus stellar mass for MIPS cluster galaxies, separated in colour by D4000. Open squares are the field population from $0.84 < z < 1.0$. The dotted, solid, and dashed black lines correspond to the field trends at $z = 0, 1, 2$, respectively (converted to a Chabrier IMF). The pink dot-dashed line denotes the boundary between the two populations of the cluster galaxies: main-sequence vs sub-main sequence, as defined by their star formation rate. The vertical and horizontal gray dashed lines indicate our mass completeness, $\mathrm{M} > 2.0 \times 10^9\ \mathrm{M}_\odot$, and SFR detection limit, respectively. Bottom—SSFR versus stellar mass. Symbols and lines are the same as the top panel.

Table 3.1 Spectroscopic measurements from the weighted, stacked spectra.

	Sub-main sequence	Main sequence
OII EW	5.4	22.0
Hδ EW	2.4	4.7
D4000	1.46	1.20

formation histories of these two populations. The main sequence group has moderate to strong [OII] emission, relatively deep Hδ absorption, and strong Balmer absorption features. Based on the spectral classifications of Dressler et al. (1999), these are most likely dust-obscured galaxies undergoing bursty star formation, e(a) galaxies. They also border on the classification of e(c) galaxies, which experience normal, continuous star formation. As these main sequence galaxies are coeval with $z \sim 1$ GCLASS field, and follow the expected SFR versus stellar mass trend, they have probably been recently accreted from the field, and therefore belong to the infall population.

On the other hand, the sub-main sequence population has weak [OII] emission and a strong 4000-Å break, marked by a sudden drop at [CaII] K and H and lines. The shallow Hδ absorption is also indicative of older systems: as massive stars die, the Hδ absorption fades. The lack of strong Balmer absorption precludes the possibility of poststarburst systems. The stacked spectrum for this population is more consistent with that of a passive galaxy with only a slight hint of star formation; it is classified as right on the border of an older k-type spectrum and e(c) galaxy, as there is some [OII] emission present. We list equivalent widths for [OII] and Hδ, along with D4000 in Table 3.1.

We also note the possibility that galaxies on the sub-main sequence could be AGNs, rather than simply star-forming galaxies with lower star formation activity. This would also be an interesting explanation as it could imply that the AGN is responsible for quenching the star formation through feedback. For example, Page et al. (2012) have claimed to find evidence for quasar-mode feedback in the form

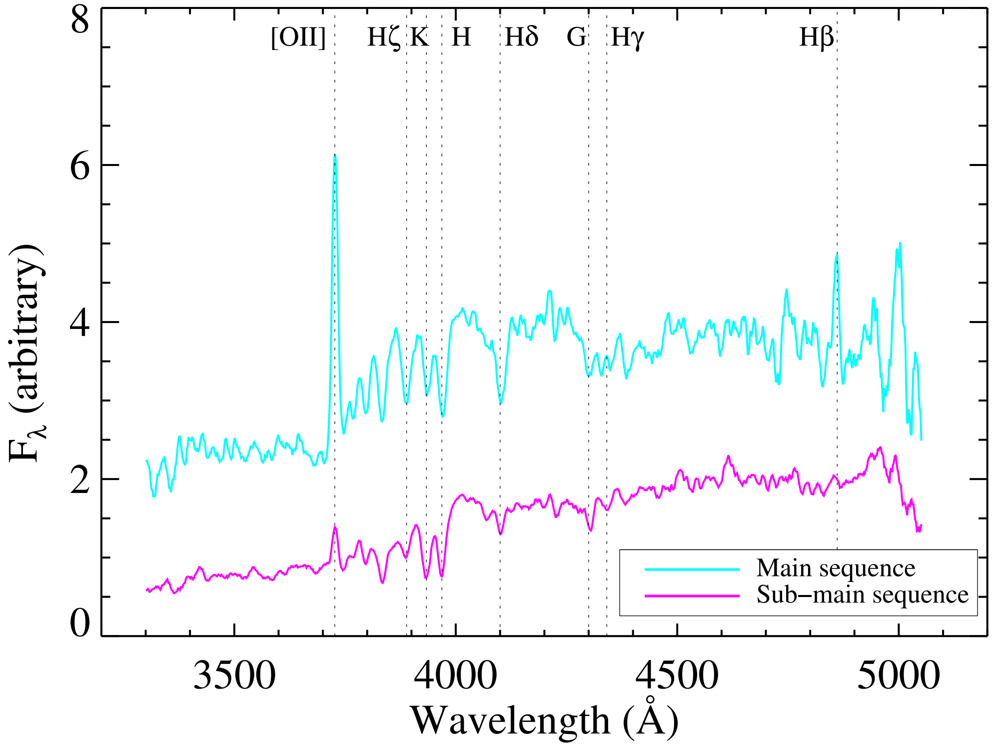

Figure 3.6 The resulting stacked spectra of MIPS cluster members from each population identified in §3.4.4: main sequence population (cyan spectrum) and sub-main sequence population (pink spectrum). Individual spectra are weighted by their spectroscopic completeness, as determined by their stellar mass and clustercentric radius.

of suppressed star formation rates for the most luminous AGNs at $z = 1 - 3$ (but see Harrison et al. (2012) for an alternative result). In this scenario, we could be witnessing the residual star formation in AGNs that are still actively accreting and just beginning to peak in luminosity.

3.5 DISCUSSION

We have analyzed a single $z = 0.872$ massive cluster from the GCLASS sample from an infrared perspective, investigating how dusty star-forming galaxies behave in the broader context of all spectroscopically-confirmed cluster members. We discuss our results here, and merge them with a detailed kinematic analysis of each MIPS member. This allows us to access the role of environment on star-forming galaxies utilizing their previous exposure to high densities, rather than their instantaneous environment.

The ages and stellar masses (Figure 3.2) of the MIPS members compared to both cluster and field galaxies suggests that they have been recently accreted from the field. The line-of-sight velocity distribution for MIPS members (Figure 3.3) exhibits analogous results, as they hug an outer envelope of velocities consistent with the younger cluster members and what would be expected from an infall population. MIPS cluster members have been observed to share certain properties with field galaxies in previous studies, but are not simply a parallel population in all cases. For example, Kocevski et al. (2011) determined that although MIPS sources have a spatial distribution within the cluster typical of an infalling population, their spectral properties reveal burstier episodes of star formation than their field counterparts at $z \sim 0.9$, perhaps provoked by harassment and mergers during assembly. While the stacked spectrum of our main-sequence galaxies is consistent with e(a) type galaxies—possibly indicative of bursty star formation—we do not see evidence for enhanced activity compared to the field. Moreover, we uncover an additional branch of 24 μm members that exhibit older, more quiescent spectral features, suggesting the existence of an environmental quenching mechanism that could occur following a possible (though not definite) initial triggering of star formation.

We find the SSFR of MIPS members to be independent of the projected local cluster environment: they maintain the same level of star formation at all densities and radii (Figure 3.4). Although this is consistent with previous studies (e.g., Peng et al., 2010; Lu et al., 2012; Muzzin et al., 2012), it is surprising given an observed increase in the fraction of star-forming galaxies with decreasing density over various star-formation indicators at $z \lesssim 1$, for example, [OII] emission lines (Poggianti et al., 2008; Muzzin et al., 2012); Hα luminosity (Sobral et al., 2011); and 24 μm flux (e.g., Finn et al., 2010 and the work presented here as shown by the cyan triangles in Figure 3.4). Many studies have invoked rapid quenching timescales to explain the disparate trends, such that star-forming galaxies are never observed in an intermediate stage—they are either active or completely quenched. However, when we investigate the SFRs and SSFRs as a function of stellar mass (Figure 3.5), we discover two distinct star-forming branches: one that is in line with the expected main sequence in the $z \sim 1$ field and undergoing obscured star formation, and another that displays depressed levels of star formation for a given mass and has a stacked spectrum consistent an older k-type galaxy. Moreover, these sub-main sequence galaxies are on average more massive; it is the less massive galaxies that are forming the bulk of the stars (though this could be a selection effect). This is consistent with a downsizing trend in mass assembly such that star formation shifts to less massive galaxies as the Universe ages (see also Kodama et al., 2004; Feulner et al., 2007; Sobral et al., 2011). Perhaps this sub-main sequence is a population of MIPS galaxies that have reached higher density regions or even the cluster core sometime in their past and have been exposed to some sort of environmental quenching; however, this seems inconsistent with the fact that no environmental dependence on SSFR is observed (Figure 3.4). Either quenching is ubiquitous throughout the cluster with little dependence on the environment or we are not measuring the environment properly. This raises the question: are we truly sampling MIPS members in the cluster core? We address this issue in the subsequent sections.

3.5.1 Velocity Distributions of Two Star-Forming Populations

In Figure 3.7 we re-analyze the line-of-sight velocities as a function of projected radius for the MIPS members, accounting for the double-sequence in SFRs. We highlight the

MIPS sources on the main sequence with cyan squares, and those populating the sub-main sequence with pink squares. There seems to be a rather clear distinction between the two populations, with the majority of sub-main sequence galaxies possessing lower velocities, while the main sequence galaxies avoid velocities below $1000\,\mathrm{km\,s^{-1}}$; with a few exceptions, the main sequence MIPS members adhere to an outer envelope in radial-velocity space. More importantly, at any given projected radius, we observe a mix of main sequence and sub-main sequence star-forming galaxies. If we return to the notion that the SSFR has no significant dependence on environment, this result offers a hint of an alternative interpretation: it indicates that low radial bins are contaminated by high-velocity galaxies, which could be infalling galaxies (outside the cluster core) that have fallen far enough into the gravitational potential well to attain large line-of-sight velocities (Haines et al., 2012). Some of these systems may in fact be at physically low radii, however, they could be on their initial (or even a subsequent) pass through the cluster and therefore are still distinct from a virialized core population that has spent a much greater amount of time in dense environments. As these systems have retained a nominal level of star formation for their stellar mass, they augment the average SSFR in low radial bins, or in what is referred to as the cluster core. The antithesis contamination occurs at large projected radii where the average SSFR is pulled down from low velocity interlopers—possibly galaxies at large physical radii that have already felt the effects of the cluster environment and therefore are not representative of an infalling population. In tandem, these two effects yield an overall flat SSFR with projected radii and densities.

We attempt to identify dynamically distinct populations in Figure 3.7 utilizing the results of Mahajan et al. (2011), where they use the dark matter hydrodynamical simulations from Borgani et al. (2004) to extract a sample of 93 mock clusters from simulations of 117 haloes, 105 of which have $\mathrm{M}_{200} > 1.4 \times 10^{14}\,\mathrm{M}_{\odot}$. From these clusters, they statistically quantify the fraction of virialized, backsplash, and infall galaxies at various projected radii and velocities. These classifications correspond to decreasing timescales of accretion, respectively: virialized galaxies were accreted when the cluster core was forming and are now passively evolving; backsplash galaxies have had time to pass through the cluster core and experience the first effects of the cluster environment, but have not yet amalgamated with the virialized population and therefore represent an intermediate phase of accretion (e.g., Balogh et al., 2000); infall galaxies were recently accreted from the field and have not reached pericenter in their orbit around the cluster. We plot the delineations in velocity-radius phase space in Figure 3.7; the corresponding fractions of each classification, along with the applications to our entire spectroscopic sample are summarized in the right-hand panel.

We assign each galaxy in our spectroscopic sample as virialized, infalling, or backsplash based on its age and, for the case of MIPS-detected members, its SFR. For cluster members that are not detected by MIPS, we simply assume that older members are virialized and younger galaxies have been recently accreted (i.e., infalling). For MIPS galaxies, we assume any galaxy on the main sequence belongs to the infalling population, while those on the sub-main sequence are virialized if they are older, or are part of the backsplash population if they are younger.

The consistency between the simulated fractions from Mahajan et al. (2011) and our cluster sample, using this simplistic criteria, is quite good. For example, the solid outlined box in Figure 3.7 represents galaxies within $0.5r_{200}$ and $1.0\sigma_v$, where 89%, 8%, and 3% of galaxies are expected to belong to the virialized, infall, and backsplash populations, respectively; we have 52 cluster members within this area, therefore the predicted fractions correspond to 46.3 virialized, 4.2 infalling, and 1.6 backsplash members in our sample (the second column in the right panel displays the expected number within our sample in each box). Of the seven MIPS-detected galaxies within this region, three fall on the star-forming main sequence (cyan squares),

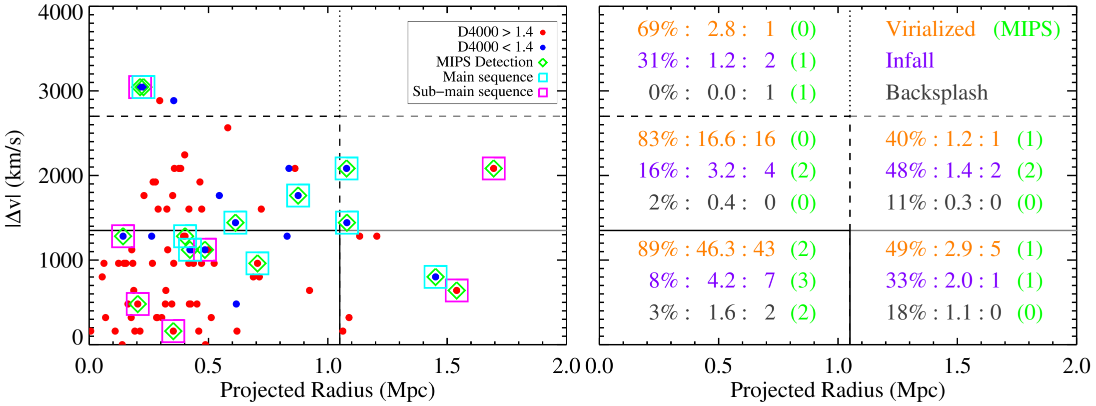

Figure 3.7 Left—The absolute line-of-sight velocity as a function of projected radius. MIPS members belonging to the main (sub-main) sequence of SFR are highlighted with cyan (pink) squares. The horizontal lines correspond to σ_v and $2\sigma_v$, and the vertical line represents $0.5r_{200}$. The boxed areas correspond to the divisions in Mahajan et al. (2011) and are identical in both panels. Right—The first number on the left in each rectangle corresponds to the fraction of galaxies classified as virialized (orange), infall (purple), and backsplash (gray) in projected phase space bins from dark matter simulations in Mahajan et al. (2011). We then apply the fractions to the total number of spectroscopically confirmed cluster members in each bin and list it after the colon. The third number represents the actual number of each type of galaxy within that phase space based on its age and SFR (for MIPS-detected members). We assume a simple classification in which: virialized galaxies consist of non-star forming older galaxies (red circles) and MIPS-detected older galaxies on the sub-main sequence (red circles with pink squares); infalling galaxies include non-star forming younger galaxies (blue circles) and MIPS-detected galaxies on the main sequence, both young (blue circles with cyan squares) and old (red circles with cyan squares); and backsplash galaxies comprise younger MIPS-detected galaxies on the sub-main sequence (blue circles with pink squares). The last column in each bin (green number in parentheses) represents the number of MIPS sources of that galaxy type that are included in the actual number counts based on the classification scheme stated above.

which suggests they are recently accreted members that have retained their gas and star formation—this number is just below the expected number of infalling galaxies from the simulations (4.2), and increases to seven after we include the members not detected by MIPS. The remaining MIPS members in this region lie on the sub-main sequence (pink squares), and therefore display lower SFRs. Additionally, there is a clear divide in the age of these four galaxies, with two containing shallow 4000 Å breaks (filled blue circles). The depressed SFRs of these two galaxies, along with their younger stellar populations, suggest they are backsplash galaxies which were stripped of their gas reservoir as they passed through the cluster core, but have not had enough time to completely virialize; this is also consistent with the expected backsplash fraction (two galaxies in total). The last two MIPS members (pink squares surrounding red circles) are both older and have suppressed SFRs, suggestive of passive, virialized galaxies which statistically comprise the bulk of this region. Including the galaxies without MIPS detections that have older ages, our classification scheme yields 43 virialized galaxies in this region, which is consistent with the number from the simulations (46.3). We note there is (seemingly) one MIPS outlier at both large projected radius and velocity that has a low SFR and an older stellar population. However, this region is still expected to contain 40% virialized galaxies, so it is not unfeasible for less active systems to inhabit this phase space.

We check the robustness of our classifications with respect to the depth of the MIPS data by assuming the SFR-limit is a factor of two lower ($3\,\mathrm{M}_{\odot}\,\mathrm{yr}^{-1}$), and all galaxies currently not detected by MIPS have this SFR. We then simplistically assign them to the above classifications based on their stellar mass and which star-forming sequence they populate. We find that two infalling galaxies would switch to a backsplash classification and three virialized galaxies would be infalling; therefore, there is no significant change in the numbers assuming a deeper SFR-limit.

3.5.2 Utilizing Caustic Diagrams as Accretion History Predictors

The mixing of different dynamical histories at all projected radii casts a doubt on the interpretation that environment has no effect on the SSFR of star-forming galaxies. However, our attempt to classify each galaxy as infalling or belonging to the cluster core is circumstantial.

A complementary method to kinematically differentiate between galaxies arises with the use of caustic profiles (i.e., constant velocity-radial lines) in physical radial phase space, where infalling and virialized cluster galaxies become distinct (e.g., Mamon et al., 2004; Gill et al., 2005; Mahajan et al., 2011; Haines et al., 2012). Moreover, this is inherently linked to the epoch of accretion, which illustrates the importance of a dynamically-defined environment: the time-averaged density a galaxy has been subjected to is more significant than its immediate surroundings.

Recently, Haines et al. (2012), stacked 30 clusters in the Millennium Simulation at $z = 0.21$ and investigated the relation between projected measurables and the accretion history of the cluster (see fig. 3 in Haines et al., 2012). Galaxies that were accreted when the cluster was first forming have a large dynamic range of velocities at the smallest projected radii, but only occupy a narrow silver of velocities ($\Delta v/v_\sigma \simeq 0$) over larger projected radii. Conversely, recently accreted galaxies permeate all projected velocities and radii, but are primarily concentrated along and outside a caustic line. These trumpet-shaped caustic profiles roughly correspond to lines of constant $r \times v$ in projected phase space. Recently accreted galaxies are therefore the dominant contaminant compared to galaxies that were accreted earlier, specifically in low radial bins. Moreover, star forming studies are biased towards picking out these contaminants, assuming recently accreted galaxies have managed to retain their activity and are classified as star-forming. This could explain why SSFR trends utilizing the entire galaxy population (quiescent and star-forming) or stacked SSFRs preserve a correlation with environment (e.g., Patel et al., 2011), while those solely for star-forming galaxies flatten out.

Motivated by the possibility of identifying distinct accretion histories within our own sample via caustic profile diagnostics, in Figure 3.8 we plot the strength of the 4000-Å break as a function of $(r/r_{200}) \times (\Delta v/\sigma_v)$, since constant values of this parameter correspond to caustic profiles which trace out accretion epochs. There is a clear movement towards higher values of $(r/r_{200}) \times (\Delta v/\sigma_v)$ for shallower breaks, meaning lower values on the x-axis correspond to older galaxies that were accreted at earlier times. We calculate a linear Pearson correlation coefficient of -0.41 between the parameters, with a high significance of $> 99.99\%$. To ensure this trend is not driven purely by the correlation between D4000 and stellar mass, we have separated the cluster members into two mass bins, above and below $3 \times 10^{10}\ \mathrm{M}_\odot$, which is roughly the median mass of the sample. The relation persists for both mass bins, meaning that for cluster galaxies of the same stellar mass, there is a progression towards larger $(r/r_{200}) \times (\Delta v/\sigma_v)$ values with decreasing time since the last burst of star formation. Assuming higher values of $(r/r_{200}) \times (\Delta v/\sigma_v)$ trace galaxies that were more recently accreted (which is analogous to fig. 3 in Haines et al., 2012), the trend in Figure 3.8 indicates the cluster environment has an effect on its constituent galaxies.

In order to isolate contamination in low projected radial bins from infalling/backsplash interlopers, we divide the space into three distinct regions based on the location of main and sub-main sequence galaxies. Combining the results of Haines et al. (2012) and Mahajan et al. (2011), these regions should primarily correspond to: virialized galaxies that were accreted when the cluster core was forming; a mix of all types but where backsplash galaxies are most likely to exist; and infalling galaxies that were recently accreted—at low, intermediate, and high values of $(r/r_{200}) \times (\Delta v/\sigma_v)$, respectively. We calculate the median D4000 in each region for both mass bins (filled stars), which confirms the declining age (i.e., epoch of accretion) with $(r/r_{200}) \times (\Delta v/\sigma_v)$.

We demonstrate the utility of these caustic regions in reference to our own sample

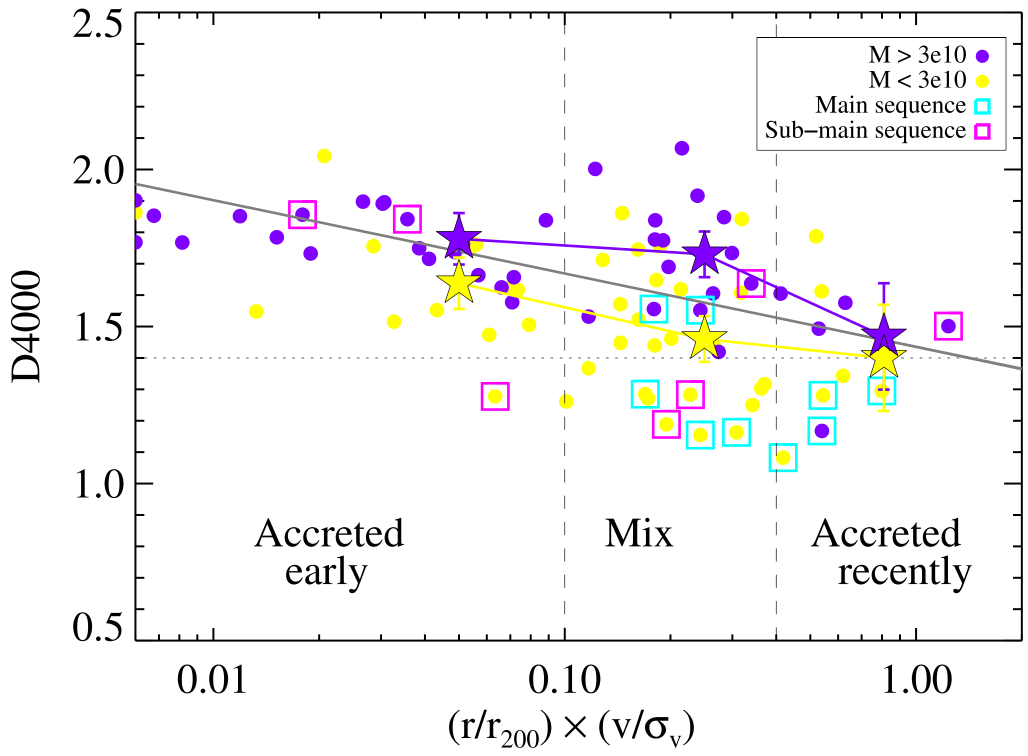

Figure 3.8 The strength of the 4000-Å break versus $(r/r_{200}) \times (\Delta v/\sigma_v)$ for all cluster members, divided in two mass bins. The MIPS members on the main and sub-main sequence are highlighted with cyan and pink squares, respectively. The solid gray line shows the best fit line for all galaxies. The median D4000 values for both mass bins in each region (denoted by the vertical dashed lines) are plotted as filled stars and indicate a declining accretionary sequence with $(r/r_{200}) \times (\Delta v/\sigma_v)$. The error bars are taken from the standard deviation on the bootstrapped median in each bin. We have labeled the regions based on accretion times. We note the three galaxies with the lowest caustic values are artificially plotted at $(r/r_{200}) \times (\Delta v/\sigma_v) = 0.006$ to reduce the size of the plot, but in fact have even lower values.

in Figure 3.9. We plot lines of constant $r \times v$ at 0.1 and 0.4 $(r_{200} \times \sigma_v)$, based on the regions in Figure 3.8. The innermost caustic line seems to preferentially select the older (virialized) population of cluster members that were most likely accreted at early times, including three out of the seven MIPS sources belonging to the sub-main sequence branch. Although rare, it is not inconceivable that recent star formation has occurred within the virialized population; (Mahajan et al., 2011) estimate that 11% of the virialized population are galaxies with ongoing or recent efficient star formation that could be attributable to rapid flybys. However, we note that their level of star formation is certainly suppressed compared to the main sequence.

Between the two caustic profiles, we expect a distribution of galaxies that were accreted early, recently, and somewhere in-between. Indeed, in this intermediate region of $0.1 < r/r_{200} \times v/\sigma_v < 0.4$, there exists a mix of old, main sequence galaxies and young, sub-main sequence galaxies, which could result from a backsplash population. The significance of the backsplash population has been demonstrated before in various simulations. Balogh et al. (2000) found that over half of the galaxies within 1–$2r_{200}$ have been inside the virial radius at an earlier time and rebounded outward. Moreover, 90% of these backsplash galaxies have plunged deep into the potential well, within the inner 50% of the virial radius (Gill et al., 2005).

The region exterior to the 0.4 ($r_{200} \times \sigma_v$) caustic profile should preferentially pick out galaxies that have been recently accreted (Haines et al., 2012). Based on the fractions from Mahajan et al. (2011), it should additionally favor infalling over backsplash galaxies. Moreover, Gill et al. (2005) observed that basksplash galaxies are kinematically distinct from infalling galaxies, as the latter have much higher relative velocities. Although this velocity bimodality can get slightly washed out in projected space, there still exists an average trend toward lower velocities for backsplash galaxies. Notably, this region contains the majority of young main sequence galaxies, which are most consistent with an infall population given their age and SFRs. As stated in §3.5.1, the lone sub-main sequence galaxy in this region could statistically be a virialized galaxy outside the core; however, we also note that we expect one chance alignment between MIPS sources and spectroscopic members (§3.3.1), which could be manifested here. Alternatively, this galaxy and another old, sub-main sequence galaxy at high projected radius could both belong to groups that have been accreted into the cluster. In this scenario, the lower SFRs of these galaxies could be due to pre-processing (e.g., Zabludoff and Mulchaey, 1998) in the group environment prior to accretion. McGee et al. (2009) found that the accretion of galaxy groups onto a massive $z \sim 1$ cluster accounts for a significant proportion ($\gtrsim$30%) of the galaxy population, and moreover, galaxies that derive from group environments are more massive. Indeed, the two outliers are both more massive than the majority of main sequence galaxies and exhibit suppressed SFRs. However, the sparse spectroscopy at these high radii precludes us from reliably identifying infalling groups.

3.5.3 A Kinematic Approach to the Environmental Dependence on the Specific Star Formation Rate

In hopes of disentangling radial contamination from environment, we consider the SSFR as a function of $r \times v$, normalized by the cluster velocity dispersion and r_{200}, in Figure 3.10. As shown in Figures 3.8, 3.9, and fig. 3 from Haines et al. (2012), low values of $r \times v$, $< 0.1(r_{200} \times \sigma_v)$, should represent a more dynamically-isolated cluster core, as it is dominated by galaxies accreted at early times, which have spent more time in dense cluster regions. Similarly, galaxies recently accreted possess higher caustic values of $> 0.4(r_{200} \times \sigma_v)$, as they are more likely to have high projected radii and velocities. In Figure 3.10 there is a clear segregation between the two star forming populations when using a caustic approach to define environment. The sub-main sequence galaxies (pink squares) are preferentially at low values of $r \times v$ and well contained within 0.4 $(r_{200} \times \sigma_v)$ with the exception of one galaxy; the main-sequence branch (cyan squares), however, does not penetrate below a value of 0.1 $(r_{200} \times \sigma_v)$, but rather is dispersed throughout intermediate and high values. The isolation of the galaxies on the sub-main sequence yields a prominent depression in SSFR towards the "caustic core" of the cluster, namely, with galaxies that exhibit

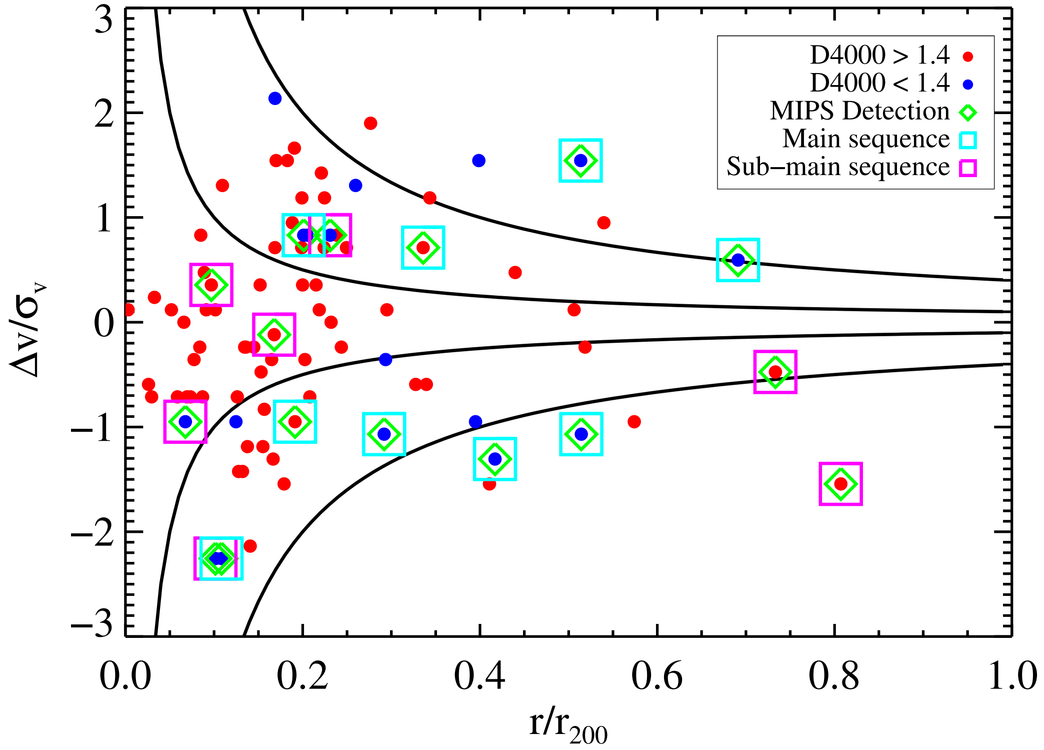

Figure 3.9 A caustic diagram for all spectroscopically confirmed cluster members. The symbols are the same as in Figure 3.7. We plot caustic profiles—lines of constant $(r/r_{200}) \times (\Delta v/\sigma_v)$—at 0.1 and 0.4 to isolate virialized (within the inner caustic), backsplash (between caustics), and infall galaxies (along and outside the outer caustic).

both low projected radii and low line-of-sight velocities. Splitting the galaxies into the aforementioned $r \times v$ bins (shown by vertical lines in Figure 3.10) and calculating the average SSFR of the MIPS cluster members in each bin (green stars) reveals a 0.9 dex decline between the highest and lowest caustic bins. With this definition for environment, the cluster core is more of a signpost for the dynamic history of its constituents, as the time-averaged density of a galaxy should increase with its time since accretion. If this dynamic core more accurately represents the virialized cluster core than clustercentric radius or density probes, the interpretation that the SSFR of star-forming galaxies lacks a dependence with environment warrants caution. Moreover, a rapid quenching timescale would no longer be a necessary requirement; if younger star-forming galaxies on the sub-main sequence are backsplash galaxies, we can use the dynamical timescale to place a lower limit of ∼1.3 Gyr on the duration of quenching.

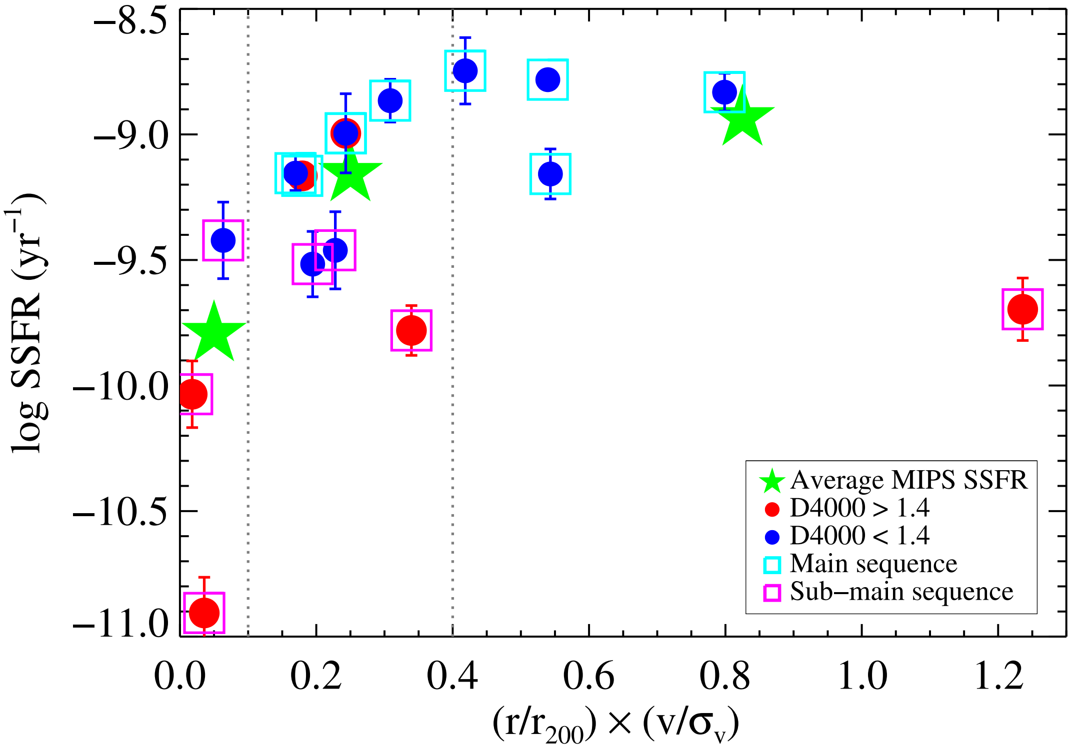

Figure 3.10 The SSFR for star-forming galaxies as a function of caustic environment, $(r/r_{200}) \times (\Delta v/\sigma_v)$. The sub-main sequence galaxies (pink squares) primarily inhabit low values of $(r/r_{200}) \times (\Delta v/\sigma_v)$ compare to the main-sequence galaxies. In contrast to Figure 3.4, there is now a clear depression (0.9 dex) of the average SSFR (green stars) towards low caustic values, where we expect to isolate galaxies accreted at earlier times. The gray vertical lines indicate the limits of the bins.

3.6 CONCLUSIONS

We have presented an infrared study of SpARCS J161314+564930, a $z = 0.872$ massive galaxy cluster comprising 85 mass-limited, spectroscopically confirmed members, 16 of which have been detected at $24\,\mu$m. After combining the stellar ages, SFRs/SSFRs, and kinematics of dusty star forming galaxies, a clean narrative of the history of these cluster members begins to unfold. We summarize the main properties and trends of the MIPS galaxies as follows:

1. MIPS cluster members form a young envelope of the cluster population; they span the same range of stellar masses and D4000 values as coeval field galaxies, suggesting they primarily belong to a recently accreted population.

2. There is a bimodal or flat distribution of velocities for the MIPS members, peaking at $\pm 1000\,\mathrm{km\,s^{-1}}$, which is roughly the cluster velocity dispersion. This sharply deviates from the older cluster members, which form the expected Gaussian distribution of velocities. There is only a 6% probability that these two distributions derive from the same parent population; therefore, the MIPS sources seem to represent a recently accreted, un-virialized population.

3. When local environment is defined as projected clustercentric radius or density, it appears to have no effect on the average SSFR of star-forming galaxies (but see conclusions 5–8 for an alternative explanation). However, when accounting for the total mass from all cluster members, there is a sharp decline in the total SSFR towards low radii, indicating that the SFR-density relation is already established in the densest regions at $z \sim 0.9$.

4. There exist two branches of SFR/SSFR as a function of stellar mass—one that is consistent with the star-forming main sequence of increasing SFR with mass, while the other displays a flat trend with suppressed SFRs compared to the

$z \sim 0.9$ field. This double-sequenced distribution appears to be unique to the cluster. Stacking the spectra of galaxies along each branch separately supports this by revealing distinct star formation histories: the former are likely obscured galaxies experiencing either continuous or bursty star formation, while the latter lacks Balmer absorption, has a strong 4000-Å break, and weak [OII] emission—features that are more typical of passive or quiescent galaxies.

5. Utilizing the results from Haines et al. (2012), we show that recently accreted galaxies contaminate all projected radii, while the earliest accreted galaxies are primarily at low radii, with only a little spillover at larger radii. Assuming star forming galaxies are preferentially an infalling or recently accreted population, the star forming population is therefore inherently more likely to be a contaminant in projected environment, which could contribute to the flat trend between the SSFR of star-forming galaxies with environment. Therefore, low radial bins are contaminated by recently accreted MIPS sources that have not yet (necessarily) passed through the densest regions of the cluster or core and could augment the SSFR.

6. A caustic diagram of line-of-sight velocity versus projected radius reveals that there is a mix of galaxies from each of the two star-forming sequences at any given radius. We are able to successfully isolate galaxies that were accreted at early times from recently accreted objects via caustic values of $(r/r_{200}) \times (\Delta v/\sigma_v) < 0.1$ and > 0.4, respectively. Intermediate values contain a mix of accretion histories, and should also contain the statistical majority of backsplash galaxies.

7. Applying caustic profiles of constant $(r/r_{200}) \times (\Delta v/\sigma_v)$ to our sample allows us to kinematically classify MIPS galaxies as virialized, backsplash, or infalling based on their age and SFR. Galaxies with lower star formation rates (i.e., on

the sub-main sequence) appear to belong to either the virialized or backsplash populations. Further differentiation between these populations arises from stellar age, as measured through the depth of the 4000-Å break. Although not definitively, older galaxies with D4000 > 1.4, are likely to be virialized within the 0.1 $(r_{200} \times \sigma_v)$ caustic profile. Backsplash galaxies appear to lie in intermediate regions of $0.1 < r/r_{200} \times v/\sigma_v < 0.4$. Infalling galaxies primarily occupy the region outside the 0.4 $(r_{200} \times \sigma_v)$ caustic profile and have SFRs consistent with the main sequence.

8. Using a caustic definition for environment reveals almost an order of magnitude (0.9 dex) depression of SSFR at low $(r/r_{200}) \times (\Delta v/\sigma_v)$ values, in contrast to the flat correlation observed with projected radius or density. This suggests that environment may suppress star formation as galaxies fall deeper into the cluster potential, with a minimum quenching timescale given by the infall time.

We stress that this is a case study of a single galaxy cluster, and a larger sample is needed to statistically verify our conclusions. We plan to expand our study to the entire GCLASS sample, which consists of ten clusters over $0.87 < z < 1.35$ and over 400 confirmed members. With a significant sample of dusty star-forming galaxies we can better assess the diagnostic power of caustic profiles in relation to environment, stellar ages, star formation, and quenching mechanisms.

4

A VIEW OF $z \sim 1.2$ CLUSTERS FROM *Herschel*

In this chapter we further develop the utility of an accretion-based definition for environment, isolating cluster populations within the phase space of radius and velocity. We extend the analysis to three $z \sim 1.2$ clusters from the SpARCS-GCLASS survey, consisting of a stellar-mass limited sample of 123 spectroscopically-confirmed cluster members above $2 \times 10^9\,\mathrm{M}_\odot$, including 58 star-forming galaxies with [OII] emission. Using *Herschel* observations from 100–500 μm, we stack PACS and SPIRE maps at the locations of star-forming cluster members, separated by phase-space bins, to determine trends as a function of environment. We confirm the result from Chapter 3, finding a similar depression of specific star formation rate from infalling to virialized galaxies. Exploiting the ample coverage of the far-infrared peak of the spectral energy distribution from *Herschel*, we extend the phase-space analysis to uncover a correlation between average dust temperature and environment. Galaxies within the middle phase-space bin, where the statistical majority of backsplash galaxies should exist, display a colder dust temperature on average. We examine the infrared colours of the three populations (low, intermediate, and high values of $r \times v$) to elucidate which quenching mechanisms could drive low dust temperatures for the intermediate galaxies. Both strangulation and ram-pressure stripping operating separately on different galaxy populations provide a plausible interpretation, with the latter likely affecting galaxies in the middle phase-space bin.

4.1 Introduction

The importance of local environment and stellar mass as drivers for galaxy evolution is now well established, as evidenced by their strong correlation with galaxy properties, such as star formation rate (SFR), colour and morphology. In particular, high-density environments of galaxy clusters in the nearby Universe are dominated by massive, passively evolving early-type galaxies, while isolated field galaxies host the most active star formation. This is called the star formation rate-density relation (e.g., Ellingson et al., 2001).

According to the hierarchical structure formation scenario, clusters gradually assemble their mass through accretion and merging events; therefore, higher-redshift clusters display significant differences from their local counterparts, manifested as an evolution in galaxy properties with time. Recent studies have suggested that by $z \sim 1$ the dominant sites of star formation are beginning to migrate to higher density regions (Elbaz et al., 2007; Cooper et al., 2008), though still avoiding the dense cores of clusters (Muzzin et al., 2012), back to at least $z \sim 1.6$ (Tran et al., 2010). Moreover, environment seems to play a prominent role in the timescale of star formation, with an especially marked difference between cluster and field galaxies at $z \sim 1.2$, as cluster early-type galaxies approach an epoch at which they are more rapidly assembling their mass than the coeval field population (Rettura et al., 2010, 2011). However, the precise mechanisms driving structural evolution and stellar mass assembly at $z > 1$ are still unclear.

Thus, the $z = 1 - -3$ regime is a crucial epoch for understanding the role of the environment in galaxy evolution, as it represents the global peak in the integrated star formation of the Universe (e.g. Madau et al., 1996; Lilly et al., 1996), and a pivotal point in the star formation rate-density relation. However, a comprehensive analysis of this parameter space was previously hindered by two fundamental limitations: uniform $z > 1$ cluster samples and accurate constraints on star formation.

Until recently, there were few clusters confirmed beyond $z \sim 1$; uniform cluster samples, accompanied by extensive multi-wavelength imaging and spectroscopy, are essential in order to identify cluster members and control for galaxy mass bias. Moreover, a caustic definition of environment that chronicles time-averaged density rather than instantaneous environment (as described in Chaper 3) relies on accurate cluster velocity dispersions and spectroscopically-confirmed cluster members with small uncertainties on the redshift.

Furthermore, deep infrared/submillimetre data are necessary for complete coverage of the thermal portion of the spectral energy distribution, which does not suffer from extinction as do data at optical/ultra-violet wavelengths. This allows for robust estimates of the total star formation activity in high-redshift clusters. In the past, 24 μm imaging with *Spitzer* provided a first glimpse of dust-enshrouded starburst activity at $z \sim 1$. However, it requires extensive extrapolation to the total infrared luminosity since it probes hot dust emission at $\lambda_0 \sim 12\ \mu$m, which is plagued by silicate absorption and polycyclic aromatic hydrocarbon (PAH) lines, and is far removed from the peak of the emission. The bands available with *Herschel*, on the other hand, straddle the peak of the $z \sim 1$ spectral energy distribution, and therefore provide a more reliable measurement of the total IR luminosity and cold dust emission.

To this end, we observed three spectroscopically-confirmed $z \sim 1.2$ clusters from SpARCS with *Herschel*. In this chapter, we present the first results from this study, which is a natural extension of the work in Chapter 3 but considers a more statistically significant sample and performs improved characterization of the thermal spectral energy distributions. We adopt the same bins for phase-space as in Chapter 3—$(r/r_{200}) \times (\Delta v/\sigma_v) < 0.1$; $0.1 < (r/r_{200}) \times (\Delta v/\sigma_v) < 0.4$; and $(r/r_{200}) \times (\Delta v/\sigma_v) > 0.4$—and refer to them as low, middle, and high, respectively. These delineations correspond to times of early, intermediate, and recent accretion onto the cluster, roughly representing where the majority of virialized, backsplash, and infalling galaxies exist,

Table 4.1 The *Herschel*-GCLASS sample at $z \sim 1.2$.

SpARCS Name	Nickname	z_{spec}	RA (J2000)	Dec (J2000)	M_{200} ($10^{14} M_{\odot}$)	R_{200} (Mpc)	σ_v (km s^{-1})	# of CMs
J161641+554513	EN1-349	1.1555	16 16 41.232	+55 45 25.708	$2.1^{+0.8}_{-0.9}$	$0.68^{+0.08}_{-0.12}$	660^{+80}_{-120}	43
J163435+402151	EN2-111	1.1770	16 34 35.402	+40 21 51.588	$4.0^{+1.4}_{-1.3}$	$0.98^{+0.10}_{-0.11}$	770^{+80}_{-90}	43
J163852+403843	EN2-119	1.1958	16 38 51.625	+40 38 42.893	$1.2^{+0.5}_{-0.6}$	$0.64^{+0.08}_{-0.14}$	510^{+60}_{-110}	37

respectively. We note that the backsplash galaxies are not necessarily the dominant population within the middle bin, they are just more likely to exist there. We therefore refrain from describing this population as backsplash galaxies, and instead use the term "intermediate" throughout this chapter. In Section 4.2 we describe the sample and the *Herschel* observations. We discuss our stacking analysis in Section 4.3, and the subsequent derivation of infrared luminosities. Our first results based on the stacked spectral energy distributions are given in Section 4.4, with final remarks in Section 4.5.

4.2 OBSERVATIONS AND DATA REDUCTION

4.2.1 A $z \sim 1.2$ Sample from GCLASS

The three clusters derive from the GCLASS cluster sample (described in Chapter 2; Muzzin et al., 2012) and therefore represent a stellar mass-limited sample, complete above 2×10^9 $M_{\odot}$. Cluster members are defined as sources within 1500 $\mathrm{km\,s^{-1}}$ of the cluster velocity dispersion, yielding a final sample of 123 cluster members with secure redshifts. Cluster properties, including M_{200}, R_{200}, and σ_v (G. Wilson et al., in preparation) are listed in Table 4.1.

4.2.2 *Herschel*-PACS Imaging

We observed with the Photodetector Array Camera and Spectrometer (PACS) instrument (Poglitsch et al., 2010) aboard *Herschel* over 5×5 arcmin around each cluster using the medium speed scan (20 arcsec/s) in array mode with homogenous coverage. We divided each cluster into two astronomical observation requests (AORs) with alternating scan directions of 45° and 135° to further maximize homogeneity (OBSIDs 1342247340, 1342247341 for EN1-349; 1342248661, 1342248662 for EN2-111; and 1342248631, 1342248632 for EN2-119). The final maps consist of 7.2 hours of integration over each field at 100 and 160 μm.

We reduce each observation (AOR) using the standard pipeline for deep scan maps in the HIPE v11.0 environment (Ott, 2010), with slight modifications to improve detectability of faint sources. First, the raw data (Level 0 products) are removed of any known bad and saturated pixels, and calibrated for instrumental effects, at which stage they are referred to as Level 0.5 frames. Next, from the timeline noise streams, glitches from cosmic rays hitting the bolometers are identified in the temporal domain and removed; the frames are then flat-fielded and the signal is converted from volts into janskys per pixel, producing Level 1 products. Up to this stage, the automatic pipeline can be run without modification.

The next reduction step utilizes a high-pass filtering technique to remove $1/f$ noise. This ubiquitous noise has large amplitudes at low temporal frequencies which produces long-timescale drifts in the detector timestreams. As this noise is highly correlated, it can be difficult to separate it from real astronomical signals, and cannot be treated independently from pixel-to-pixel (unlike white noise). The noise is removed in each timeline by subtracting a running box median of a specified width around each readout. Unfortunately, this method is problematic in that it can also remove real signal from the timeline; when a point source is present in the timeline, the median can be overestimated, leading to a flux loss for point sources in the final map. A detailed study by Popesso et al. (2012) found that masking sources in the timeline from a prior catalog alleviates most of flux loss, while any residual loss can be systematically calibrated. We therefore apply this technique to the Level 1 products, using a mask catalog from our deep MIPS catalogs for each field. We adopt circular mask values of 4 and 6 arcsec for 100 and 160 μm, respectively. The choice of the high-pass filter radius also has important consequences for the final map. While a smaller radius provides a better representation of the median, it can severely damage the point spread function. Alternatively, a large radius will not properly remove the $1/f$ noise. We therefore choose a radius of 15 readouts (corresponding to 30 arcsec) for the 100 μm channel and 20 readouts (40 arcsec) for the 160 μm channel. These high-pass filter and masking radii have both been tested by Popesso et al. (2012), and therefore the remaining flux loss in the final maps can be calibrated with a multiplicative factor that varies with aperture radii.

The final step in the reduction process is the projection onto the map, which utilizes the drizzle method (Fruchter and Hook, 2002). This method maps the input pixels onto a finer output grid, while shrinking the pixels (called the drop size) before they are averaged. We specify a drop size of 1/10 the input pixel size, which was found to be small enough to help reduce cross-correlated noise, but still large enough to avoid degrading the projected map. We perform the projection, weighting each input pixel contribution by the variance in each bolometer readout with width ten times the high-pass filter radius, and setting a specific world coordinate system (given by the Level 2 maps in the automatic pipeline). Finally, we co-add the maps from each scan direction. Our final images have output pixel sizes of 1 and 2 arcsec for 100 and 160 μm, respectively. In Figure 4.1, we show the maps for each cluster field in both channels, over-plotted with symbols denoting the positions of spectroscopically confirmed cluster members.

4.2.3 *Herschel*-SPIRE Data

We download raw archival data from the Herschel Science Archive for the Spectral and Photometric Imaging Receiver (SPIRE) for the Elais-North 1 and Elais-North 2 fields,

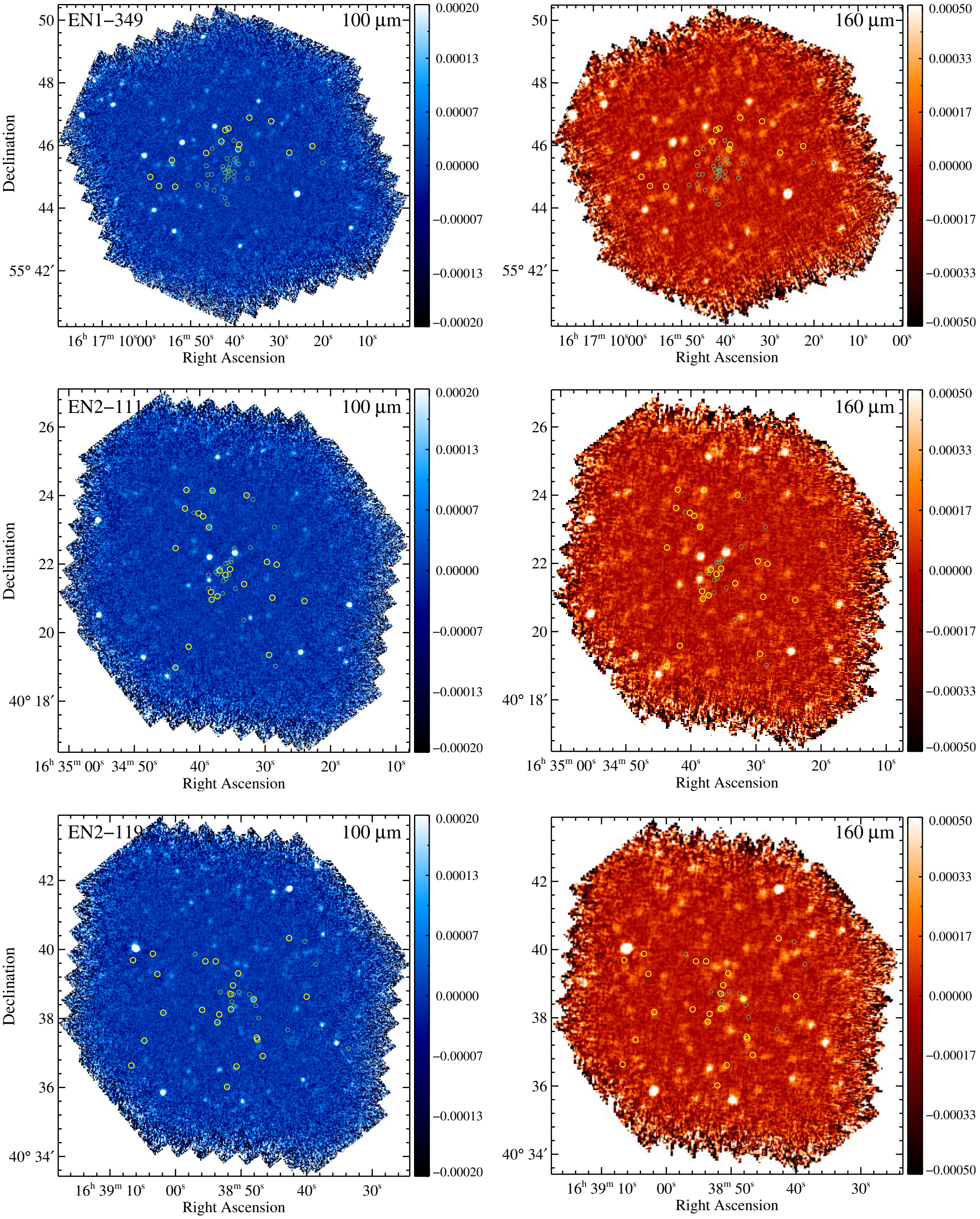

Figure 4.1 *Herschel*-PACS maps at 100 (left column) and 160 μm (right column) for EN1-349 (top row), EN2-111 (middle row) and EN2-119 (bottom row). We plot spectroscopically confirmed cluster members with [OII] emission in yellow, and those without in pale green.

Table 4.2 The *Herschel*-SPIRE fields.

HerMES Name	OBSIDs	Time per AOR (hrs)	Total Integration Time (hrs)	Area (sq. deg.)
ELAIS N1 SWIRE	1342228450	13.6	28.0	9.3
	1342228354	14.4		
ELAIS N2 SWIRE	1342214712	8.6	16.8	4.8
	1342226997	8.2		

which contain our three clusters, and reduce the data ourselves. The observations derive from the Herschel Multi-tiered Extragalactic Survey (HerMES), the largest program carried out with *Herschel*, covering ~70 square degrees (Oliver et al., 2012). Both fields belong to the level 6 tier of the survey, meaning they are wide-field but relatively shallow depth, and were observed in parallel mode with PACS and SPIRE. We summarize the properties of the observations in Table 4.2.

In general, we follow the default pipeline for reducing large SPIRE maps in parallel mode, with a few modifications when necessary. Processing each AOR separately, the pipeline first loops over the scans, correcting for various artifacts along the way, including jumps in the thermistor timelines, cosmic ray glitches, low temperature noise drifts, and pointing calibrations. At this stage, the timelines are also converted from volts to janskys per beam, and we combine the scans from each AOR (with orthogonal scan directions) to complete the processing with merged scans.

The next step involves making a correction for residual offsets between detectors, which can lead to stripes in the map. This can be corrected for with a number of methods, the default being a subtraction of the median from each scan, which in some cases is insufficient. The SPIRE Destriper module, however, has been found to produce optimal results in general, though it is more memory intensive. This algorithm iteratively removes the offsets by adjusting the baseline removal with either a simple median or polynomial fit of a specified degree. We use the latter approach, with a zeroth order polynomial for the Elais North 2 field, and a first order polynomial for the Elais North 1 field, which was found to have significant stripes with the zeroth order fit. Finally, the baseline-removed scans are passed to the map maker; again we use the default naive mapper, which projects each bolometer signal onto a sky pixel, and creates a flux density map by dividing the total signal map by the coverage map.

4.3 ANALYSIS

To improve our statistics, we perform stacking analyses (see Sections 4.3.1 and 4.3.3) to study the average properties of cluster members, rather than individually detected objects. We utilize the extensive spectroscopy available over all three clusters (123 members), but focus on non-passive galaxies (defined by the presence of [OII] emission), as we are primarily interested in environmental effects on star formation activity. After removing quiescent galaxies from the sample, we are left with 58 star-forming galaxies (13, 22, and 23 in EN1-349, EN2-111, and EN2-119, respectively). We note that EN1-349 actually has 14 star-forming galaxies, but one faint 100 μm source has been removed as it was too close to a 100 μm-bright cluster member which was contaminating the aperture of the faint source. We further divide the sources into phase-space bins (as described in Chapter 3), with $(r/r_{200}) \times (\Delta v/\sigma_v) < 0.1$ (low bin), $0.1 < (r/r_{200}) \times (\Delta v/\sigma_v) < 0.4$ (medium bin), and $(r/r_{200}) \times (\Delta v/\sigma_v) > 0.4$ (high bin). These final bins contain 8, 11, and 39 sources, respectively.

4.3.1 PACS Stacking

For each bin, we stack the PACS maps at 100 and 160 μm combined over all three clusters, using the following approach. We extract a thumbnail image around each source, just large enough to cover the recommended annulus for sky estimation (see Section 4.3.2), yielding a radius of 26 arcsec for 100 μm and 30 arcsec for 160 μm. We mask the inner pixels of the thumbnails (6 and 12 arcsec), just encompassing the required radius for aperture photometry at each wavelength, and perform a 4σ

clipping on the remaining pixels to remove any bright sources within the extracted map. The clipped map is then weighted by the inverse of the variance, calculated over the non-clipped and non-masked pixels. We combine all subsequent thumbnails to make a cube for each bin, where each layer represents the clipped, weighted map with the inner masking now removed. Along the cube dimension, we perform a trimmed average: we first discard the minimum and maximum pixel values along all layers in the cube (not including the clipped values), pixel by pixel, and calculate the mean in the remaining pixels. Finally, we normalize by the total of the inverse variance associated with the pixels that contribute to the trimmed mean. The resulting map, a flattened cube that has been averaged (with trimming) pixel by pixel with each layer inverse weighted and 4σ clipped, represents our stacked image and is shown in the bottom panels Figures 4.2 and 4.3 for each phase-space bin. For comparison, we also show a simple average stack for the same bins (upper panels), which suffer from high contamination from neighboring sources.

4.3.2 PACS Aperture Photometry

We perform aperture photometry on the final stacked images within the HIPE V11.0 environment, using the recommended radii for faint sources: 5.6, 20, 25 arcsec (10.5, 24, 28 arcsec) for source flux, inner sky annulus, and sky annulus, respectively at 100 μm (160 μm). The sky estimate is determined from an algorithm adapted from DAOPHOT which iteratively computes the mean and standard deviation of the provided sky pixels, each time removing possible outliers, and is ultimately subtracted from the source flux.

The aperture radii are below the nominal FWHM of the beam at each wavelength, which helps to reduce contamination from any residual flux from neighboring sources that was not removed during stacking. However, we must then apply an aperture correction to properly account for the missing flux that is not captured within the

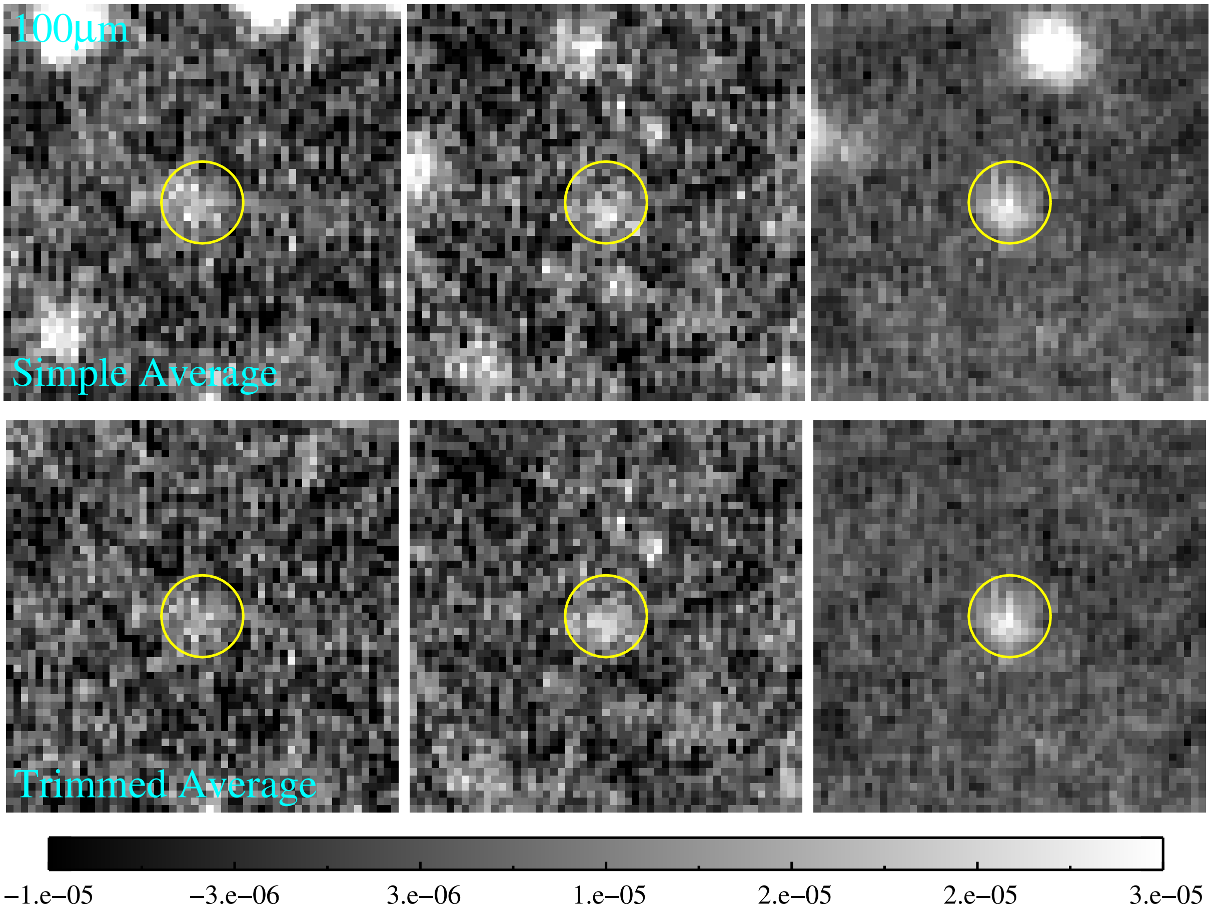

Figure 4.2 Stacked images for each phase-space bin at 100 μm. The left, middle, and right column show lower to higher phase-space bins: $(r/r_{200}) \times (\Delta v/\sigma_v) < 0.1$, $0.1 < (r/r_{200}) \times (\Delta v/\sigma_v) < 0.4$, and $(r/r_{200}) \times (\Delta v/\sigma_v) > 0.4$, respectively. The upper panel displays the resulting stack from a simple average, while the lower panel represents a weighted, clipped, and trimmed average, as described in Section 4.3.1. The removal of contamination in the lower stacks is evident. We also include the radius used for aperture photometry, 5.6 arcsec, with the yellow circle. The colour bar shows the gray scale in janskys per pixel.

given radius. These corrections are calculated with version 7 of the responsivity function for various apertures in each band: 0.57 for 5.6 arcsec at 100 μm and 0.64 for 10.5 arcsec at 160 μm.

As described in Section 4.2.2, we must also include a correction for flux loss due

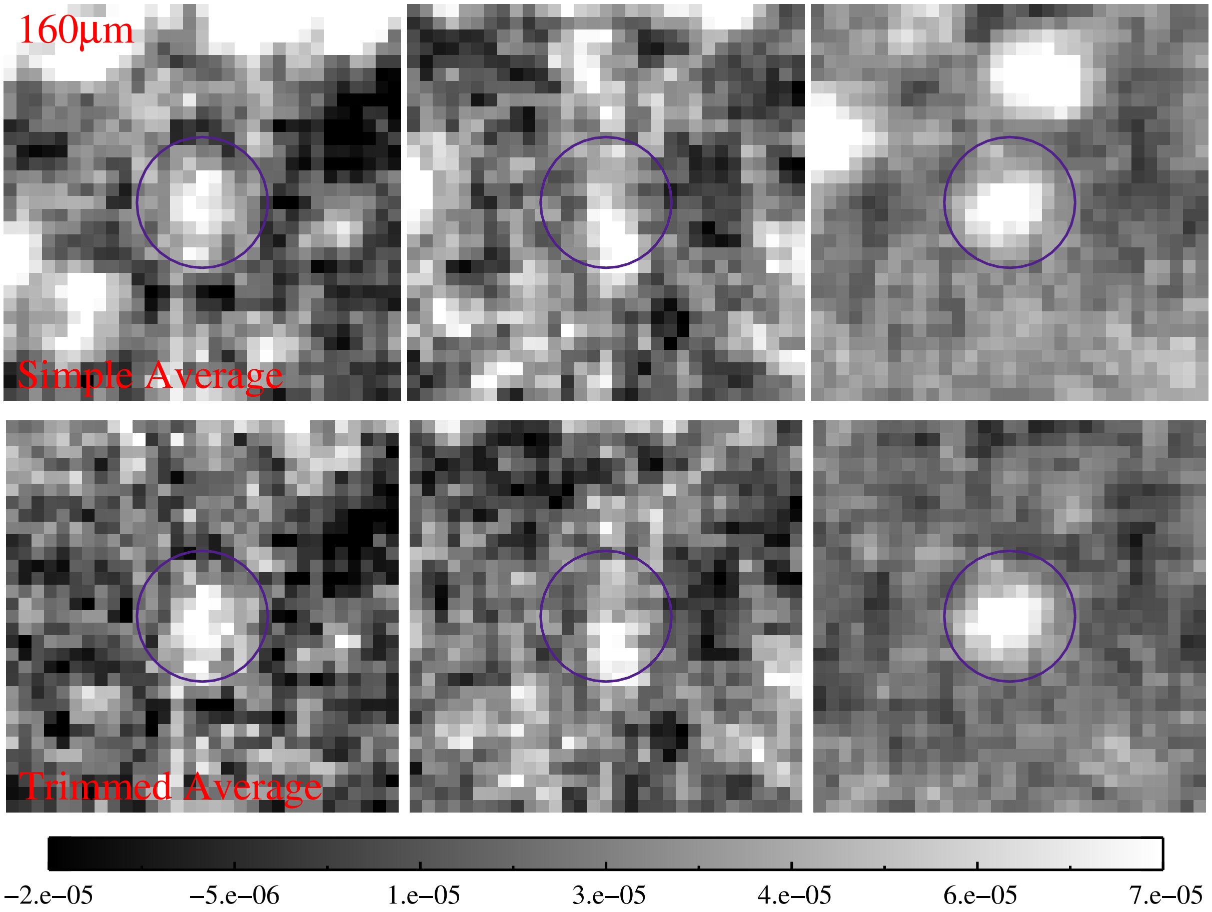

Figure 4.3 Stacked images for each phase-space bin similar to those in Figure 4.2, but at 160 μm. The purple circles represent apertures of 10.5 arcsec.

to the high-pass filtering during the removal of $1/f$ noise. These multiplicative factors have been calibrated by Popesso et al. (2012) for various parameters, including aperture radii, high-pass filter radii, scan speeds, etc, and are equal to 0.93 for 100 μm and 0.86 for 160 μm. After applying these aforementioned corrections, the final source flux is given by:

$$S_{\mathrm{true}} = \frac{S_{\mathrm{ap}}}{corr_{\mathrm{HPF}}(r_{\mathrm{ap}}) \times corr_{\mathrm{ap}}(r_{\mathrm{ap}})}, \tag{4.1}$$

where $S_{\rm ap}$ is the background subtracted flux, $corr_{\rm HPF}(r_{\rm ap} = [5.6, 10.5]) = [0.93, 0.86]$, and $corr_{\rm ap}(r_{\rm ap} = [5.6, 10.5]) = [0.57, 0.64]$. We bootstrap the sources 100 times in each phase-space bin and calculate the standard deviation on the mean to determine the errors on the binned fluxes.

4.3.3 SPIRE Stacking

The large beam at SPIRE wavelengths (18.2, 24.9, and 36.3 arcsec FWHM at 250, 350, and 500 μm, respectively) renders traditional stacking analyses difficult. This is due to the confusion-limited nature of the maps, which is typically reached when the source density surpasses $\sim$0.02–0.03 beam^{-1} (Condon, 1974); this is found to occur at 18.7, 18.4, and 13.2 mJy (at 40 beams per source) with ascending SPIRE wavelengths (Oliver et al., 2010). As a result, a single flux peak in the map is likely to have contributions from a sea of fainter, unresolved sources and disentangling these fluxes can be problematic. Moreover, this effect amplifies when one considers intrinsically correlated populations, as they are expected to be clustered on large beam scales.

Monte Carlo simulations can circumvent this problem by correcting for the bias measured in stacked fluxes. However, an even cleaner approach lies in fitting the stacked fluxes of correlated populations simultaneously. An algorithm called SIMSTACK developed specifically for SPIRE maps by Viero et al. (2013) exploits the latter technique and has been made publicly available.

The general method relies on separating potentially clustered populations into individual lists; in our case, we divide the sources into phase-space bins. The central idea is to construct template maps from each list and simultaneously fit them to the real map data; the best-fit amplitude of each template then corresponds to the average stacked flux for that list. More specifically, for every input map (i.e., the three SPIRE wavelengths), a “hits map” is created from each list separately, where pixels are assigned an integer value corresponding to the number of sources that fall within it (or given a value of zero if empty). These maps are smoothed with a Gaussian (given by the FWHM of the beam), and are then mean-subtracted. For each list, a vector is populated with the values in the mean-subtracted smoothed map at pixels of interest; these include all pixels within a circle of radius 1.1×FWHM around each source (combined from all lists) and anything not within an optional user-supplied mask. This results in a vector of the same length for each list with the beam-convolved mean-subtracted values given in the pixels of interest. All vectors are passed to the fitting routine of the functional form

$$M_j = \sum_{\alpha} S_\alpha C_{\alpha j}, \tag{4.2}$$

where M_j corresponds to the real map values in j pixels of interest, $C_{\alpha j}$ is the beam-convolved mean-subtracted values in the pixels of interest for each list α, and S_α is the stacked flux in list α. This process is iterated until the resulting χ^2 is minimized, yielding a stacked flux for each list. The entire procedure is subsequently repeated for each SPIRE wavelength. Since the fluxes are fit simultaneously from all lists, it effectively allows for a deconvolution of the flux contribution from multiple sources within a beam (assuming that all these sources were detected in the original catalog).

Since we aim to combine sources from all three clusters into each phase-space bin, we slightly alter the public code to suit our needs. Specifically, we create a separate beam-convolved mean-subtracted "hits map" for each field, and then merge the resulting vectors together (along with merged vectors of real data) to pass to the fitting routine.

In order to optimize the functionality of SIMSTACK for reducing the bias due to beam-size clustering, we also simultaneously pass catalogs with 24 μm prior positions to the fitting routine. The catalogs include every 3σ MIPS source detected above 70 μJy (roughly the completeness limit in each map) with any cluster members removed

Table 4.3 *Herschel* stacked flux densities in phase-space bins.

Wavelength (μm)	$0.1 < r \times v$ (mJy)	$0.1 < r \times v < 0.4$ (mJy)	$r \times v > 0.4$ (mJy)
100	1.2 ± 0.7	1.7 ± 0.8	1.9 ± 0.5
160	3.7 ± 2.2	3.0 ± 2.1	4.0 ± 1.4
250	1.5 ± 0.8	5.7 ± 0.8	2.4 ± 0.4
350	—	4.7 ± 0.8	2.7 ± 0.4
500	—	5.7 ± 0.9	1.5 ± 0.4

(as those are already included in the phase-space catalogs). We split the MIPS catalogs (combined over all three clusters) into four flux bins to isolate galaxies with the same average properties: 70–100 μJy, 100–200 μJy, 200–300 μJy, and > 300 μJy. We plot the resulting stacked SPIRE fluxes for all seven catalogs that are simultaneously fit in Figure 4.4. Error bars are computed from the standard deviation on 100 bootstrapped means for each bin. The final stacked flux densities in each phase-space bin for all five *Herschel* wavelengths are listed in Table 4.3.

4.4 Results and Discussion

4.4.1 Infrared Spectral Energy Distributions

With broad characterization of the thermal portion of the spectral energy distribution, we can fit modified blackbodies to the stacked fluxes to estimate the infrared luminosity of each population. We adopt the modified blackbody from equation 1.3, described in Section 1.3.1, and fit for the dust temperature. We keep the slope of the emissivity, β, fixed to a typical value of 1.7—with the accepted range of values between 1.5–2.0 (Dunne et al., 2000). We note that fixing β at either limit does not alter the resulting dust temperatures beyond their 1σ uncertainties. There is also a strong degeneracy between dust temperature and redshift, as both parameters alter the location of the thermal peak in a similar manner: colder temperatures and increasing redshift shift the peak to longer wavelengths and attenuated fluxes.

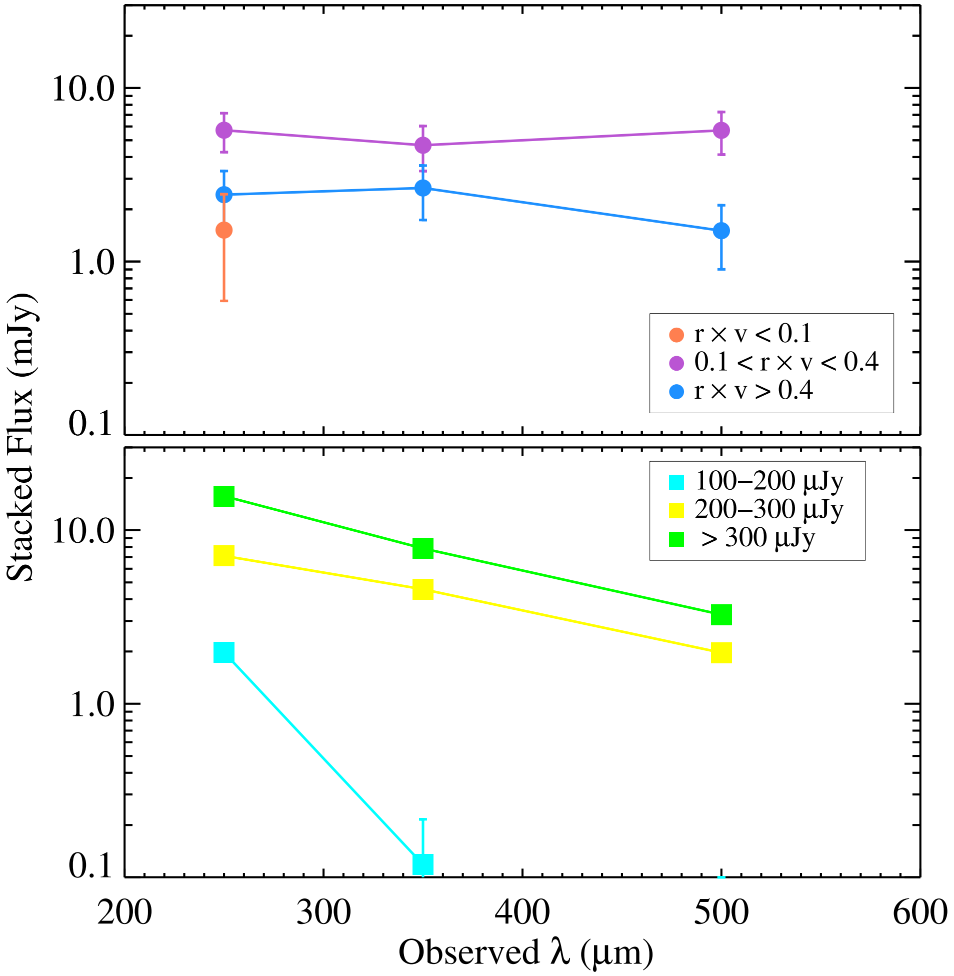

Figure 4.4 Stacked flux densities in the SPIRE maps using our modified version of SIMSTACK. We simultaneously stack seven catalogs, three of which include star-forming cluster members in phase-space bins (upper panel; filled circles), and four from MIPS prior positions separated by flux (lower panel; filled squares). The flux at the lowest phase-space bin (orange circles) is only detected at 250 μm; the 70–100 μJy MIPS bin is not detected at any wavelength and therefore is not plotted; and the 100–200 μJy MIPS bin (cyan squares) lacks a stacked detection at 500 μm.

However, stacking on spectroscopically confirmed star-forming members removes this problem as we no longer need to fit for the redshift, reducing the final errors on the dust temperature.

The best-fit spectral energy distributions for the three phase-space bins are shown

Table 4.4 Best fit spectral energy distributions for stacked cluster members in phase-space bins.

Phase-Space Bin	Curve Colour	Average z	$T_{\rm dust}$ (K)	$L_{\rm IR}$ (10^{11}L$_\odot$)	SFR (M$_\odot$ yr^{-1})	SSFR (yr^{-1})	χ^2/n
$0.1 < r \times v$	orange	1.18	53±12	$2.4^{+3.8}_{-1.7}$	25^{+40}_{-18}	$0.1^{+0.2}_{-0.1}$	0.2
$0.1 < r \times v < 0.4$	purple	1.17	28±4.3	$3.6^{+3.8}_{-2.1}$	38^{+40}_{-22}	$1.2^{+1.2}_{-0.7}$	1.7
$r \times v < 0.4$	blue	1.18	48±4.5	$3.9^{+2.0}_{-1.5}$	41^{+21}_{-15}	$0.9^{+0.5}_{-0.3}$	0.8

in Figure 4.5 with the resulting values for $T_{\rm dust}$. We convert these curves into luminosities (L_λ) using equation 1.4 and integrate over rest-frame 8–1000 μm to obtain the average infrared luminosity: 2.4×10^{11}, 3.6×10^{11}, and 3.9×10^{11} L$_\odot$ for ascending phase-space bins. The star formation rates from the total infrared luminosity can then be calculated using the relation from Kennicutt (1998a), equation 2.3. The derived properties and fit parameters are listed in Table 4.4.

4.4.2 Specific Star Formation Rate as a Function of Phase-Space

Infrared luminosities derived from fits to spectral energy distributions that span the peak of the thermal emission should provide robust estimates of the bolometric star formation rate within galaxies (Kennicutt et al., 2009), as they trace dust emission both directly and indirectly related to star formation. The former tracer includes any dust that is directly heated from ultraviolet radiation from young stars, while the latter describes the inherent association between dust and gas—the raw fuel for star formation. Dust grains are essential to the process of star formation, providing the catalyst for the formation of molecular gas: pairs of hydrogen atoms within HI regions adsorb on cool ($T \lesssim 25$ K) grains, forming molecular hydrogen (Hollenbach and Salpeter, 1971). Dense pockets of H_2 within cool molecular clouds are stellar nurseries, as they gravitationally collapse, fragment, and eventually form protostars. The widely-used Kennicutt-Schmidt law for star formation states that its rate is

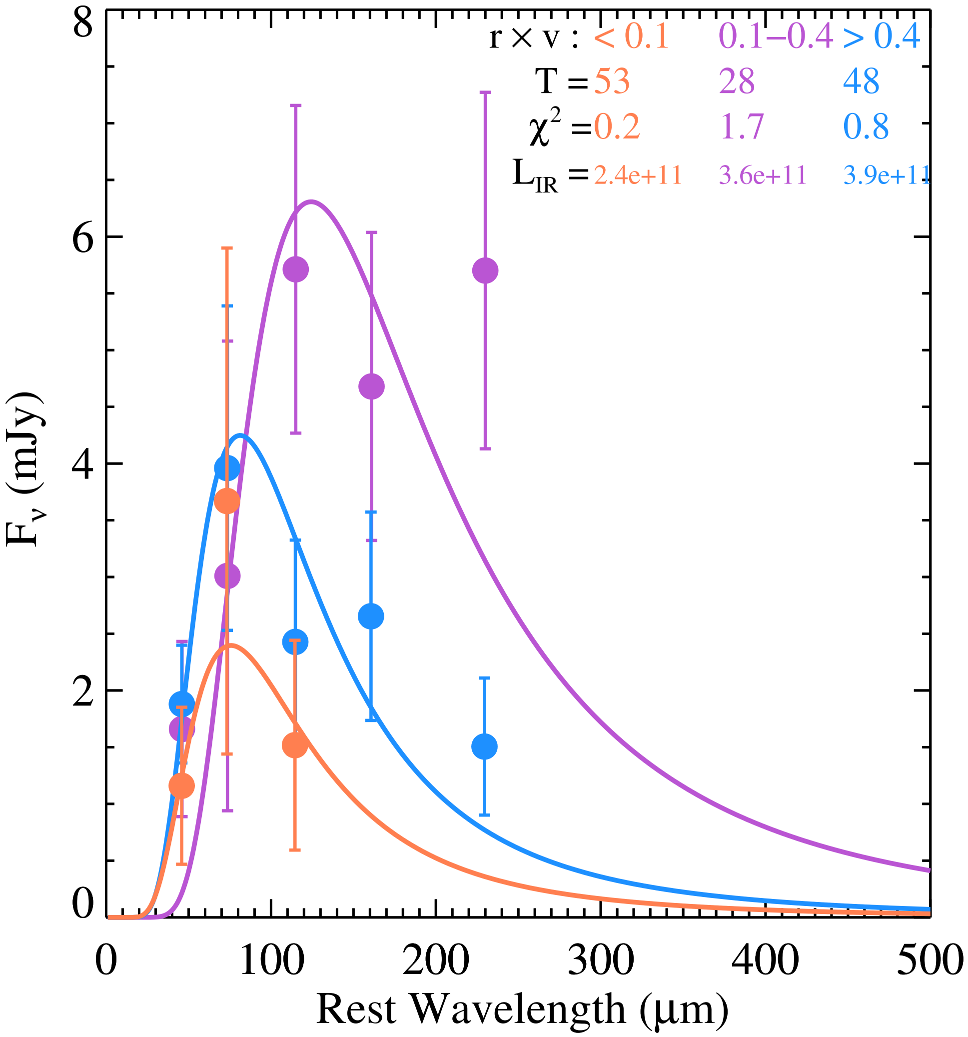

Figure 4.5 Modified blackbody fits to the thermal portion of the spectral energy distribution using five wavelengths from stacked *Herschel*-PACS (100 and 160 μm) and *Herschel*-SPIRE (250, 350, and 500 μm) fluxes, shown as solid circles. The best fit for each phase-space bin is represented by the solid line, with the resulting parameter values for dust temperature (in units of Kelvin) and reduced χ^2 listed. The orange, purple, and blue colours correspond the ascending phase-space bins: $(r/r_{200}) \times (\Delta v/\sigma_v) < 0.1$; $0.1 < (r/r_{200}) \times (\Delta v/\sigma_v) < 0.4$; and $(r/r_{200}) \times (\Delta v/\sigma_v) > 0.4$, respectively. The lowest phase-space bin (orange curve) does not have detections at 350 and 500 μm, and therefore is fit solely with the remaining three flux values. These fits allow for determination of the integrated infrared luminosity, given in units of $L_{\odot}$.

proportional to the gas surface density raised to the power of index n, SFR $\propto \Sigma_{gas}^{n}$, where $n \sim$1–2 (Schmidt, 1959; Kennicutt, 1998b). Thus, since dust is associated with hydrogen, it provides an indirect gauge of regions conducive to star formation.

In the upper panel of Figure 4.6, we plot the total infrared luminosity-derived star formation rates as a function of phase-space bin, representing earliest accreted (or virialized) objects in the lowest bin, intermediate objects in the middle bin, and the most recently accreted population at the largest values of $r \times v$. We perturb the best fit dust temperatures by $\pm 1\sigma$ and re-integrate the modified blackbody to estimate errors on the infrared luminosities and star formation rates. The resulting star formation trend is flat as a function of dynamically-defined environment within the uncertainties. This is due to the high degree of mass segregation in clusters, with more massive galaxies, which inherently form stars at a higher rate, residing deeper in the cluster potential. In the lower panel, we correct for this effect, plotting the specific star formation rate (star formation rate per unit stellar mass). We find a decline in specific star formation rate with accretion history, with a ∼1 dex drop between infalling/intermediate galaxies and those accreted at earlier times. This confirms our work in Chapter 3 with MIPS galaxies in a $z = 0.872$ cluster, but now with a larger sample of star-forming galaxies, more robust star-formation rates, and at a higher redshift of $z = 1.2$. This could be suggestive of environment playing an active role in the quenching of star formation, rather than just controlling the fraction of star-forming galaxies; however, we need to further control for stellar mass to disentangle any effects from mass-quenching in order to elucidate the precise role of environment.

4.4.3 Dust Temperatures for Dynamically-Isolated Populations

In Figure 4.7, we plot the best-fit dust temperatures for each stacked phase-space bin, thereby isolating galaxy populations by accretion epoch and relative dynamics within

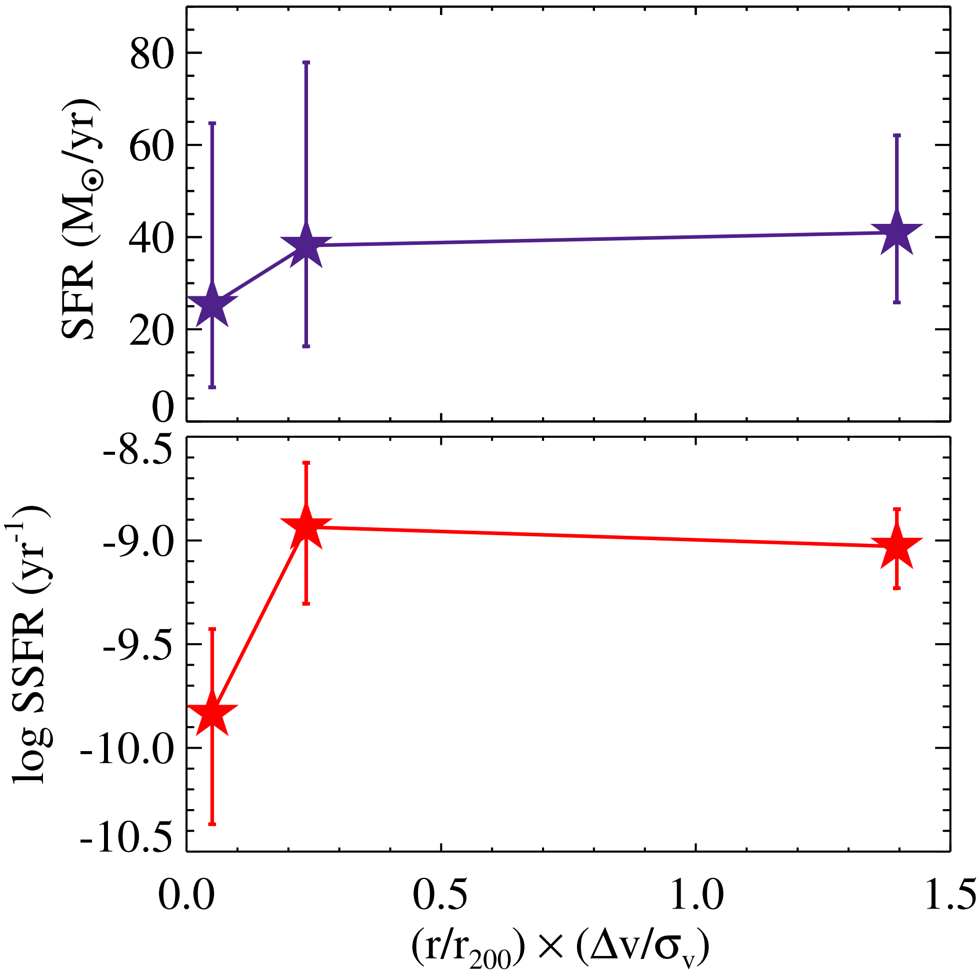

Figure 4.6 The star formation rate (upper panel) and specific star formation rate (lower panel) for star-forming galaxies as a function of phase-space. Star formation rates are derived from PACS and SPIRE fits to the thermal portion of the spectral energy distribution. Uncertainties are estimated from shifting the best fit dust temperature by $\pm 1\sigma$ and recalculating the infrared luminosity. We find the specific star formation to be constant between recently accreted and intermediate galaxies, but declines with the earliest accreted cluster galaxies.

the cluster. We find that the early- and recently-accreted populations are dominated by warm dust of $T \sim 50\,\mathrm{K}$, whereas the intermediate population has colder dust at $T \sim 30\,\mathrm{K}$. Attempting to fit a straight line to the data leads to a slope discrepant with zero at 2.7σ (13.7 ± 5.1), and moreover, is a poor representation of the data with reduced $\chi^2 = 4.7$. In order to interpret this temperature deficit we must expand upon the interplay between gas and dust within galaxies.

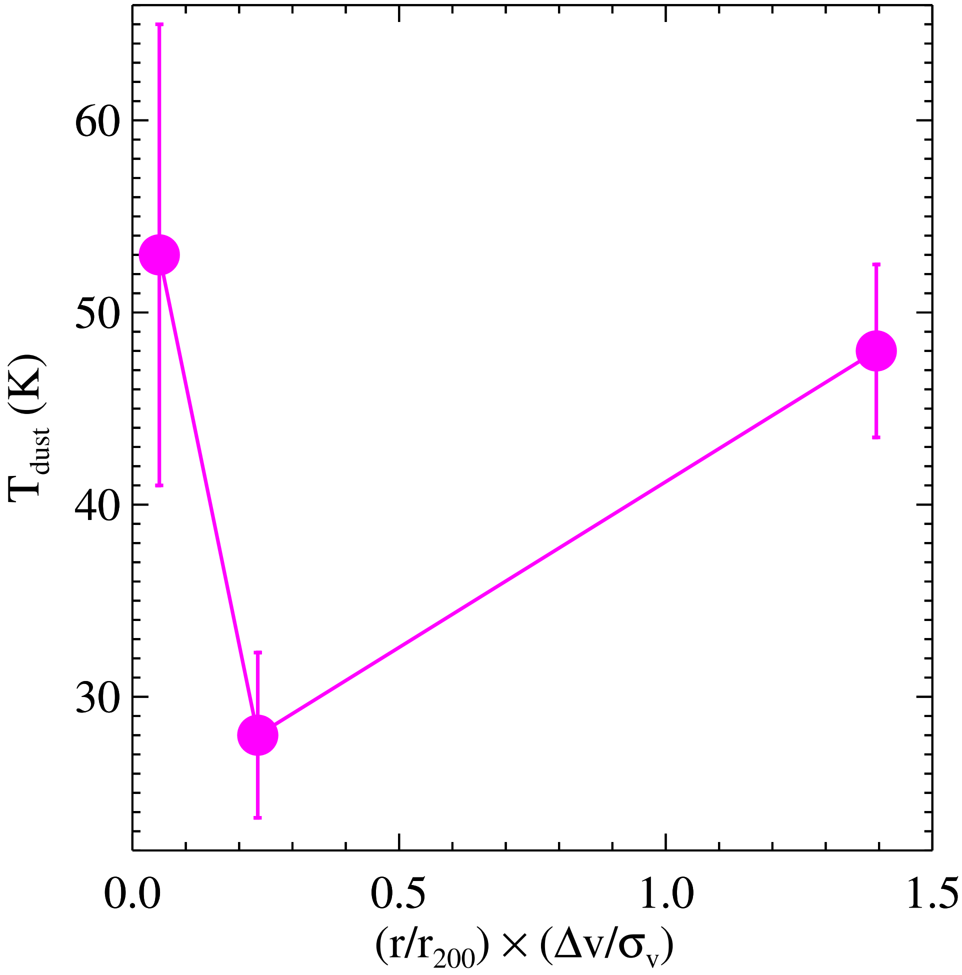

Figure 4.7 The best-fit dust temperature for each stacked population in phase-space. The intermediate galaxies (middle phase-space bin) display the coldest dust temperature ($\sim 30\,K$). The uncertainties are 1σ errors on the temperature from fits to the spectral energy distribution assuming β is fixed at 1.7.

The gamut of dust grain sizes gives rise to many features in the infrared regime. Many studies have attempted to disentangle the dust temperature components with specific gas phases in the interstellar medium. Earlier work primarily focused on the warmer dust component on the Wien side of the spectrum, utilizing the available infrared bands with *IRAS* (12, 25, 60, and 100 μm) and out to slightly longer wavelengths (160/170 μm) with *ISO* and *Spitzer* (e.g., Cox et al., 1986; Helou, 1986; Bicay and Giovanelli, 1987; Boselli and Gavazzi, 2006). For example, Cox et al. (1986) proposed a four-component model for dust temperature and gas in the galactic disk. The hottest dust ($250 < T < 500$ K) consists of both moderately-sized grains (radius $\sim 0.1\,\mu$m) and smaller-sized grains (PAHS; radius $\sim 1\,$Å). These grains are transiently heated by evolved stars (peaking at $\lambda \sim 5\,$Å) and the general interstellar radiation field (at mid-infrared wavelengths), respectively, and trace the diffuse hydrogen gas. Warm dust ($T \sim 40$ K) at ∼40–100 μm is associated with the younger stellar population, and therefore probes ionized gas. The atomic hydrogen in the galactic disk comprises cooler dust of 20–30 K and peaks at 100 μm. The coldest dust ($T \sim$20–30 K) traces quiescent molecular clouds, and is subdominant to the cool emission; recent studies find that the 80% of the luminosity budget in the Galaxy stems from atomic hydrogen (e.g., Paladini et al., 2007). Both the cooler components are heated by the total stellar population, including young and old stars. Similar multi-component dust models were found for larger samples of star-forming galaxies: a warm ($T \sim 50$ K) component associated with younger stars and HII regions; and a cool cirrus component ($T \sim 25$ K) heated by the general radiation field (de Jong et al., 1984; Helou, 1986; Dunne and Eales, 2001). However, these analyses lacked data in the regime dominated by cold dust emission ($200 \lesssim \lambda \lesssim 400\,\mu$m).

The advent of PACS and SPIRE instruments on *Herschel* has now permitted studies to link different dust temperatures peaking at these previously absent wavelengths with phases of the gas (Bendo et al., 2010, 2012; Boselli et al., 2012; Bourne et al., 2013). It is becoming evident that the evolved stellar population plays a role in heating the large grains associated with the colder dust at $\lambda > 160\,\mu$m, and may even be the dominant source of heating at $\lambda > 250\,\mu$m in nearby spirals (Bendo et al., 2012). Much of the cold dust exists in the interstellar medium, while the warmer dust lies within the confines of optically-thick star-forming regions. It thereby insulates the surrounding colder dust from the strong radiation field from young stars, though some leakage is expected (Dunne and Eales, 2001; Kennicutt et al., 2009). However, many recent studies have found that far-infrared wavelengths correlate with direct tracers of star formation and gas, indicating that the cold dust is at least partially heated from younger stars, or probes the density of diffuse gas that fuels star formation. For example, in a nearby spiral galaxy, Verley et al. (2010) discovered a strong relation between compact 250 μm emission and both 24 μm and Hα emission, which are known indicators of star formation. Moreover, Bourne et al. (2013) claim that a trend exists between gas phases and far-infrared emission in local spiral galaxies: dust at 60–500 μm shows a significant correlation with dense molecular gas (CO 3–2), with emission at 100 μm being the best tracer. Cold dust peaking at 250–500 μm roughly follows emission from more diffuse molecular gas (CO 2–1) and has an even stronger trend with atomic gas (HI). They also find a robust relation between CO 2–3 and HI, implying high amounts of atomic gas are necessary for large reservoirs of dense molecular gas.

In light of the interplay between gas and dust, we can attempt to understand how a drop in dust temperature might arise for intermediate galaxies (some of which are possibly backsplash galaxies) with infrared colour ratios. In Figure 4.8 we show the infrared colours for each phase-space bin. Colours are primarily sensitive to the mechanism heating the dust, as opposed to single emission bands which also depend on the surface density (Bendo et al., 2012). We plot the colour ratio for observed $\mathrm{f}_{250}/\mathrm{f}_{160}$ against $\mathrm{f}_{160}/\mathrm{f}_{100}$, corresponding to emitted ratios at $z = 1.2$ of $\mathrm{f}_{114}/\mathrm{f}_{73}$ and $\mathrm{f}_{73}/\mathrm{f}_{45}$. According to the above dust phases, these colours should roughly represent dust heated by the total stellar population, including partial contributions from older and younger stellar populations, and dust heated primarily by ionizing stars in HII regions, respectively. Moreover, a higher luminosity of 100 μm emission might be indicative of a large reservoir of dense molecular gas. Therefore, colder (higher) ratios at emitted f_{114}/f_{73} might imply an increased contribution of heating from older stellar populations and/or the existence plentiful H_2 regions, while warmer (lower) ratios of f_{73}/f_{45} denote a prominent contribution from hotter dust associated with young stars. We see a vague trend in our star-forming sample with f_{114}/f_{73} getting cooler as f_{73}/f_{45} gets warmer, albeit with large uncertainties. The intermediate galaxies have both the coolest f_{114}/f_{73} ratio and warmest f_{73}/f_{45} ratio.

4.4.4 A Simple Interpretation for Quenching

We attempt to explain the above star formation and dust temperature trends with a simple interpretation of the possible quenching mechanisms at work. Strangulation or increased merging activity are the most likely processes in the cluster outskirts (Treu et al., 2003). Since we currently do not have a stacked field sample with which to compare, we cannot postulate whether infalling galaxies have increased star formation rates compared to $z = 1.2$ field galaxies, though we note the specific star formation rate is consistent with the $z \sim 1$ field trend in Figure 3.5. Strangulation, however, seems to be a viable explanation for the transition between the recently accreted and intermediate galaxies. This mild process works on long timescales by removing the hot gaseous halo of atomic and ionized hydrogen, while leaving the cold disk gas untouched (Larson et al., 1980; Balogh et al., 2000). This leads to a gradual decline in star formation—on the timescale of cold gas consumption—as it only exhausts the fuel for future cooling. Spiral galaxies are likely to contain diffuse ionized gas in their halo that is associated with the presence of dust (Howk and Savage, 1999; Ménard et al., 2010). This warmer dust component could be stripped along with the gas (Boselli and Gavazzi, 2006), which could lead to an immediate drop in dust temperature while preserving the current star formation rate. It is therefore consistent with the change in the global dust temperature between the infalling and intermediate populations.

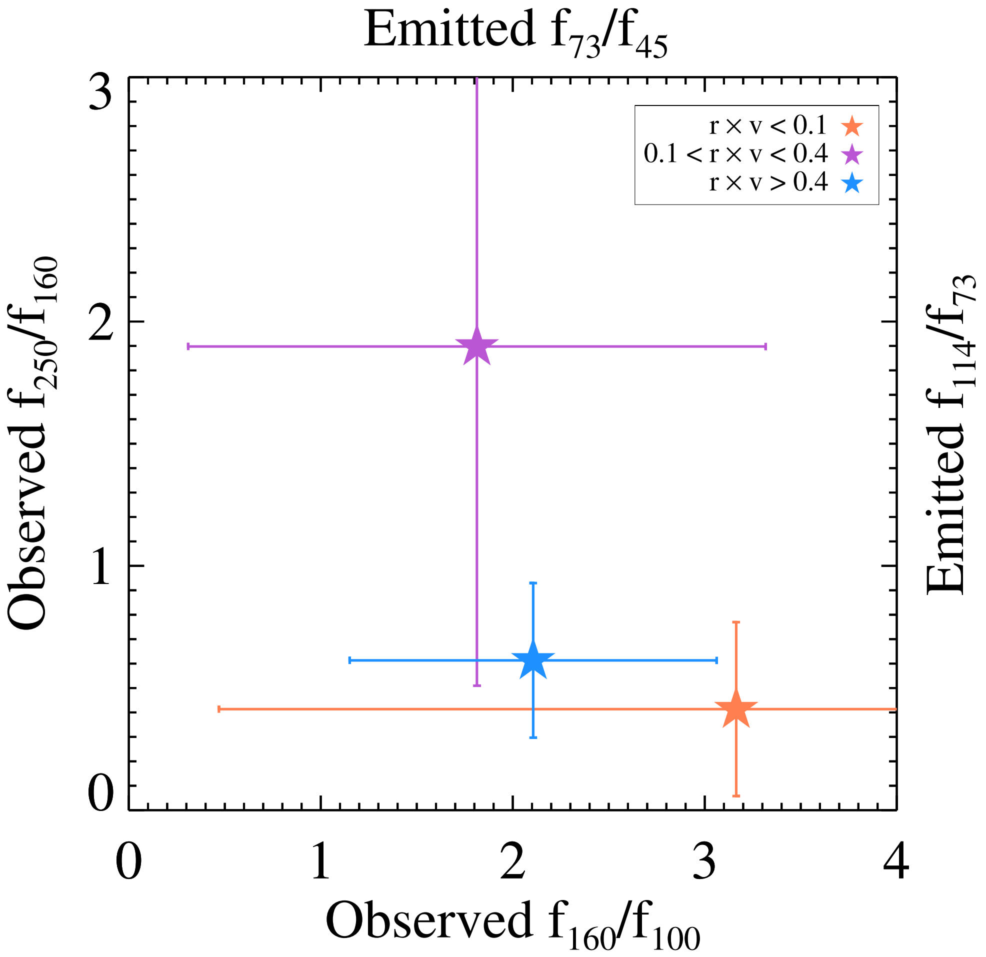

Figure 4.8 An infrared colour-colour diagram for the three phase-space bins: orange ($r \times \Delta v < 0.1$); purple ($0.1 < r \times \Delta v < 0.4$); and blue ($r \times \Delta v > 0.4$). The observed f_{250}/f_{160} colour corresponds to f_{114}/f_{73} at $z = 1.2$, and observed f_{160}/f_{100} corresponds to a rest-frame colour of f_{73}/f_{45}. We see a rough trend of increasing f_{114}/f_{73} with decreasing f_{73}/f_{45}. The intermediate population (purple star) has the coldest f_{114}/f_{73} and warmest f_{73}/f_{45} ratio.

For this simple interpretation, let us assume the intermediate population has properties similar to those of backsplash galaxies (i.e., close to pericenter in their orbit). In reality, it might consist of a mixture of all galaxy types, but as we discussed earlier, the middle phase-space bin is where the statistical majority of backsplash galaxies should exist. Backsplash galaxies possess high relative velocities and encounter dense gas as a result of being close to pericenter in their orbit. These conditions are conducive to ram-pressure stripping which can effectively remove the entire HI component in the disk. The high densities within molecular clouds, however, make them impenetrable to the effects of stripping (Gunn and Gott, 1972; Quilis et al., 2000). This mechanism is therefore thought to have a delayed, then rapid ($\lesssim 100\,\mathrm{Myr}$), effect on star formation (Wetzel et al., 2012, 2013); molecular clouds already in existence can still efficiently form stars, but the removal of atomic disk gas prevents further production of molecular hydrogen. Star formation thus ceases on the scale of a molecular cloud lifetime (approximately tens of millions of years; Blitz and Shu, 1980). The infrared colours of the middle phase-space bin ($0.1 < r \times \Delta v < 0.4$) support this scenario: they exhibit both a warm dust component from ongoing star formation; and an increasing component of cooler dust, presumably heated by recent and evolved stars. The elevated $\mathrm{f}_{114}/\mathrm{f}_{73}$ colour is suggestive of HI-deficient galaxies (Bicay and Giovanelli, 1987; Doyon and Joseph, 1989), which is commonly seen in cluster (and group) galaxies (e.g. Hess and Wilcots, 2013). The high $113\,\mu$m rest-frame flux is also indicative of the presence of a reservoir of dense molecular gas (Bourne et al., 2013). This is expected from ram-pressure stripping, which is incapable of removing the molecular clouds and can even lead to their compression from the encountered shock with the intracluster medium (Fujita and Nagashima, 1999), possibly triggering bursts of star formation. While our results are consistent with a prevalence of dense molecular gas in intermediate galaxies, we do not see evidence for enhanced star formation compared to the recently accreted galaxies.

The earliest accreted galaxies display depressed specific star formation rates. They also have the lowest warm dust component (corresponding to the coldest $\mathrm{f}_{73}/\mathrm{f}_{45}$ colour), and little-to-no longer-wavelength cold dust, as shown by the lack of detections at 350 and $500\,\mu$m in the observed frame. These galaxies have probably exhausted much or all of their molecular gas, and are (likely) completely HI deficient. Their residual star formation is evidenced by a diminishing contribution of dust heated by young stars. Given that ram-pressure results in a rapid quenching timescale, specific star formation rates observed at depressed values might instead stem from a population of galaxies that have had their gas slowly exhausted.

Our simple interpretation—a combination of strangulation and ram-pressure stripping as viable quenching mechanisms—is compatible with other studies. For example, many groups invoke long quenching timescales to explain observed star formation and colour trends which are indicative of a slow removal or heating of gas. In high-redshift groups, Balogh et al. (2011) discover a population of galaxies with intermediate optical colours falling between the quiescent red-sequence and star-forming blue cloud, evident of slow and continuous gas exhaustion. Haines et al. (2013) also propose a long quenching timescale to explain lower specific star formation rates in $0.15 < z < 0.3$ cluster galaxies once they pass within $1.5r_{200}$, indicative of strangulation or ram-pressure stripping.

On the other hand, many studies observe discrete or binary trends in star formation activity, attributable to a rapid quenching mechanism. Wetzel et al. (2012) find a bimodal distribution of specific star formation rates, split between central and satellite galaxies in $z \simeq 0$ group and cluster galaxies from the SDSS. They claim that environment has little effect on satellite galaxies until they cross the virial radius. They derive quenching timescales to explain this trend (Wetzel et al., 2013), finding a plausible scenario in which satellite galaxies undergo delayed (∼2–4 Gyr), then rapid (< 0.8 Gyr) quenching, likely due to ram-pressure stripping. In a large sample of clusters over $0.3 < z < 1.5$, Alberts et al. (2013) propose multiple mechanisms for altering star formation rates, including strangulation in higher-mass galaxies, and increased merger occurrences for lower mass galaxies in the cluster outskirts at $z \sim 1.4$. They also suggest ram-pressure stripping might be responsible for a quick transition in the fraction of star-forming galaxies within the clusters at all redshifts. Moreover, direct evidence for ram-pressure stripping—in the form of trailing HI gas tails on spiral galaxies—has previously been observed in the Virgo cluster (Chung et al., 2007).

Further support for mechanisms which quench star formation rapidly after a delayed period emerges with the observed abundance of poststarburst galaxies in clusters compared to the field (e.g., Dressler et al., 1999; Poggianti et al., 1999, 2009; Tran et al., 2004, 2007; De Lucia et al., 2009; Muzzin et al., 2012). These galaxies exhibit strong Balmer absorption (e.g., Hδ) and weak emission lines (e.g., little-to-no [OII] emission), indicative of star formation that ended abruptly within the last few hundred million years (Dressler and Gunn, 1983; Couch and Sharples, 1987). They are often referred to as "K+A" galaxies due to their spectral similarities to average A-type stars (with $\sim 1\,$Gyr lifetime) superimposed with an older K spectrum. A population of poststarburst galaxies in cluster cores is expected from ram-pressure stripping given the resulting removal of disk gas, a possible compression of molecular clouds from the shock, and a subsequent rapid decline in star formation on the order of molecular cloud lifetimes. The SpARCS team has recently uncovered a correlation in the location of poststarbursts with phase-space, finding them preferentially in the middle phase-space bin with higher line-of-sight velocities (A. Muzzin et al., in preparation). In the work presented here, we have specifically selected galaxies with [OII] emission in order to expose environmental trends with star-forming galaxies. Therefore we are not likely to be probing a poststarburst population. However, we could be witnessing the intermediate galaxies during the delayed period sometime after ram-pressure stripping. Indeed, we measure their current level of star formation activity to be on par with recently accreted galaxies (i.e., not suppressed) and they have seemingly large reservoirs of dense molecular gas as traced by the high $113\,\mu$m rest-frame flux. Perhaps these are the progenitors of poststarburst galaxies before the rapid suppression of star formation. Some authors have even suggested that poststarbursts could be the descendants of e(a) galaxies: dusty starbursts with both moderate emission lines and strong Balmer absorption (e.g., Poggianti et al., 1999; Balogh et al., 2005; De Lucia et al., 2009). These galaxies are thought to contain a multi-phase dust distribution that obscures young OB stars in HII regions while leaving A stars relatively unaffected (Poggianti and Wu, 2000). Further elucidation of this hypothesis requires detailed examination of stacked spectra in phase-space bins; this analysis is currently in progress.

4.5 Conclusions

We have presented a *Herschel* study of star-forming galaxies in three $z \sim 1.2$ clusters from the SpARCS-GCLASS sample. We stack PACS (100 and 160 μm) and SPIRE (250, 350, and 500 μm) maps at the location of galaxies with [OII] emission—the star-forming population—binned by their location in $(r/r_{200}) \times (\Delta v/\sigma_v)$ phase-space. We utilize the bins determined in Noble et al. (2013b): $(r/r_{200}) \times (\Delta v/\sigma_v) < 0.1$ (low bin); $0.1 < (r/r_{200}) \times (\Delta v/\sigma_v) < 0.4$ (middle bin); and $(r/r_{200}) \times (\Delta v/\sigma_v) > 0.4$ (high bin). This isolates the earliest accreted cluster galaxies from galaxies that have completed at least one passage through the cluster, and those most recently accreted, respectively. We summarize our results as follows:

1. We fit the thermal portion of the stacked spectral energy distribution for each phase-space bin, deriving dust temperatures and integrated infrared luminosities from 100–500 μm in the observed frame, corresponding to 45–230 μm rest-frame. We do not detect the (stacked) lowest phase-space bin ($r \times \Delta v < 0.1$) in the 350 or 500 μm bands with SPIRE. After converting the luminosities to star formation rates, we find a constant specific star formation rate between the infalling and intermediate galaxies, and a ∼1 dex decline towards virialized galaxies in the core. This confirms the MIPS study of a $z = 0.871$ cluster presented in Chapter 3 (Noble et al., 2013b).

2. The dust temperatures of the lowest and highest phase-space bins are consistent with each other at ~50 K, while the middle bin $(0.1 < (r/r_{200}) \times (\Delta v/\sigma_v) < 0.4)$ possesses a lower temperature of ~30 K. This seems to be driven by a high flux at rest-frame 113 μm, which could be indicative of a large supply of dense molecular gas. The high f_{73}/f_{45} rest-frame ratio in this intermediate population also implies significant heating from a young population of stars. The low f_{73}/f_{45} rest-frame colour of the virialized population suggests a declining population of young stars, consistent with the lower specific star formation rate in this bin.

3. We propose a simple interpretation for quenching in which infalling galaxies undergo a constant gradual quenching from strangulation, and intermediate galaxies experience the more violent ram-pressure stripping, resulting in delayed, than rapid quenching. The virialized galaxies could be the by-product of a longer quenching timescale since we observe depressed activity in the cluster core. We speculate that intermediate galaxies with [OII] emission (which should contain a backsplash population) could be the progenitors of poststarbursts. We are currently observing them in the calm before the storm—a delayed period of passive evolution, while there is still ample molecular gas available to fuel star formation, and before rapid quenching commences.

We emphasize that this last conclusion is just a plausible quenching model to explain the observed trends in star formation activity and dust temperatures as a function of phase-space environment. An examination of stacked spectra and further observations of the gas components are crucial to verify this claim. As we will discuss in the thesis conclusions in Chapter 6, the Atacama Large Millimeter Telescope can provide CO 3–2 and CO 2–1 measurements at $z = 1.2$ that trace the densest molecular gas phase and total molecular gas reservoir, respectively.

5

A SUBMILLIMETRE-BRIGHT $z \sim 3$ OVERDENSITY

In this chapter, we present a wide-field (30′ diameter) 850μm SCUBA-2 map of the spectacular three-component merging supercluster, RCS 231953+00, at $z = 0.9$. The brightest submillimetre galaxy (SMG) in the field ($S_{850} \approx 12\,\mathrm{mJy}$) is within 30″ of one of the cluster cores (RCS 2319–C), and is likely to be a more distant, lensed galaxy. Interestingly, the wider field around RCS 2319-C reveals a local overdensity of SMGs, exceeding the average source density by a factor of 4.5, with a $< 1\%$ chance of being found in a random field. Utilizing *Herschel*-SPIRE observations, we find three of these SMGs have similar submillimetre colours. We fit their observed 250–850μm spectral energy distributions to estimate their redshift, yielding $2.5 < z < 3.5$, and calculate prodigious star formation rates (SFRs) ranging from $500-2500\,\mathrm{M}_\odot\,\mathrm{yr}^{-1}$. We speculate that these galaxies are either lensed SMGs, or signpost a physical structure at $z \approx 3$: a 'protocluster' inhabited by young galaxies in a rapid phase of growth, destined to form the core of a massive galaxy cluster by $z = 0$.

This work was originally published as:

"A submillimetre-bright $z \sim 3$ overdensity behind a $z \sim 1$ supercluster revealed by SCUBA-2 and *Herschel*"

Noble, A. G., Geach, J. E., van Engelen, A. J., Webb, T. M. A., Coppin, K. E. K., Delahaye, A., Gilbank, D. G., Gladders, M. D., Ivison, R. J., Omori, Y., Yee, H. K. C, 2013, MNRAS: *Letters*, 436, 40

We have expanded upon this document beyond the original five page *Letter* format in Noble et al. (2013a).

5.1 INTRODUCTION

Submillimetre (submm) surveys have a history of exciting revelations, beginning with the discovery of a population of submm-bright galaxies (SMGs) over a decade ago (Smail et al., 1997; Barger et al., 1998b; Hughes et al., 1998). These SMGs are now known to be high-z (Chapman et al., 2005; Wardlow et al., 2011), gas-rich (Frayer et al., 1998, 1999) systems undergoing intense episodes of star formation, and are the likely progenitors of massive elliptical galaxies seen locally (Eales et al., 1999; Lilly et al., 1999). Much of the insight gleaned from SMGs has been limited to a modest sample of detections, primarily over deep blank-fields (e.g., Coppin et al., 2006) or low-redshift cluster cores (e.g., Smail et al., 1997, 2002; Cowie et al., 2002; Knudsen et al., 2006, 2008). However, the latest generation of submm telescopes, namely the *Herschel Space Observatory* (Pilbratt et al., 2010) and SCUBA-2 (Holland et al., 2013) on the James Clerk Maxwell Telescope (JCMT), are ushering in a new era of submm astronomy, yielding samples of thousands of SMGs (Eales et al., 2010; Oliver et al., 2012) and promising many discoveries.

The first handful of results from the recently commissioned SCUBA-2 have just emerged: Chen et al. (2013) probed below the confusion limit in the first small (< 100 arcmin^2) SCUBA-2 map by exploiting a massive $z = 0.37$ cluster to magnify the faint background SMG population; Geach et al. (2013) presented a deep 450μm map of a blank-field and resolved 16% of the CIB; Casey et al. (2013) observed the same blank-field in the first wide-area SCUBA-2 map, and extracted 78 and 99 SMGs at 450μm and 850μm, respectively. While these studies have all demonstrated the great potential of SCUBA-2, a fundamental goal of the advanced camera has yet to be realized: the detection of rare SMGs in the early universe that trace the formation of protoclusters.

The wide-field mapping power of SCUBA-2 opens up a new parameter space in submm studies: the capability to survey volumes that sample the full range of galaxy environment at high redshifts. The densest regions—the nodes in the cosmic web—at all epochs are rare. However, it is essential to understand the evolution of galaxies within these environments if we are to link the growth of galaxies with the large scale structure they inhabit. Submm studies of distant 'protoclusters' are particularly promising since it is becoming clear that the massive tail of the galaxy cluster 'red-sequence' assembles quickly at $z > 2$ (Papovich et al., 2010), possibly via intense starbursts within gas-rich galaxies located in overdense (but potentially pre-virialised) structures at high-z (Daddi et al., 2009). This activity might well be heavily dust-obscured, requiring submm and/or infrared (IR) observations to detect.

Here, we report early findings from a wide-field SCUBA-2 and *Herschel*-SPIRE survey of a spectacular merging $z = 0.9$ supercluster, RCS 231953+00 (hereafter RCS 2319+00; Faloon et al., 2013). The structure comprises three massive ($\sim 5\times10^{14}\mathrm{M}_{\odot}$), X-ray bright galaxy clusters (Hicks et al., 2008), namely RCS 231953+0038.1, RCS 232003+0033.5, and RCS 231946+0030.6 (hereafter RCS 2319–A, RCS 2319–B, and RCS 2319–C). The three clusters are separated by less than 3 projected Mpc and are expected to merge to form a single Coma-mass cluster ($>10^{15}\mathrm{M}_{\odot}$) by $z \sim 0.5$ (Gilbank et al., 2008). RCS 2319–A is a known strong-lensing cluster (Gladders et al., 2003), and the three cores appear to be connected by filamentary structure and satellite groups. The wealth of data and discoveries surrounding RCS 2319–A is extensive (see Section 5.2.1); RCS 2319–C, on the other hand, has thus far been comparatively inconspicuous due to a lack of wide-field coverage encompassing the entire structure.

RCS 2319+00 is a progenitor of one of the most massive dark matter halos in the Universe, and affords a unique opportunity to study the physics of galaxy formation across the full range of galaxy environments at $z \approx 1$, as well as more distant galaxies lensed by the cluster potential. In this Letter, we present a serendipitous discovery of an overdensity of SMGs behind RCS 2319–C, as well as a bright SMG close to the cluster core. This overdensity could result from a large number of lensed SMGs behind the cluster or represent a possible distant protocluster. This discovery along the line-of-sight to the RCS 2319 supercluster is a fortunate coincidence: it allows us to investigate the properties of SMGs within the densest environments in the Universe at two epochs within the same field, with the benefit that the more distant structure might be partially lensed by the supercluster. We assume a ΛCDM cosmology with $(\Omega_m, \Omega_\Lambda, h) = (0.3, 0.7, 0.7)$.

5.2 OBSERVATIONS AND DATA REDUCTION

5.2.1 The RCS 2319+00 Supercluster

Originally discovered in the Red-sequence Cluster Survey (RCS-1; Gladders and Yee, 2005) and presented in Gilbank et al. (2008), the RCS 2319+00 structure now has extensive follow-up observations. Much of the work has focused on the northern-most cluster (RCS 2319–A). This cluster was revealed to be a remarkable strong-lensing cluster with three gravitationally lensed radial arcs (Gladders et al., 2003), and has a significant weak lensing signal as shown in the reconstructed mass map derived from *HST* imaging (Jee et al., 2011). SCUBA imaging of the core of RCS 2319–A unveiled a candidate lensed SMG (Noble et al., 2012) and *Herschel*-SPIRE imaging revealed a 2.5 Mpc filament of SMGs connecting RCS 2319–A to its eastern companion, RCS 2319–B (Coppin et al., 2012). This filament has been spectroscopically confirmed through a friends-of-friends analysis that utilized a comprehensive dataset of 302 confirmed cluster members and additional redshifts for 1961 galaxies over the entire supercluster field (Faloon et al., 2013).

5.2.2 850μm SCUBA–2 Observations

SCUBA-2 observations were conducted at the JCMT in Band 2 weather ($0.05 < \tau_{225\,\mathrm{GHz}} < 0.08$) over three nights between 17–21 September 2012. The 30′ PONG mapping pattern (Holland et al., 2013) is centred at $\alpha = 23^{\mathrm{h}}\ 19^{\mathrm{m}}\ 53.5^{\mathrm{s}}$, $\delta = 00^\circ\ 34'$

40.8″ J2000. The total mapping time was 7.75 hr, split into 11× 40 min scans. Individual scans are reduced using the dynamic iterative map-maker (*makemap*) of the SMURF package (Jenness et al., 2011; Chapin et al., 2013) following the procedure outlined in Geach et al. (2013). These scans are co-added in an optimal, noise-weighted manner, using the `MOSAIC_JCMT_IMAGES` recipe in the PICARD environment. Finally, to improve the detectability of faint point sources, we use `SCUBA2_MATCHED_FILTER`, which removes large angular scale varying pattern noise in the map by smoothing with a 30" Gaussian kernel, subtracting this, and then convolving the map with the 850μm beam. The average exposure time over the 'nominal' 30′ mapping region in the co-added map is ≈10 ksec, reaching a central depth of 1.5 mJy (see Figure 5.1).

5.2.3 *Herschel*-SPIRE Observations

The *Herschel*-SPIRE (Griffin et al., 2010) data were taken on January 2, 2013, with a total of 8.1 hours of integration time over five dithered maps at 250, 350, and 500μm (OBSIDs 1342258348, 1342258349, 1342258350, 1342258351, 1342258352). The observations were designed to cover the three cluster components over $30' \times 30'$, and were carried out in array mode using the nominal scan speed.

Each map is reprocessed individually using HIPE V10.0 (Ott, 2010) and the latest calibration tree. One map has significant artifacts and requires a linear polynomial fit during the destriping process; all other maps are destriped using a zeroth-order fit. All Level 1 scans are merged and final mosaiced images created using the naïve mapper with default pixel sizes of 6″, 10″, and 14″, at 250, 350, and 500μm, respectively (Figure 5.2).

Point sources are extracted using SUSSEXtractor (Savage and Oliver, 2007) at a relatively low detection threshold of 3.5σ to maximize counterpart completeness. The source list is passed to a timeline fitter that utilizes the merged Level 1 timeline data to fit a Gaussian at the source position. For sources below 30 mJy, the flux is measured

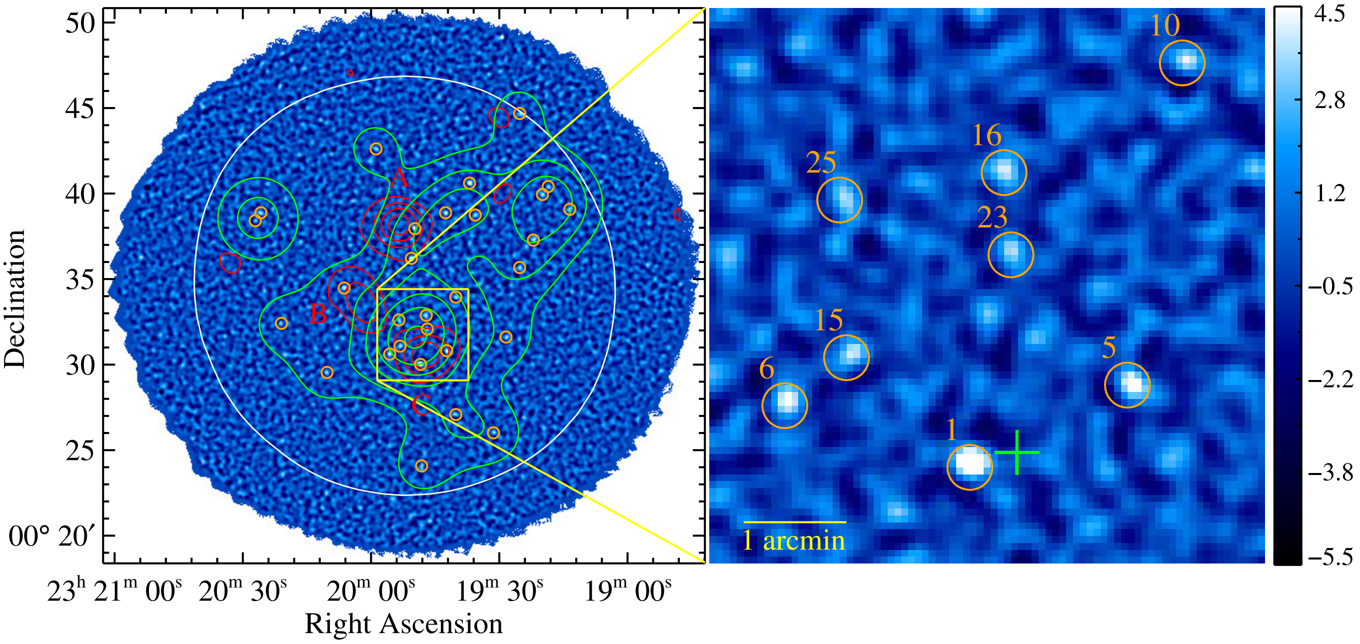

Figure 5.1 Left: 850μm signal-to-noise ratio map of the RCS 2319+00 supercluster overlaid with the red-sequence contours indicating the cluster positions in red. We highlight all SMGs detected at $>3.5\sigma$ in the 850μm map with orange circles. The green contours show the fractional overdensity of SMGs compared to the average density over the field, starting at $\delta = -0.3$ and increasing by levels of 0.7. The white circle represents the region from which sources are extracted. Right: a zoom-in on the overdensity of SMGs surrounding RCS 2319–C, labeled with their ID in the 850μm catalog. Given its proximity to the centre of RCS 2319–C (the BCG is marked by the green cross), the brightest source in the catalog, SMM J2319.1, is possibly lensed by the cluster potential.

as the peak on the image after smoothing with a convolution kernel and using a subpixel correction factor. This has been found to be a more reliable flux estimate for faint sources (SPIRE Webinar, private communication). The uncertainties on the fluxes are estimated from pixel noise added in quadrature with a nominal confusion noise of 5.8, 6.3, and 6.8 mJy at 250, 350, and 500μm, respectively (Nguyen et al., 2010).

5.3 Analysis and Results

Point sources are extracted from the central $\sim 25'$ of the beam-convolved signal-to-noise ratio map, where the sensitivity is fairly uniform and the noise is $< 3\times$ the central 1σ r.m.s., corresponding to a total uniform area of $\sim$473 arcmin^2. We detect 29 point sources at 850μm at a significance of $>3.5\sigma$, 16 of which are at $> 4\sigma$. The detections are indicated by orange circles in Figure 5.1 and named in order of descending signal-to-noise ratio. We quantify the false-detection rate by running the detection algorithm on jack-knife versions of the map (details given in Geach et al., 2013). Within the source detection area, we find a false-detection rate of 4.5% (20%) at 4.0σ (3.5σ). We note that both these rates are 25% lower where the noise is $< 2\times$ the central r.m.s., encompassing all but one of the SMGs. In Figure 5.3, we plot the 850μm differential source counts and find them consistent with those from a blank-field, the SCUBA HAlf Degree Extragalactic Survey (SHADES; Coppin et al., 2006).

5.3.1 SCUBA–2/SPIRE Source Identification

Continuum radio imaging at 1.4 GHz covers the entirety of the SCUBA-2 and SPIRE observations, although with roughly 2× the noise at the edges due to primary beam attenuation. It derives from 16 hours of integration time on the National Radio Astronomy Observatory's Very Large Array, and has previously been described in Noble et al. (2012). We also exploit deep IR imaging from the Multiband Imag-

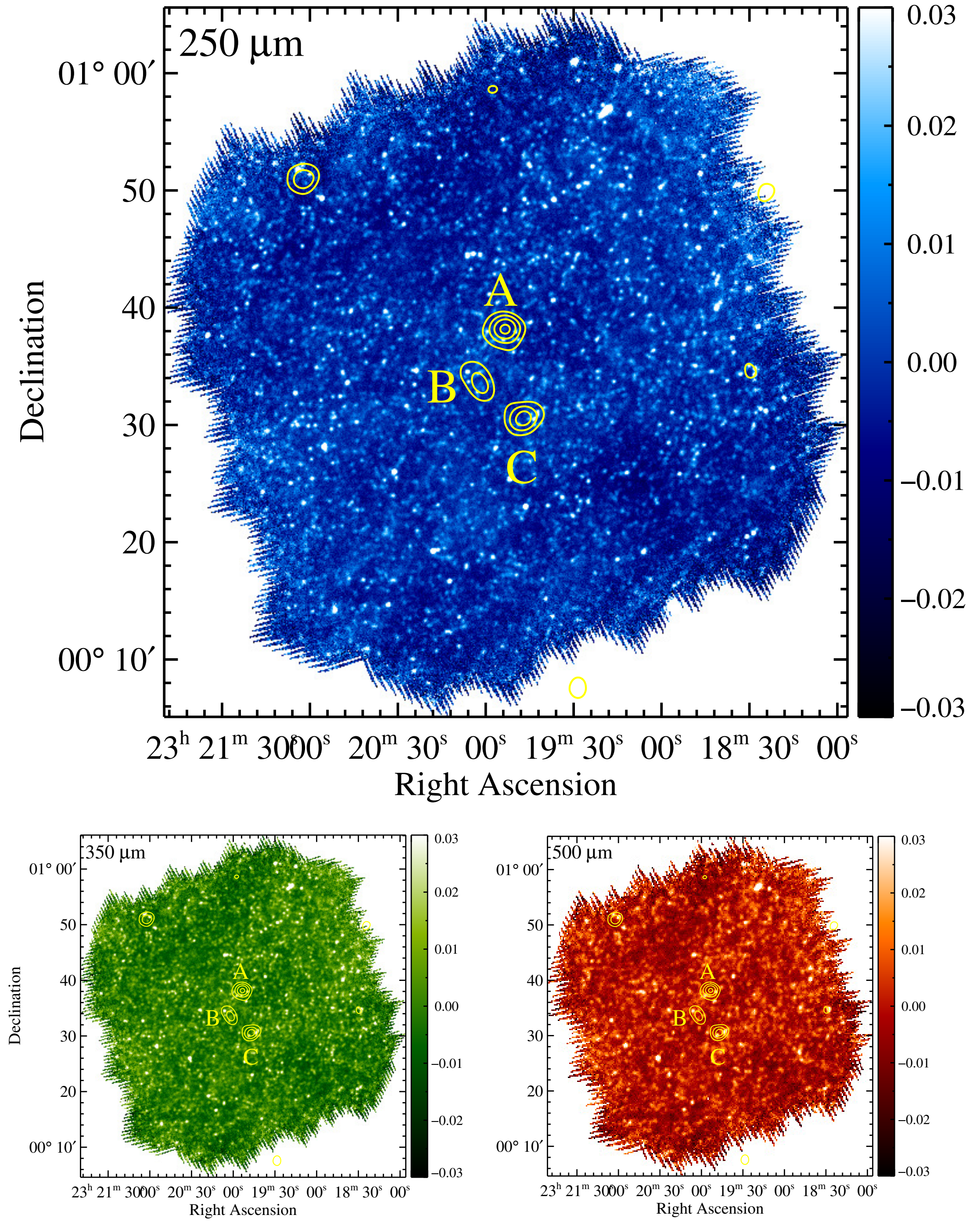

Figure 5.2 *Herschel*-SPIRE maps of the RCS 2319 cluster field at 250 (blue), 350 (green), and 500μm(red). The red-sequence contours are overlaid in yellow to illustrate the three cluster components.

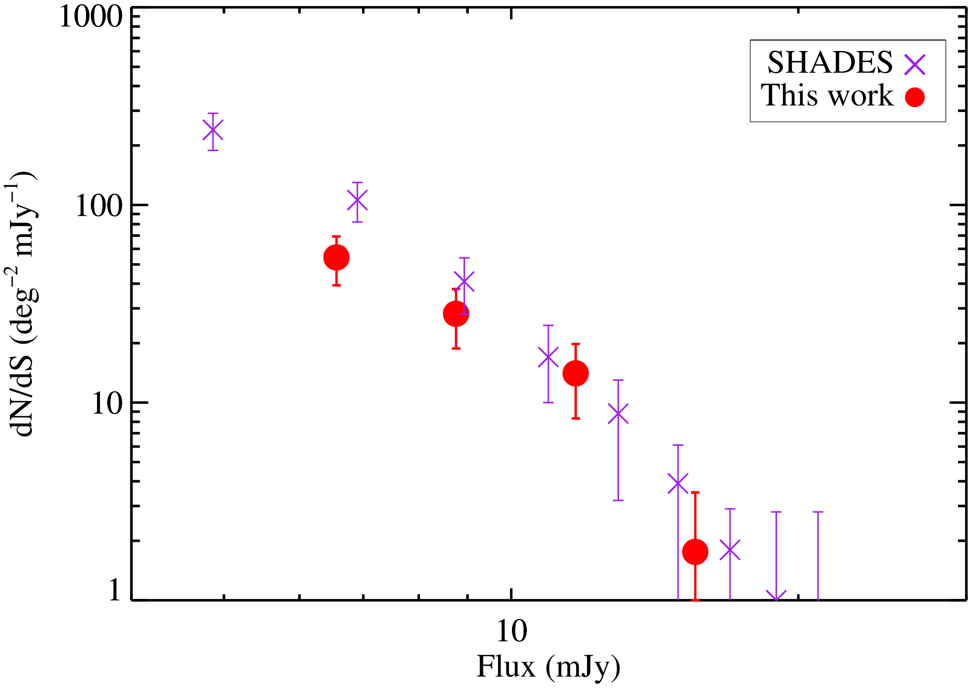

Figure 5.3 Differential source counts at 850μm within the RCS 2319 cluster field for all 3.5σ detected SMGs (red circles). The error bars are standard Poisson uncertainties. The source counts from SHADES (purple X) are plotted as a consistency check.

ing Photometer (MIPS) aboard *Spitzer* which are explained in detail in Webb et al. (2013). The extensive, multi-wavelength counterpart identification process, including the completeness and false-detection rate, will be presented in Noble et al. (in preparation); we provide only a brief description in this communication, as we are primarily interested in the sources around RCS 2319–C.

Given the ≈15″ beam at 850μm, we search for radio and 24μm emission within 10″ of the SCUBA-2 positions, ensuring we detect all possible counterparts (Ivison et al., 2007; Biggs et al., 2011). While a 10″ search radius is generous, in practice we find that all the counterparts to >4σ SMGs are within 6″, with an average offset of 3″. We robustly detect a 24μm and/or radio counterpart for 20 of the 29 (70%) sources within our catalog. Of the remaining SCUBA-2 detections, eight lack MIPS coverage (and have no radio detection), and one source eludes any counterpart emission. For cases where multiple 24μm sources are detected within the search area (and no radio emission), we assign the nearest source as the most likely counterpart, which in all $< 4\sigma$ occurrences is also the brightest 24μm detection within the search area.

Counterpart SPIRE emission can further verify the validity of each SCUBA-2 source, although it is not a requirement as 20–60% of $z > 2$ SMGs are undetectable with SPIRE (Casey et al., 2012). Given the large SPIRE beam, we search within the entire SCUBA-2 beam for 250–500μm emission, resulting in detections in one or more SPIRE bands for 18 of the 29 850μm sources. Four of the SMGs lacking MIPS coverage or a radio counterpart are detected with SPIRE, yielding a final catalog of 24 (80%) SCUBA-2 sources with counterparts in another band. Any emission that is blended or confused in SPIRE is omitted from the counterpart catalog for the purposes of far-IR SED fitting (see §5.3.2). Postage stamps of $36'' \times 36''$ are shown in Figures 5.4 and 5.5 to illustrate the counterpart identification process for the eight SMGs in the overdensity around RCS 2319–C (see Section 5.3.2.

5.3.2 Evidence of a Line-of-sight, Submillimetre-bright Protocluster

The 30′ SCUBA–2 and SPIRE maps are large enough to enable us to examine the spatial distribution of submm galaxies. The average surface density of 850μm sources across the 30′ RCS 2319+00 field is consistent with that expected from the number counts measured in blank-field submm surveys (Coppin et al., 2006); however, it is clear that there are large variations in the local surface density on scales of several arcminutes. Indeed, there appears to be a local relative overdensity of 850μm detections in the vicinity of RCS 2319–C. To quantify this, we create a Gaussian smoothed ($\theta = 4'$) surface density map, normalized to the fractional overdensity of SMGs: $\delta_{\rm peak} = (\rho - \bar{\rho})/\bar{\rho}$, where ρ and $\bar{\rho}$ are the local and mean galaxy density (Figure 5.1).

There is a $\delta_{\rm peak} = 3.5$ close to RCS 2319–C. Although clearly this is a local maxi-

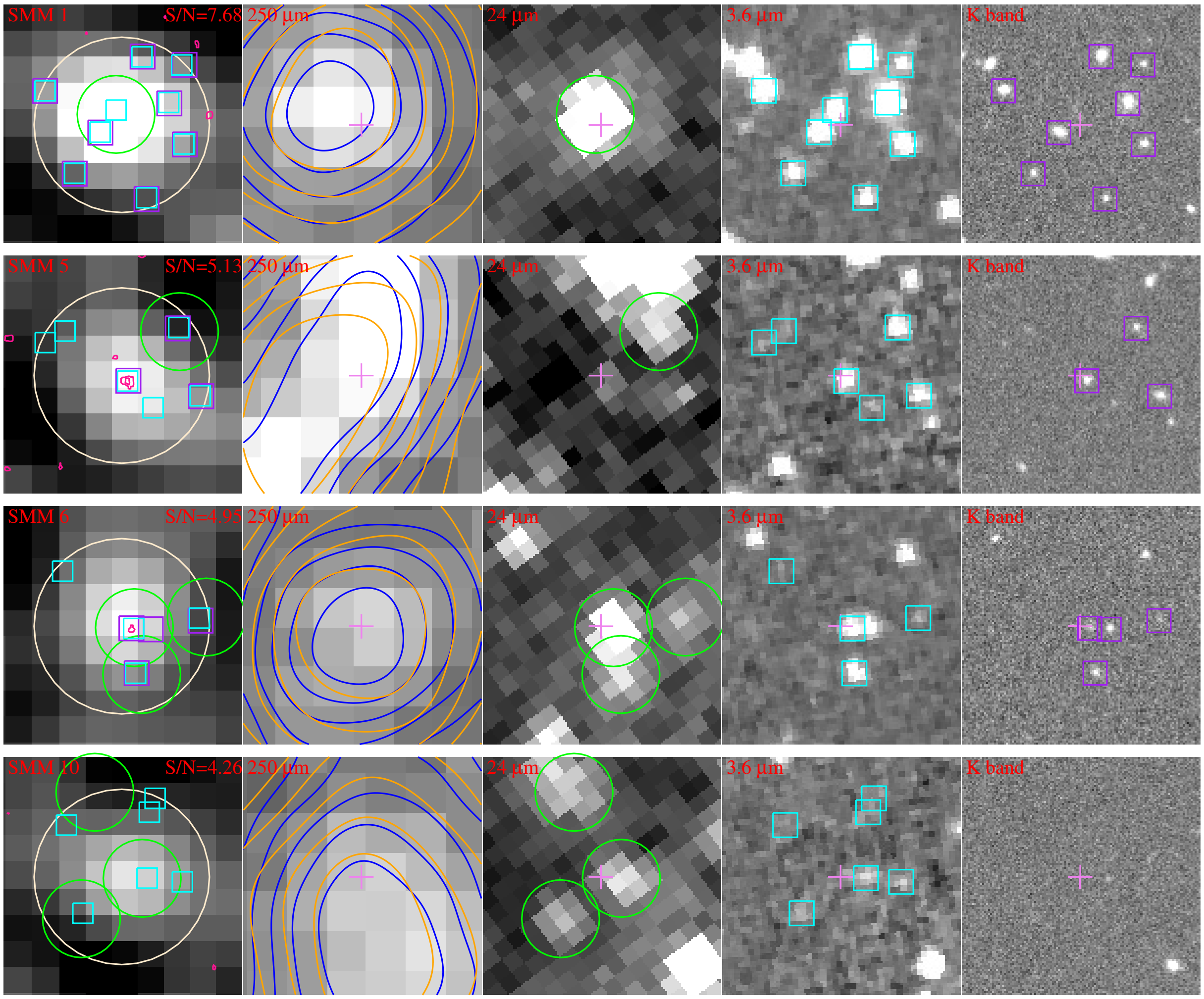

Figure 5.4 Postage stamps of 36″ × 36″ for the four SMGs detected with the highest significance in the overdensity centered on RCS 2319–C. The gray scales correspond to 850 μm, 250 μm, 24 μm, 3.6 μm, and 2.2 μm, from left to right. The white circles represent the 10″ search radius used to identify likely counterpart emission to each SMG. The pink contours on the 850 μm image represent 1.4 GHz detections from the radio map, starting at 45 μJy and increasing by levels of 20 μJy. Overlaid on the 250 μm image are 350 μm and 500 μm contours in blue and orange, respectively. The levels of the contours differ between each image, but are shown to illustrate the increased level of blending and confusion at longer wavelengths, especially for the lower signal-to-noise sources. The green circles represent 24 μm detections with the 6″ radius signifying the MIPS point spread function. The cyan (purple) squares correspond to detections at 3.6 μm (2.2 μm), and have a 2″ radius. These last two wavelengths (3.6 and 2.2 μm) are not used in the counterpart identification process but are shown for completeness. The pink cross in all images marks the position of the SMG.

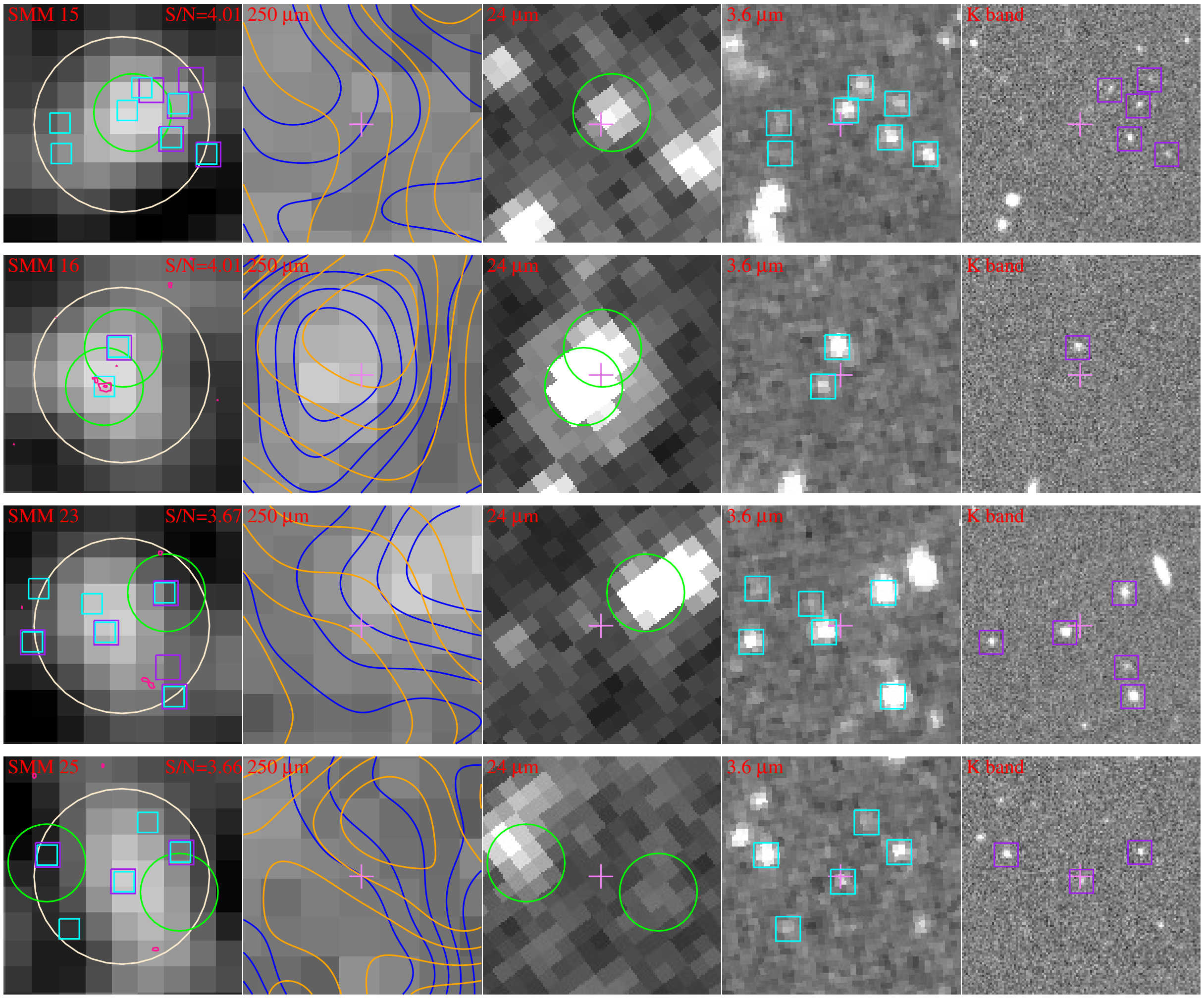

Figure 5.5 Postage stamps for the four remaining SMGs within the overdensity. The symbols are the same as Figure 5.4.

mum of the SMG density within our (still relatively small) field, how significant is it? To address this, we generate 1000 simulated catalogues of the same size as the real map, and with the same source density as the detected SMGs. In addition to the shot noise properties of the sources, we also include the effects of clustering on linear scales, assuming a redshift distribution from (Chapman et al., 2005) and bias factor matching the current best estimate for 850μm-selected SMGs (Hickox et al., 2012). We check the clustering properties of the fake catalogues by applying the Landy-Szalay estimator (Landy and Szalay, 1993), which counts the number of galaxy-galaxy (DD), random-random (RR), and galaxy-random (DR) pairs at various angular scales:

$$w(\theta) = \frac{DD - 2DR + RR}{RR}. \tag{5.1}$$

In Figure 5.6, we find the angular correlation function $w(\theta)$ from our simulated catalogs (red circles) to be consistent with the linear bias from Hickox et al. (2012) at $\theta \gtrsim 1'$, matching the scale of the candidate protocluster. We expect the roll-off at low angular scales where the one-halo term dominates since our dark matter density fields only included the two-halo term given we were interested in clustering on larger scales.

From each independent catalogue realisation, we evaluate the convolved surface density estimate, as described above. The total number of density peaks found with $\delta \geqslant \delta_{\mathrm{peak}}$ is an estimate of the significance of finding a local overdensity of magnitude 3.5 or greater in our map. We find nine such peaks over all 1000 realisations, meaning the SMG overdensity is very unlikely to be due to Poisson noise or clustering from large scale structure, significant at a level of 99%. In other words, such a structure is rare, even given the known correlation function of SMGs, and thus could point to the presence of a real physical association of SMGs tracing a highly biased structure. In Figure 5.7, we show the fractional over density for the real map compared to two examples in the simulated catalogs: one of the nine cases where we find a $\delta_{\mathrm{peak}} \geqslant 3.5$ and one case with no such peak.

With four submm bands, we can also compare the submm colours of the SMGs around RCS 2319–C to test if they have similar far-IR SEDs (and therefore possibly similar redshifts) in addition to a spatial correlation. In Figure 5.8, we plot the SPIRE and SCUBA-2 colours of 11 SMGs that are detected in all three SPIRE bands. We do not include 8 sources that have blended SPIRE emission. The sources within the

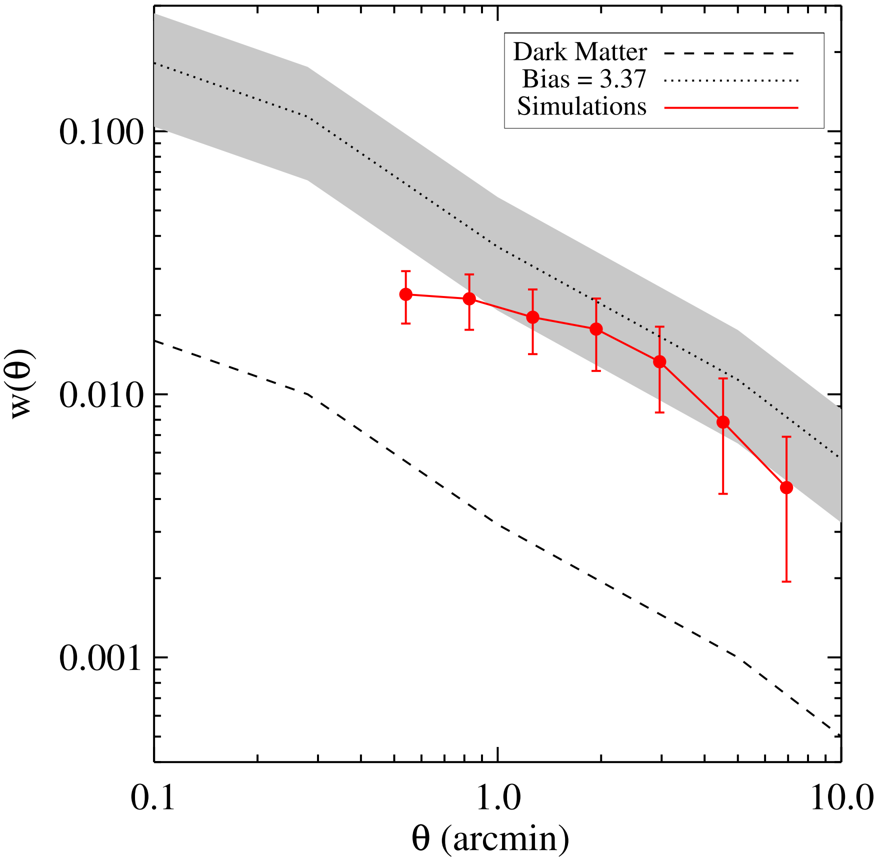

Figure 5.6 The angular autocorrelation function for SMGs with a linear bias of 3.37 ± 0.82 (solid gray band) as derived in Hickox et al. (2012). Also shown is the dark matter correlation function (dashed line). We compute the Landy-Szalay estimator in our simulated dark matter density field with an input bias of 3.37 to check the clustering is consistent with that of SMGs from Hickox et al. (2012).

overdensity are highlighted in pink, and lie at the higher redshift end of the colour distribution compared to the other SMGs in the field. SMM J2319.1 and SMM J2319.6 are quite distinct, while SMM J2319.16 tends towards the bluer end of the S_{250}/S_{350} distribution, but is still within $\sim 1\sigma$ of the other putative protocluster galaxies.

We estimate the redshifts of these sources by fitting to the submm photometry, assuming the SED can be modeled by a single temperature modified blackbody, with a

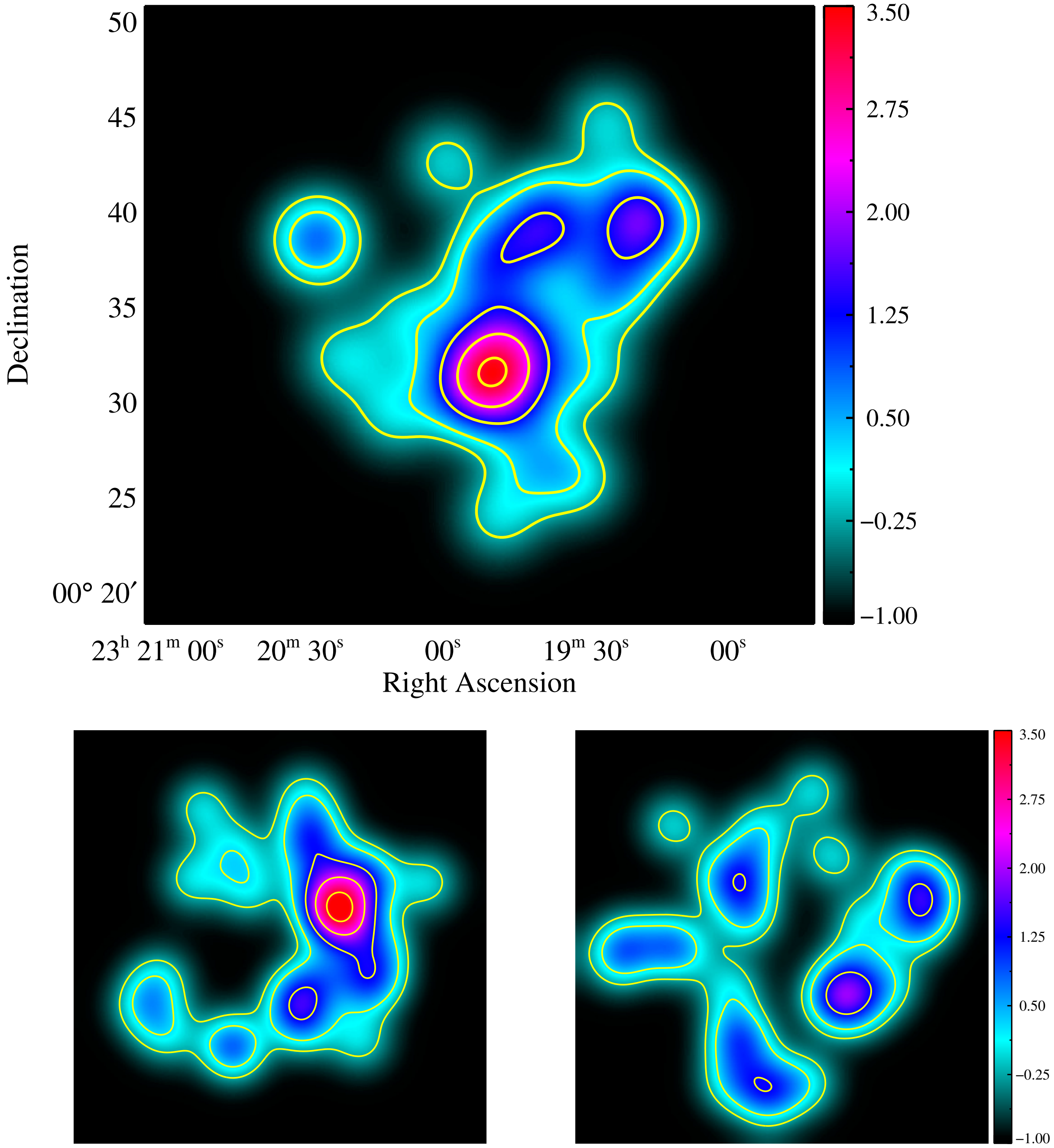

Figure 5.7 The surface density map showing the fractional over density of SMGs in the real map (top panel), and for two of the 1000 realisations of simulated clustered catalogs (bottom panel). The left map illustrates a case where the simulations produce a peak of $\geqslant 3.5$ ($< 1\%$ of the time), while the right map demonstrates the remainning 99% of the catalogs that show less clustering than the real map. The contours shows fractional over density levels starting at -0.25 and increasing by 1.0.

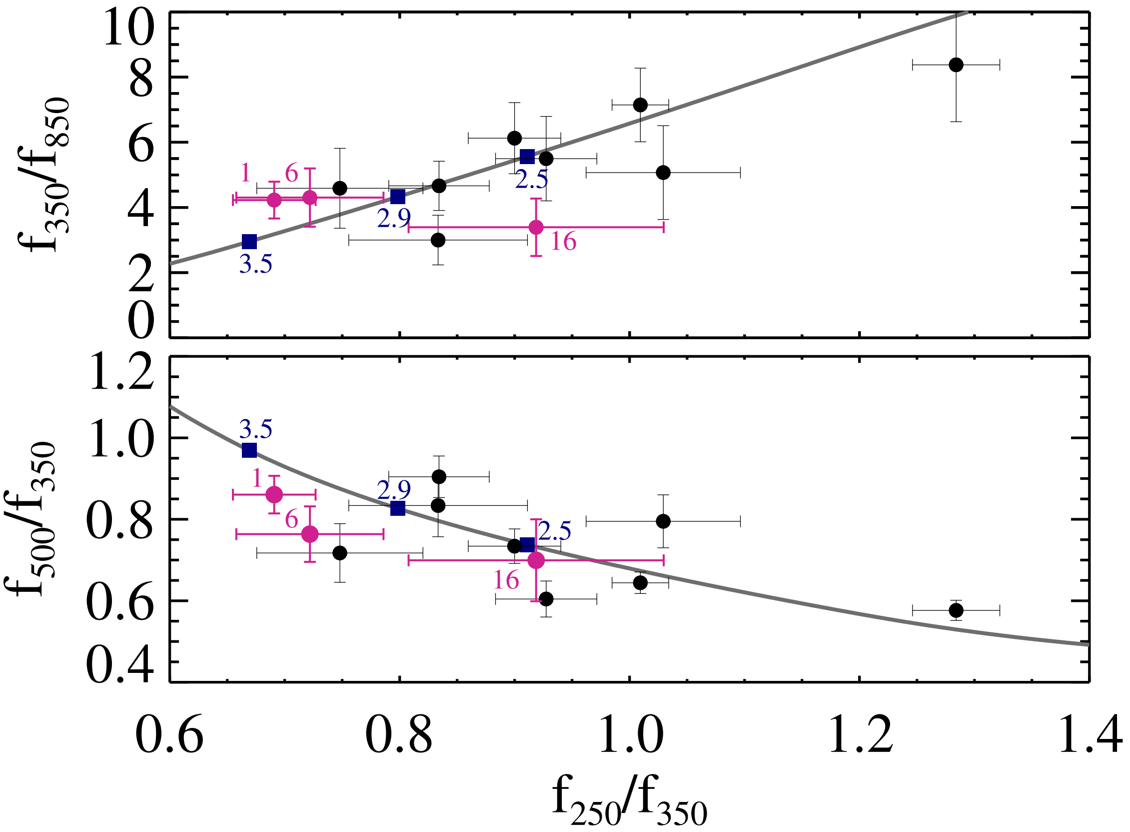

Figure 5.8 Submm/far-IR colour ratios for all SMGs that have unblended SPIRE counterpart emission in the top panel, and solely SPIRE colours in the bottom panel. Both plots show the change of these colour ratios (gray line) with redshift using the median luminosity template from Chary and Elbaz (2001), where the navy squares denote $z = 2.5, 2.9, 3.5$. The possible protocluster members are highlighted in pink, and are at the higher-z end of the distribution with similar far-IR/submm colours. Confusion errors are not shown for clarity.

smooth transition into a power law ($S_\nu \propto \nu^{-2}$) on the Wien side, where $\mathrm{dlog}S_\nu/\mathrm{dlog}\nu \leqslant -2$. Because of the degeneracy in the z–T–β parameter space, we perform three fits, each time only allowing z and T to be free parameters ($20 < T < 60\,\mathrm{K}$), while fixing β at 1.5, 1.75 and 2, spanning the likely range of real galaxies (Dunne et al., 2000).

We further improve upon the estimate by putting prior constraints on z and T from independent measurements, as shown in Roseboom et al. (2012). We estimate a submm-radio photo-z using the spectral index relation from Carilli and Yun (1999):

$$\log(1+z) = \frac{-0.24 - \alpha^{850\mu\mathrm{m}}_{1.4_{\mathrm{GHz}}}}{0.42 \times (\alpha_{\mathrm{radio}} - \alpha_{\mathrm{submm}})} \tag{5.2}$$

assuming $\alpha_{1.4\mathrm{GHz}} = -0.8$ (Ibar et al., 2008), $\alpha_{850\mu m} = \beta + 2$, and a typical uncertainty of $\Delta z = 1.0$ (Aretxaga et al., 2007). We compute $\alpha^{850\mu\mathrm{m}}_{1.4_{\mathrm{GHz}}}$ from the ratio of the observed flux densities:

$$\alpha^{850\mu\mathrm{m}}_{1.4_{\mathrm{GHz}}} = \frac{\log(S_{850\mu\mathrm{m}}/S_{1.4\mathrm{GHz}})}{\log(\nu_{850\mu\mathrm{m}}/\nu_{1.4_{\mathrm{GHz}}})}. \tag{5.3}$$

We also simultaneously measure the total rest-frame IR luminosity to estimate S_{60}/S_{100} using the empirical relation in Chapman et al. (2003):

$$\log\left(\frac{S_{60\mu\mathrm{m}}}{S_{100\mu\mathrm{m}}}\right) = \log C_\star + \delta \log\left(1 + \frac{L_\star}{L_{\mathrm{TIR}}}\right) + \gamma \log\left(1 + \frac{L_{\mathrm{TIR}}}{L_\star}\right). \tag{5.4}$$

We adapt the fit values from a SPIRE-selected sample from Roseboom et al. (2012) with $C_\star = 0.45$, $\delta = -0.02$, $L_\star = 5 \times 10^{10}\mathrm{L}_\odot$, and $\gamma = 0.16$. We then convert the flux ratio into a dust temperature from the modified blackbody described above and conservatively assume a 10 K scatter in T_d.

This fitting algorithm greatly reduces the degeneracy between z and T_d and produces typical uncertainties of $\Delta z = 0.6$ and $\Delta T_d = 8\,\mathrm{K}$. The best fit SEDs are shown in Figure 5.9. The lowest values of χ^2/ν yield $z =$[3.5, 2.9, 2.5] and $T_d =$[48, 43, 41] K for SMMs J2319.1, J2319.6, and 2319.16, respectively. These redshifts are all within $\sim 1\sigma$ and further support the existence of an SMG protocluster behind RCS2319-C at $z > 2.5$. Although this redshift range is representative of the typical SMG (Chapman et al., 2005), we emphasize the similarity of submm colours for these SMGs, which isolates them from the rest of the sample through a consistent comparison. The SED fit also provides an estimate of the IR luminosity which can be converted to a SFR (Salpeter IMF; Kennicutt, 1998a); we find all three candidate protocluster members are highly active, with SFRs of 2500, 1100, and 500 $\mathrm{M_{\odot}\,yr^{-1}}$(assuming no AGN contamination). We note that these could be over estimated if any of the SMGs are strongly lensed.

5.3.3 A Submillimetre-bright, Strongly Lensed Galaxy

Within this putative protocluster lies the brightest 850μm source in the catalogue, SMM J2319.1, with $S_{850} = 12.05 \pm 1.56\,\mathrm{mJy}$. This source is only 28$''$ away from the X-ray peak of RCS2319–C ($L_X = 3.6^{+0.6}_{-0.4}\,\mathrm{erg\,s^{-1}}$; Hicks et al., 2008), and could be strongly lensed by the cluster potential, though it is only 1.5× as bright as the second brightest protocluster member. SMM J2319.1 is coincident with an extremely red spur-like feature—possibly the optical/near-IR counterpart to the SMG. It is considerably redder than the red-sequence galaxies in the cluster, implying that it is probably at higher redshift. Indeed, the SED fit places this source at $z = 3.5$, although (sub)mm spectroscopic identification will be required to accurately determine the redshift. SMM J2319.1 might have its flux and projected size boosted by lensing – it is thus an excellent target for detailed, high signal-to-noise follow-up in the (sub)mm-cm regime which can reveal a wealth of information on the physical conditions within distant galaxies (e.g., Cox et al., 2011; Omont et al., 2011; Fu et al., 2012; Vieira et al., 2013).

In Figure 5.10 we present a $gK[4.5]$ composite image of the cluster core. 850μm S/N contours mark the position of the galaxy. There are hints of a blue arc-like feature around the BCG, indicating that this may be a strong lensing cluster. We lack an accurate mass model for this cluster (high-resolution optical imaging only exists for RCS 2319–A), but assuming an isothermal sphere with $\sigma_v = 759\,\mathrm{km\,s^{-1}}$ (Faloon et al., 2013) and $z = 3.0$ for the source plane, we calculate an Einstein radius of $\sim 9''$, which is consistent with the distance between the BCG and blue arc. We emphasize that the projected overdensity of SMGs around RCS2319–C could also be due to

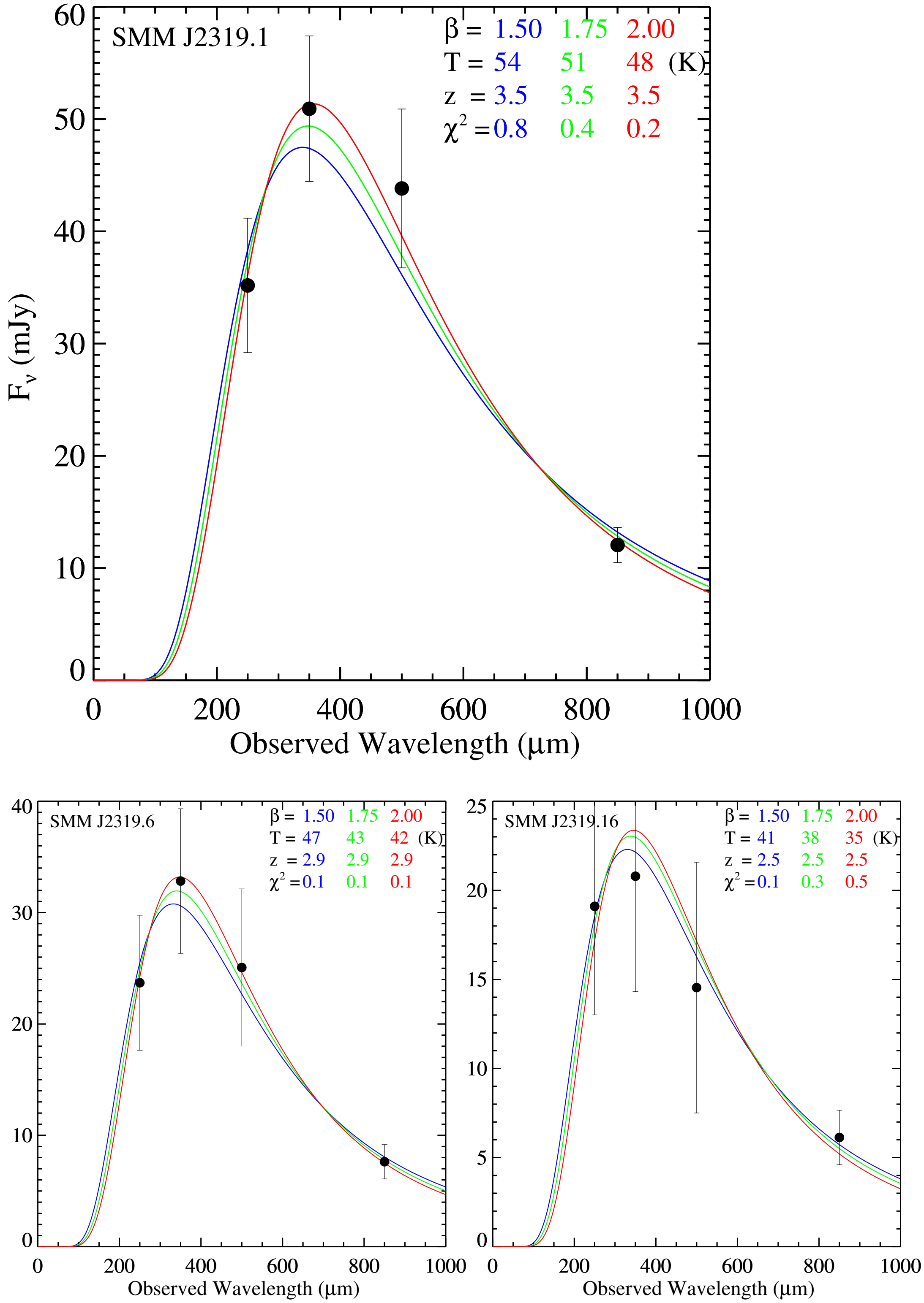

Figure 5.9 Modified blackbody fits to the SPIRE and SCUBA-2 fluxes for the three possible protocluster members, using the technique described in Section 5.3.2. The parameters for the best fit values with β fixed at 1.5 (blue), 1.75 (green) and 2.0 (red) are listed in each panel. The lowest reduced χ^2 values are given by $z = [3.5, 2.9, 2.5] \pm 0.6$ and $T_{\rm d} = [48, 43, 41] \pm 8$ K for SMMs J2319.1, 2319.6, and 2319.16, respectively. We note that SMM J2319.1 has only a weak radio detection, just below the catalogue limit; we therefore assign it the 3σ rms limit of 45μJy.

boosted counts from lensing of the random field, rather than a physical protocluster (spectroscopic confirmation will answer this question). However, the peak of the overdensity is offset from the core of RCS 2319–C by $>1'$, while the average lensing magnification beyond the central $30''$ is expected to be < 2 for similarly massive clusters (Noble et al., 2012).

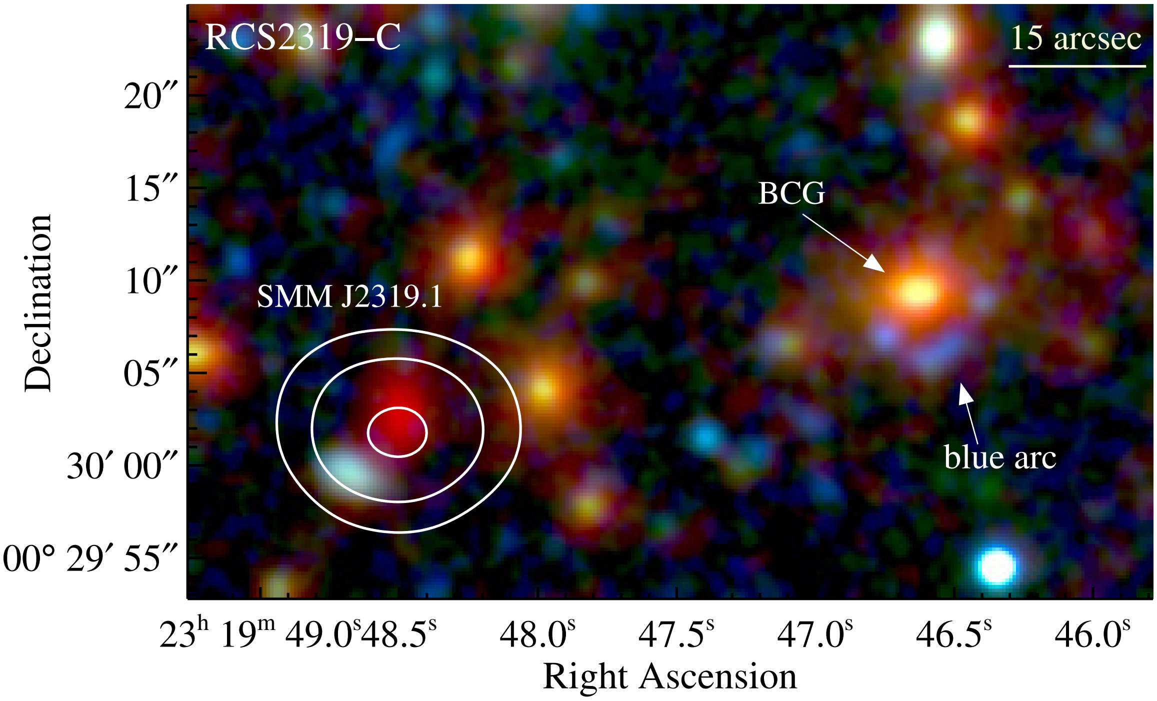

Figure 5.10 A gK[4.5] colour composite (from CFHT and IRAC) of the centre of RCS 2319–C, showing the position of with SMM J2319.1, the possible lensed SMG (850μm S/N contours starting at 5σ, increasing by levels of 1σ), Note the very red optical/near-IR emission coincident with the SCUBA-2 detection. We highlight the BCG, with a blue arc-like feature to the south, further indicating that this could be a strong-lensing cluster.

5.4 SUMMARY

This Letter presents the first wide-field SCUBA-2 850μm map of a high-z galaxy cluster field. We target a rare, three-component supercluster at $z = 0.9$ – RCS 2319+00 – detecting 29 SMGs, the majority of which have robust counterparts at 24μm, 1.4 GHz and/or in the *Herschel*-SPIRE bands. Previous work on RCS 2319+00 has focused on the northern core, RCS 2319–A, which is a well-known strong-lensing system, whereas the new SCUBA–2 map reveals that RCS2319–C, the southern-most component, also has some interesting traits. We make two discoveries:

1. RCS2319–C has features indicative of a strongly lensing cluster, with a distinct blue arc just below the BCG (at a radius consistent with the Einstein radius expected for this cluster). We report the discovery of a bright ($S_{850} \approx 12\,\mathrm{mJy}$) SMG 28″ from the core, associated with a very red optical/near-IR counterpart that is likely to be a lensed galaxy at $z \approx 3$. Thus, it offers the rare opportunity to study the properties of the SMG in much finer detail than would otherwise be possible.

2. There is a significant local overdensity of SMGs in the vicinity of RCS2319–C, with a peak of $\delta = 3.5$ in density contrast when smoothed at $4'$. Simulations indicate that there is a <1% chance of finding a similar structure in a (clustered) blank field of the same area. We estimate the redshifts for three of the sources within this overdensity by fitting the observed 250–850μm photometry with a modified blackbody SED, finding them consistent with $2.5 < z < 3.5$. They have high IR luminosities, corresponding to SFRs ranging from $500 - 2500\,\mathrm{M}_{\odot}\,\mathrm{yr}^{-1}$. We speculate that the SMGs are part of a physical association at $z \approx 3$, perhaps signposting a starbursting protocluster along the line of sight to RCS 2319–C. This scenario is supported by recent clustering measurements which predict the formation of SMGs in compact protoclusters

(Maddox et al., 2010). Indeed, SMGs have been found to trace the underlying distribution of Lyman-α emitters in a $z \approx 3.1$ protocluster (Tamura et al., 2009) and in some cases are physically associated with Lyα Blobs in these enviroments (Chapman et al., 2001; Geach et al., 2005).

6

CONCLUSIONS

6.1 SUMMARY

In this thesis we have studied multiple aspects of galaxy evolution within cluster environments through several observational windows in the infrared and submillimetre regimes. We are currently in a golden age of rich observations at these wavebands, enabled by the advent of cutting edge instruments and facilities, including those used in this work: *Spitzer*, *Herschel*, and SCUBA-2. As discussed in Chapter 1, observations from 1–1000 μm are providing critical new insight into the evolution of galaxy properties, tracing star formation activity that is otherwise obscured at ultraviolet and optical wavelengths. Infrared and submillimetre observations are of particular importance at high redshift ($z > 1$) where the peak epoch of star formation in the Universe occurs, and luminous infrared galaxies dominate the energy budget.

Understanding the influence of environment represents a fundamental goal in studies of galaxy formation and evolution, and galaxy clusters offer ideal laboratories with which to examine environmental effects on their constituent members. In a Universe governed by hierarchical structure formation, clusters continually evolve and build up mass through the accumulation of galaxies and groups. As such, various accretion histories for galaxies within clusters likely result in differing interactions with the intracluster medium. A suitable definition of environment must therefore account for the various phases of galaxy accretion, and is crucial in order to accurately assess environmental significance on galaxy evolution.

A dynamical definition for environment based on the phase space of line-of-sight velocity and clustercentric radius offers a unique snapshot of distinct galaxy populations that are accreted throughout the cluster's lifetime. It therefore provides a sampling of environmental interactions with homogenous populations, probing the time-averaged density to which a galaxy has been exposed. We introduced this "caustic" definition of environment in Chapter 3 (Noble et al., 2013b), highlighting its utility for isolating infalling galaxies from those that were accreted at the earliest stages of cluster formation (or even formed in situ). Conventional definitions of environment—nearest neighbor density or clustercentric radius—have high levels of contamination from recently accreted objects that appear to be in the cluster core due to projection. Assuming infalling galaxies still retain a nominal level of star formation, and are not yet affected by the cluster environment, projection-induced contamination can artificially boost estimates of the specific star formation rate in the cluster core. With a stellar mass-limited sample of *Spitzer*-MIPS 24 μm star-forming galaxies, we identified trends in stellar age and specific star formation as a function of caustic environment, $r/r_{200} \times \Delta v/\sigma_v$ in a $z = 0.871$ cluster, thereby isolating distinct galaxy populations which are more likely to have homogenous properties. This results in a 0.9 dex decline of specific star formation in the earliest accreted galaxies within the cluster core, contrary to the flat trend that results from conventional probes of environment.

We extended this caustic analysis to a larger sample of three $z = 1.2$ clusters in Chapter 4 with *Herschel*-PACS and -SPIRE data. Observations from 100 to 500 μm straddle the peak of the thermal portion of the spectral energy distribution, facilitating accurate estimates of the infrared luminosity. We stacked the *Herschel* maps at the locations of galaxies with [OII] emission, which is indicative of ongoing star formation, and divided the sample into the three phase-space bins determined from Chapter 3. From the spectral energy distribution of each stack, we derived dust temperatures, infrared luminosities, and specific star formation rates. Once again, an order of magnitude depression in specific star formation rate with descending phase-space bin was revealed, confirming the results from Noble et al. (2013b). We also investigated the dust temperatures as a function of environment, finding the intermediate population to have a significant drop in temperature ($28 \pm 4.3\,\mathrm{K}$) compared to the recently accreted population ($48 \pm 4.5\,\mathrm{K}$), and to a lesser extent compared to the virialized galaxies which have a large dust temperature uncertainty ($53 \pm 12\,\mathrm{K}$). We presented a plausible interpretation for quenching mechanisms, suggesting that ram-pressure stripping acts on the intermediate population, while gradual strangulation results in reduced star formation rates for the virialized population.

Chapter 5 presented a study of a $z \sim 0.9$ three-component merging supercluster using SCUBA-2 ($850\,\mu$m) on the JCMT and *Herschel-SPIRE* (250, 350, and $500\,\mu$m) data. We serendipitously discovered an overdensity of submillimetre-bright galaxies which exceed the average source density in the field by a factor of 4.5. From the far-infrared to submillimetre photometry, we derived the best-fit spectral energy distributions to estimate dust temperatures and redshifts. The overdensity is consistent with a background population at $z \simeq 3$ and has significant star formation activity, ranging from 500–$2500\,\mathrm{M}_\odot\,\mathrm{yr}^{-1}$. Given a $< 1\%$ chance of randomly finding such a strong density, even after accounting for the inherent clustering of submillimetre sources, we speculated that this structure is either a significant population of lensed submillimetre galaxies or a starbursting protocluster in a rapid phase of growth.

6.2 FUTURE WORK

The next wave of galaxy evolution studies lies in the coupling of star formation activity with molecular gas reservoirs at high redshift to determine how this relationship evolves with time. The current and future crop of novel telescopes, namely the Atacama Large Millimeter Array (ALMA) and CCAT, can offer valuable insight toward this aim through sensitive continuum and line emission. The lower rotational transitions of carbon monoxide (^{12}CO) provide an excellent tracer of the total cold gas content, while higher order transitions probe the denser gas.

Although the repository of CO emission lines at high redshift has steadily expanded with the advent of sensitive millimetre-wave arrays, it predominately comprises the most active and intrinsically luminous galaxies, namely SMGs and quasars (e.g., Riechers et al., 2006; Hainline et al., 2006; Ivison et al., 2010; Vieira et al., 2013). Such systems are thought to be highly efficient at converting their gas into stars (e.g., Greve et al., 2005). Until recently, a dearth of CO detections at intermediate and higher redshifts in typical star-forming galaxies has hindered a complete understanding of this important parameter space.

Indeed, studies have only recently begun to shed light onto the correlation between molecular gas and star formation at higher redshift, although mostly in the field (Daddi et al., 2008, 2010; Dannerbauer et al., 2009; Aravena et al., 2010; Tacconi et al., 2010; Combes et al., 2011; Pope et al., 2013). Cluster galaxies have been less studied, with only a handful of CO detections in total (Geach et al., 2009, 2011; Wagg et al., 2012). There is now mounting evidence that typical high-redshift galaxies fuel star formation through larger gas reservoirs at early epochs, rather than inherently greater star formation efficiencies, and are thus more similar to local quiescent spirals. Moreover, there appears to be a steep decline in the fraction of molecular gas in massive galaxies ($\gtrsim 10^{10}\,\mathrm{M}_{\odot}$) since $z \sim 2$. A missing key component of these studies is star-forming LIRGs within galaxy cluster cores at the epoch with which we expect star formation to begin to peak in high-density regions, $z \gtrsim 1$. Within these dense environments, an understanding of the available reservoir of molecular gas is crucial in order to constrain the various quenching mechanisms. Exploring this new frontier of CO emission lines in the highest-density regions at $z > 1$ holds the promise of exciting discoveries, and can provide a clear narrative of star formation histories in some of the rarest structures in the Universe.

BIBLIOGRAPHY

Aaronson, M. and Olszewski, E. W. Optical counterparts of unidentified IRAS point sources Infrared luminous galaxies. Nature, 309:414–417, 1984. doi: 10.1038/309414a0.

Abell, G. O. The Distribution of Rich Clusters of Galaxies. ApJS, 3:211, 1958. doi:10.1086/190036.

Alberts, S., Pope, A., Brodwin, M., Atlee, D. W., Lin, Y.-T., et al. The evolution of dust-obscured star formation activity in galaxy clusters relative to the field over the last 9 billion years. *ArXiv e-prints*, 2013. `1310.6040`.

Amblard, A., Cooray, A., Serra, P., Altieri, B., Arumugam, V., et al. Submillimetre galaxies reside in dark matter haloes with masses greater than 3x10e11 solar masses. Nature, 470:510–512, 2011. doi:10.1038/nature09771. `1101.1080`.

Aravena, M., Carilli, C., Daddi, E., Wagg, J., Walter, F., et al. Cold Molecular Gas in Massive, Star-forming Disk Galaxies at z = 1.5. ApJ, 718:177–183, 2010. doi:10.1088/0004-637X/718/1/177. `1005.4965`.

Aretxaga, I., Hughes, D. H., Coppin, K., Mortier, A. M. J., Wagg, J., et al. The SCUBA Half Degree Extragalactic Survey - IV. Radio-mm-FIR photometric redshifts. MNRAS, 379:1571–1588, 2007. doi:10.1111/j.1365-2966.2007.12036.x. `arXiv:astro-ph/0702503`.

Baldry, I. K., Balogh, M. L., Bower, R. G., Glazebrook, K., Nichol, R. C., et al. Galaxy bimodality versus stellar mass and environment. MNRAS, 373:469–483, 2006. doi:10.1111/j.1365-2966.2006.11081.x. `arXiv:astro-ph/0607648`.

Baldry, I. K., Glazebrook, K., Brinkmann, J., Ivezić, Ž., Lupton, R. H., et al. Quantifying the Bimodal Color-Magnitude Distribution of Galaxies. ApJ, 600:681–694, 2004. doi:10.1086/380092. `arXiv:astro-ph/0309710`.

Balogh, M., Eke, V., Miller, C., Lewis, I., Bower, R., et al. Galaxy ecology: groups and low-density environments in the SDSS and 2dFGRS. MNRAS, 348:1355–1372, 2004a. doi:10.1111/j.1365-2966.2004.07453.x. `arXiv:astro-ph/0311379`.

Balogh, M. L., Baldry, I. K., Nichol, R., Miller, C., Bower, R., et al. The Bimodal Galaxy Color Distribution: Dependence on Luminosity and Environment. ApJ, 615:L101–L104, 2004b. doi:10.1086/426079. `arXiv:astro-ph/0406266`.

Balogh, M. L., McGee, S. L., Wilman, D. J., Finoguenov, A., Parker, L. C., et al. Direct observational evidence for a large transient galaxy population in groups at 0.85 ¡ z ¡ 1. MNRAS, 412:2303–2317, 2011. doi:10.1111/j.1365-2966.2010.18052.x. `1011.5509`.

Balogh, M. L., Miller, C., Nichol, R., Zabludoff, A., and Goto, T. Near-infrared imaging of 222 nearby Hδ-strong galaxies from the Sloan Digital Sky Survey. MNRAS, 360:587–609, 2005. doi:10.1111/j.1365-2966.2005.09047.x. `astro-ph/0503639`.

Balogh, M. L., Morris, S. L., Yee, H. K. C., Carlberg, R. G., and Ellingson, E. Differential Galaxy Evolution in Cluster and Field Galaxies at z˜0.3. ApJ, 527:54–79, 1999. doi:10.1086/308056. `arXiv:astro-ph/9906470`.

Balogh, M. L., Navarro, J. F., and Morris, S. L. The Origin of Star Formation Gradients in Rich Galaxy Clusters. ApJ, 540:113–121, 2000. doi:10.1086/309323. `arXiv:astro-ph/0004078`.

Balogh, M. L., Schade, D., Morris, S. L., Yee, H. K. C., Carlberg, R. G., et al. The Dependence of Cluster Galaxy Star Formation Rates on the Global Environment. ApJ, 504:L75, 1998. doi:10.1086/311576. `arXiv:astro-ph/9806146`.

Barger, A. J., Aragon-Salamanca, A., Smail, I., Ellis, R. S., Couch, W. J., et al. New Constraints on the Luminosity Evolution of Spheroidal Galaxies in Distant Clusters. ApJ, 501:522–+, 1998a. `arXiv:astro-ph/9801112`.

Barger, A. J., Cowie, L. L., Sanders, D. B., Fulton, E., Taniguchi, Y., et al. Submillimetre-wavelength detection of dusty star-forming galaxies at high redshift. Nature, 394:248–251, 1998b.

Barnes, J. E. and Hernquist, L. E. Fueling starburst galaxies with gas-rich mergers. ApJ, 370:L65–L68, 1991. doi:10.1086/185978.

Bastian, N., Covey, K. R., and Meyer, M. R. A Universal Stellar Initial Mass Function? A Critical Look at Variations. ARA&A, 48:339–389, 2010. doi:10.1146/annurev-astro-082708-101642. `1001.2965`.

Bell, E. F. and de Jong, R. S. Stellar Mass-to-Light Ratios and the Tully-Fisher Relation. ApJ, 550:212–229, 2001. doi:10.1086/319728. `arXiv:astro-ph/0011493`.

Bell, E. F., McIntosh, D. H., Katz, N., and Weinberg, M. D. The Optical and Near-Infrared Properties of Galaxies. I. Luminosity and Stellar Mass Functions. ApJS, 149:289–312, 2003. doi:10.1086/378847. `arXiv:astro-ph/0302543`.

Bendo, G. J., Boselli, A., Dariush, A., Pohlen, M., Roussel, H., et al. Investigations of dust heating in M81, M83 and NGC 2403 with the Herschel Space Observatory. MNRAS, 419:1833–1859, 2012. doi:10.1111/j.1365-2966.2011.19735.x. `1109.0237`.

Bendo, G. J., Wilson, C. D., Pohlen, M., Sauvage, M., Auld, R., et al. The Herschel Space Observatory view of dust in M81. A&A, 518:L65, 2010. doi:10.1051/0004-6361/201014568. `1005.1889`.

Berta, S., Magnelli, B., Nordon, R., Lutz, D., Wuyts, S., et al. Building the cosmic infrared background brick by brick with Herschel/PEP. A&A, 532:A49, 2011. doi:10.1051/0004-6361/201116844. `1106.3070`.

Béthermin, M., Le Floc'h, E., Ilbert, O., Conley, A., Lagache, G., et al. HerMES: deep number counts at 250 μm, 350 μm and 500 μm in the COSMOS and GOODS-N fields and the build-up of the cosmic infrared background. A&A, 542:A58, 2012. doi:10.1051/0004-6361/201118698. `1203.1925`.

Bicay, M. D. and Giovanelli, R. Far-infrared properties of cluster galaxies. ApJ, 321:645–657, 1987. doi:10.1086/165659.

Biggs, A. D., Ivison, R. J., Ibar, E., Wardlow, J. L., Dannerbauer, H., et al. The LABOCA survey of the Extended Chandra Deep Field-South - radio and mid-infrared counterparts to submillimetre galaxies. MNRAS, 413:2314–2338, 2011. doi:10.1111/j.1365-2966.2010.18132.x. `1012.0305`.

Blain, A. W., Barnard, V. E., and Chapman, S. C. Submillimetre and far-infrared spectral energy distributions of galaxies: the luminosity-temperature relation and consequences for photometric redshifts. MNRAS, 338:733–744, 2003. doi:10.1046/j.1365-8711.2003.06086.x. `arXiv:astro-ph/0209450`.

Blain, A. W., Smail, I., Ivison, R. J., Kneib, J.-P., and Frayer, D. T. Submillimeter galaxies. Phys. Rep., 369:111–176, 2002. doi:10.1016/S0370-1573(02)00134-5. `arXiv:astro-ph/0202228`.

Blanton, M. R., Eisenstein, D., Hogg, D. W., Schlegel, D. J., and Brinkmann, J. Relationship between Environment and the Broadband Optical Properties of Galaxies in the Sloan Digital Sky Survey. ApJ, 629:143–157, 2005. doi:10.1086/422897. `arXiv:astro-ph/0310453`.

Blanton, M. R. and Moustakas, J. Physical Properties and Environments of Nearby Galaxies. ARA&A, 47:159–210, 2009. doi:10.1146/annurev-astro-082708-101734. `0908.3017`.

Blitz, L. and Shu, F. H. The origin and lifetime of giant molecular cloud complexes. ApJ, 238:148–157, 1980. doi:10.1086/157968.

Böhringer, H., Schuecker, P., Guzzo, L., Collins, C. A., Voges, W., et al. The ROSAT-ESO flux limited X-ray (REFLEX) galaxy cluster survey. I. The construction of the cluster sample. A&A, 369:826–850, 2001. doi:10.1051/0004-6361:20010240. `arXiv:astro-ph/0012266`.

Böhringer, H., Voges, W., Huchra, J. P., McLean, B., Giacconi, R., et al. The Northern ROSAT All-Sky (NORAS) Galaxy Cluster Survey. I. X-Ray Properties of Clusters Detected as Extended X-Ray Sources. ApJS, 129:435–474, 2000. doi:10.1086/313427. `arXiv:astro-ph/0003219`.

Böhringer, H. and Werner, N. X-ray spectroscopy of galaxy clusters: studying astrophysical processes in the largest celestial laboratories. A&A Rev., 18:127–196, 2010. doi:10.1007/s00159-009-0023-3.

Borgani, S., Murante, G., Springel, V., Diaferio, A., Dolag, K., et al. X-ray properties of galaxy clusters and groups from a cosmological hydrodynamical simulation. MNRAS, 348:1078–1096, 2004. doi:10.1111/j.1365-2966.2004.07431.x. `arXiv:astro-ph/0310794`.

Borys, C., Chapman, S., Halpern, M., and Scott, D. The Hubble Deep Field North SCUBA Super-map - I. Submillimetre maps, sources and number counts. MNRAS, 344:385–398, 2003. doi:10.1046/j.1365-8711.2003.06818.x. `arXiv:astro-ph/0305444`.

Boselli, A., Ciesla, L., Cortese, L., Buat, V., Boquien, M., et al. Far-infrared colours of nearby late-type galaxies in the Herschel Reference Survey. A&A, 540:A54, 2012. doi:10.1051/0004-6361/201118602. `1201.2305`.

Boselli, A. and Gavazzi, G. Environmental Effects on Late-Type Galaxies in Nearby Clusters. PASP, 118:517–559, 2006. doi:10.1086/500691. `astro-ph/0601108`.

Boulade, O., Charlot, X., Abbon, P., Aune, S., Borgeaud, P., et al. MegaCam: the new Canada-France-Hawaii Telescope wide-field imaging camera. In M. Iye and A. F. M. Moorwood, editors, *Society of Photo-Optical Instrumentation Engineers (SPIE) Conference Series*, volume 4841 of *Society of Photo-Optical Instrumentation Engineers (SPIE) Conference Series*, pages 72–81. 2003. doi:10.1117/12.459890.

Bourne, N., Dunne, L., Bendo, G. J., Smith, M. W. L., Clark, C. J. R., et al. Herschel-ATLAS: correlations between dust and gas in local submm-selected galaxies. MNRAS, 436:479–502, 2013. doi:10.1093/mnras/stt1584. `1308.4406`.

Bouwens, R. J., Illingworth, G. D., Franx, M., and Ford, H. UV Luminosity Functions at z˜4, 5, and 6 from the Hubble Ultra Deep Field and Other Deep Hubble Space Telescope ACS Fields: Evolution and Star Formation History. ApJ, 670:928–958, 2007. doi:10.1086/521811. `0707.2080`.

Bower, R. G., Lucey, J. R., and Ellis, R. S. Precision Photometry of Early Type Galaxies in the Coma and Virgo Clusters - a Test of the Universality of the Colour / Magnitude Relation - Part Two - Analysis. MNRAS, 254:601–+, 1992.

Brinchmann, J., Charlot, S., White, S. D. M., Tremonti, C., Kauffmann, G., et al. The physical properties of star-forming galaxies in the low-redshift Universe. MNRAS, 351:1151–1179, 2004. doi:10.1111/j.1365-2966.2004.07881.x. `arXiv:astro-ph/0311060`.

Brodwin, M., Brown, M. J. I., Ashby, M. L. N., Bian, C., Brand, K., et al. Photometric Redshifts in the IRAC Shallow Survey. ApJ, 651:791–803, 2006. doi:10.1086/507838. `arXiv:astro-ph/0607450`.

Bruzual, A. G. and Charlot, S. Spectral evolution of stellar populations using isochrone synthesis. ApJ, 405:538–553, 1993. doi:10.1086/172385.

Bruzual, G. and Charlot, S. Stellar population synthesis at the resolution of 2003. MNRAS, 344:1000–1028, 2003. doi:10.1046/j.1365-8711.2003.06897.x. `arXiv:astro-ph/0309134`.

Butcher, H. and Oemler, A., Jr. The evolution of galaxies in clusters. I - ISIT photometry of C1 0024+1654 and 3C 295. ApJ, 219:18–30, 1978. doi:10.1086/155751.

—. The evolution of galaxies in clusters. V - A study of populations since Z approximately equal to 0.5. ApJ, 285:426–438, 1984. doi:10.1086/162519.

Calzetti, D., Armus, L., Bohlin, R. C., Kinney, A. L., Koornneef, J., et al. The Dust Content and Opacity of Actively Star-forming Galaxies. ApJ, 533:682–695, 2000. doi:10.1086/308692. `arXiv:astro-ph/9911459`.

Calzetti, D., Kennicutt, R. C., Engelbracht, C. W., Leitherer, C., Draine, B. T., et al. The Calibration of Mid-Infrared Star Formation Rate Indicators. ApJ, 666:870–895, 2007. doi:10.1086/520082. `0705.3377`.

Calzetti, D., Kennicutt, R. C., Jr., Bianchi, L., Thilker, D. A., Dale, D. A., et al. Star Formation in NGC 5194 (M51a): The Panchromatic View from GALEX to Spitzer. ApJ, 633:871–893, 2005. doi:10.1086/466518. `arXiv:astro-ph/0507427`.

Cappellari, M., di Serego Alighieri, S., Cimatti, A., Daddi, E., Renzini, A., et al. Dynamical Masses of Early-Type Galaxies at z ˜ 2: Are they Truly Superdense? ApJ, 704:L34–L39, 2009. doi:10.1088/0004-637X/704/1/L34. `0906.3648`.

Carilli, C. L. and Yun, M. S. The Radio-to-Submillimeter Spectral Index as a Redshift Indicator. ApJ, 513:L13–L16, 1999. doi:10.1086/311909. `arXiv:astro-ph/9812251`.

Carlberg, R. G., Yee, H. K. C., and Ellingson, E. The Average Mass and Light Profiles of Galaxy Clusters. ApJ, 478:462, 1997. doi:10.1086/303805. `astro-ph/9512087`.

Carlstrom, J. E., Holder, G. P., and Reese, E. D. Cosmology with the Sunyaev-Zel'dovich Effect. ARA&A, 40:643–680, 2002. doi:10.1146/annurev.astro.40.060401.093803. `arXiv:astro-ph/0208192`.

Casey, C. M., Berta, S., Béthermin, M., Bock, J., Bridge, C., et al. A Redshift Survey of Herschel Far-infrared Selected Starbursts and Implications for Obscured Star Formation. ApJ, 761:140, 2012. doi:10.1088/0004-637X/761/2/140. `1210.4928`.

Casey, C. M., Chen, C.-C., Cowie, L., Barger, A., Capak, P., et al. Characterisation of SCUBA-2 450um and 850um-selected Galaxies in the COSMOS Field. *ArXiv e-prints*, 2013. `1302.2619`.

Castander, F. J., Ellis, R. S., Frenk, C. S., Dressler, A., and Gunn, J. E. The detection of X-ray emission from the highest redshift galaxy clusters. ApJ, 424:L79–L82, 1994. doi:10.1086/187279.

Chabrier, G. Galactic Stellar and Substellar Initial Mass Function. PASP, 115:763–795, 2003. doi:10.1086/376392. `arXiv:astro-ph/0304382`.

Chapin, E. L., Berry, D. S., Gibb, A. G., Jenness, T., Scott, D., et al. SCUBA-2: iterative map-making with the Sub-Millimetre User Reduction Facility. MNRAS, 430:2545–2573, 2013. doi:10.1093/mnras/stt052. `1301.3652`.

Chapman, S. C., Blain, A. W., Smail, I., and Ivison, R. J. A Redshift Survey of the Submillimeter Galaxy Population. ApJ, 622:772–796, 2005. `arXiv:astro-ph/0412573`.

Chapman, S. C., Helou, G., Lewis, G. F., and Dale, D. A. The Bivariate Luminosity-Color Distribution of IRAS Galaxies and Implications for the High-Redshift Universe. ApJ, 588:186–198, 2003. doi:10.1086/374038. `arXiv:astro-ph/0301233`.

Chapman, S. C., Lewis, G. F., Scott, D., Richards, E., Borys, C., et al. Submillimeter Imaging of a Protocluster Region at Z=3.09. ApJ, 548:L17–L21, 2001. doi:10.1086/318919. `arXiv:astro-ph/0010101`.

Chary, R. and Elbaz, D. Interpreting the Cosmic Infrared Background: Constraints on the Evolution of the Dust-enshrouded Star Formation Rate. ApJ, 556:562–581, 2001. doi:10.1086/321609. `arXiv:astro-ph/0103067`.

Chen, C.-C., Cowie, L. L., Barger, A. J., Casey, C. M., Lee, N., et al. Faint Submillimeter Galaxy Counts at 450 μm. ApJ, 762:81, 2013. doi:10.1088/0004-637X/762/2/81. `1209.4377`.

Chung, A., van Gorkom, J. H., Kenney, J. D. P., and Vollmer, B. Virgo Galaxies with Long One-sided H I Tails. ApJ, 659:L115–L119, 2007. doi:10.1086/518034. `astro-ph/0703338`.

Combes, F., García-Burillo, S., Braine, J., Schinnerer, E., Walter, F., et al. Galaxy evolution and star formation efficiency at 0.2¡ z ¡ 0.6. A&A, 528:A124, 2011. doi:10.1051/0004-6361/201015739. `1009.2040`.

Condon, J. J. Confusion and Flux-Density Error Distributions. ApJ, 188:279–286, 1974. doi:10.1086/152714.

Conroy, C. Modeling the Panchromatic Spectral Energy Distributions of Galaxies. ARA&A, 51:393–455, 2013. doi:10.1146/annurev-astro-082812-141017. `1301.7095`.

Cooper, M. C., Newman, J. A., Weiner, B. J., Yan, R., Willmer, C. N. A., et al. The DEEP2 Galaxy Redshift Survey: the role of galaxy environment in the cosmic star formation history. MNRAS, 383:1058–1078, 2008. doi:10.1111/j.1365-2966.2007.12613.x. `0706.4089`.

Coppin, K., Chapin, E. L., Mortier, A. M. J., Scott, S. E., Borys, C., et al. The SCUBA Half-Degree Extragalactic Survey - II. Submillimetre maps, catalogue and number counts. MNRAS, 372:1621–1652, 2006. doi:10.1111/j.1365-2966.2006.10961.x. `arXiv:astro-ph/0609039`.

Coppin, K. E. K., Geach, J. E., Webb, T. M. A., Faloon, A., Yan, R., et al. The Herschel Filament: A Signature of the Environmental Drivers of Galaxy Evolution during the Assembly of Massive Clusters at z = 0.9. ApJ, 749:L43, 2012. doi:10.1088/2041-8205/749/2/L43. `1203.0007`.

Couch, W. J. and Sharples, R. M. A spectroscopic study of three rich galaxy clusters at Z = 0.31. MNRAS, 229:423–456, 1987.

Cowie, L. L., Barger, A. J., and Kneib, J.-P. Faint Submillimeter Counts from Deep 850 Micron Observations of the Lensing Clusters A370, A851, and A2390. AJ, 123:2197–2205, 2002. `arXiv:astro-ph/0201426`.

Cox, P., Krips, M., Neri, R., Omont, A., Güsten, R., et al. Gas and Dust in a Submillimeter Galaxy at z = 4.24 from the Herschel Atlas. ApJ, 740:63, 2011. doi:10.1088/0004-637X/740/2/63. `1107.2924`.

Cox, P., Kruegel, E., and Mezger, P. G. Principal heating sources of dust in the galactic disk. A&A, 155:380–396, 1986.

Daddi, E., Bournaud, F., Walter, F., Dannerbauer, H., Carilli, C. L., et al. Very High Gas Fractions and Extended Gas Reservoirs in z = 1.5 Disk Galaxies. ApJ, 713:686–707, 2010. doi:10.1088/0004-637X/713/1/686. `0911.2776`.

Daddi, E., Dannerbauer, H., Elbaz, D., Dickinson, M., Morrison, G., et al. Vigorous Star Formation with Low Efficiency in Massive Disk Galaxies at z = 1.5. ApJ, 673:L21–L24, 2008. doi:10.1086/527377. `0711.4995`.

Daddi, E., Dannerbauer, H., Stern, D., Dickinson, M., Morrison, G., et al. Two Bright Submillimeter Galaxies in a z = 4.05 Protocluster in Goods-North, and Accurate Radio-Infrared Photometric Redshifts. ApJ, 694:1517–1538, 2009. doi:10.1088/0004-637X/694/2/1517. `0810.3108`.

Daddi, E., Dickinson, M., Morrison, G., Chary, R., Cimatti, A., et al. Multiwavelength Study of Massive Galaxies at z˜2. I. Star Formation and Galaxy Growth. ApJ, 670:156–172, 2007. doi:10.1086/521818. `0705.2831`.

Dale, D. A. and Helou, G. The Infrared Spectral Energy Distribution of Normal Star-forming Galaxies: Calibration at Far-Infrared and Submillimeter Wavelengths. ApJ, 576:159–168, 2002. doi:10.1086/341632. `arXiv:astro-ph/0205085`.

Dannerbauer, H., Daddi, E., Riechers, D. A., Walter, F., Carilli, C. L., et al. Low Milky-Way-Like Molecular Gas Excitation of Massive Disk Galaxies at z 1.5. ApJ, 698:L178–L182, 2009. doi:10.1088/0004-637X/698/2/L178. `0905.3637`.

de Jong, T., Clegg, P. E., Rowan-Robinson, M., Soifer, B. T., Habing, H. J., et al. IRAS observations of Shapley-Ames galaxies. ApJ, 278:L67–L70, 1984. doi:10.1086/184225.

De Lucia, G., Poggianti, B. M., Halliday, C., Milvang-Jensen, B., Noll, S., et al. On the role of the post-starburst phase in the buildup of the red sequence of intermediate-redshift clusters. MNRAS, 400:68–77, 2009. doi:10.1111/j.1365-2966.2009.15435.x. `0907.3922`.

Demarco, R., Wilson, G., Muzzin, A., Lacy, M., Surace, J., et al. Spectroscopic Confirmation of Three Red-sequence Selected Galaxy Clusters at z = 0.87, 1.16, and 1.21 from the SpARCS Survey. ApJ, 711:1185–1197, 2010. doi:10.1088/0004-637X/711/2/1185. `1002.0160`.

Devlin, M. J., Ade, P. A. R., Aretxaga, I., Bock, J. J., Chapin, E. L., et al. Over half of the far-infrared background light comes from galaxies at z¿1.2. Nature, 458:737–739, 2009. doi:10.1038/nature07918. `0904.1201`.

Dole, H., Lagache, G., Puget, J.-L., Caputi, K. I., Fernández-Conde, N., et al. The cosmic infrared background resolved by Spitzer. Contributions of mid-infrared galaxies to the far-infrared background. A&A, 451:417–429, 2006. doi:10.1051/0004-6361:20054446. `arXiv:astro-ph/0603208`.

Doyon, R. and Joseph, R. D. Dust deficiency in Virgo spirals. MNRAS, 239:347–360, 1989.

Draine, B. T. Interstellar Dust Grains. ARA&A, 41:241–289, 2003. doi:10.1146/annurev.astro.41.011802.094840. `arXiv:astro-ph/0304489`.

Dressler, A. Galaxy morphology in rich clusters - Implications for the formation and evolution of galaxies. ApJ, 236:351–365, 1980. doi:10.1086/157753.

Dressler, A. and Gunn, J. E. Spectroscopy of galaxies in distant clusters. II - The population of the 3C 295 cluster. ApJ, 270:7–19, 1983. doi:10.1086/161093.

Dressler, A., Oemler, A. J., Couch, W. J., Smail, I., Ellis, R. S., et al. Evolution since Z = 0.5 of the Morphology-Density Relation for Clusters of Galaxies. ApJ, 490:577–+, 1997. `arXiv:astro-ph/9707232`.

Dressler, A., Smail, I., Poggianti, B. M., Butcher, H., Couch, W. J., et al. A Spectroscopic Catalog of 10 Distant Rich Clusters of Galaxies. ApJS, 122:51–80, 1999. doi:10.1086/313213. `arXiv:astro-ph/9901263`.

Dunne, L., Eales, S., Edmunds, M., Ivison, R., Alexander, P., et al. The SCUBA Local Universe Galaxy Survey - I. First measurements of the submillimetre luminosity and dust mass functions. MNRAS, 315:115–139, 2000. doi:10.1046/j.1365-8711.2000.03386.x. `arXiv:astro-ph/0002234`.

Dunne, L. and Eales, S. A. The SCUBA Local Universe Galaxy Survey - II. 450-μm data: evidence for cold dust in bright IRAS galaxies. MNRAS, 327:697–714, 2001. doi:10.1046/j.1365-8711.2001.04789.x. `astro-ph/0106362`.

Eales, S., Dunne, L., Clements, D., Cooray, A., de Zotti, G., et al. The Herschel ATLAS. PASP, 122:499–515, 2010. doi:10.1086/653086. `0910.4279`.

Eales, S., Lilly, S., Gear, W., Dunne, L., Bond, J. R., et al. The Canada-UK Deep Submillimeter Survey: First Submillimeter Images, the Source Counts, and Resolution of the Background. ApJ, 515:518–524, 1999. doi:10.1086/307069. `arXiv:astro-ph/9808040`.

Ebeling, H., Edge, A. C., Bohringer, H., Allen, S. W., Crawford, C. S., et al. The ROSAT Brightest Cluster Sample - I. The compilation of the sample and the cluster log N-log S distribution. MNRAS, 301:881–914, 1998. doi:10.1046/j.1365-8711.1998.01949.x. `arXiv:astro-ph/9812394`.

Ebeling, H., Edge, A. C., and Henry, J. P. MACS: A Quest for the Most Massive Galaxy Clusters in the Universe. ApJ, 553:668–676, 2001. doi:10.1086/320958. `arXiv:astro-ph/0009101`.

Eisenhardt, P. R. M., Brodwin, M., Gonzalez, A. H., Stanford, S. A., Stern, D., et al. Clusters of Galaxies in the First Half of the Universe from the IRAC Shallow Survey. ApJ, 684:905–932, 2008. doi:10.1086/590105. `0804.4798`.

Elbaz, D., Daddi, E., Le Borgne, D., Dickinson, M., Alexander, D. M., et al. The reversal of the star formation-density relation in the distant universe. A&A, 468:33–48, 2007. doi:10.1051/0004-6361:20077525. `arXiv:astro-ph/0703653`.

Elbaz, D., Dickinson, M., Hwang, H. S., Díaz-Santos, T., Magdis, G., et al. GOODS-Herschel: an infrared main sequence for star-forming galaxies. A&A, 533:A119, 2011. doi:10.1051/0004-6361/201117239. `1105.2537`.

Elbaz, D., Hwang, H. S., Magnelli, B., Daddi, E., Aussel, H., et al. Herschel unveils a puzzling uniformity of distant dusty galaxies. A&A, 518:L29, 2010. doi:10.1051/0004-6361/201014687. `1005.2859`.

Ellingson, E., Lin, H., Yee, H. K. C., and Carlberg, R. G. The Evolution of Population Gradients in Galaxy Clusters: The Butcher-Oemler Effect and Cluster Infall. ApJ, 547:609–622, 2001. doi:10.1086/318423. `arXiv:astro-ph/0010141`.

Fadda, D., Yan, L., Lagache, G., Sajina, A., Lutz, D., et al. Ultra-deep Mid-infrared Spectroscopy of Luminous Infrared Galaxies at z ˜ 1 and z ˜ 2. ApJ, 719:425–450, 2010. doi:10.1088/0004-637X/719/1/425.

Faloon, A. J., Webb, T. M. A., Ellingson, E., Yan, R., Gilbank, D. G., et al. The Structure of the Merging RCS 231953+00 Supercluster at z ˜ 0.9. ApJ, 768:104, 2013. doi:10.1088/0004-637X/768/2/104. `1302.4344`.

Fazio, G. G., Hora, J. L., Allen, L. E., Ashby, M. L. N., Barmby, P., et al. The Infrared Array Camera (IRAC) for the Spitzer Space Telescope. ApJS, 154:10–17, 2004. doi:10.1086/422843. `arXiv:astro-ph/0405616`.

Feulner, G., Goranova, Y., Hopp, U., Gabasch, A., Bender, R., et al. The Munich Near-Infrared Cluster Survey - IX. Galaxy evolution to z $\tilde{2}$ from optically selected catalogues. MNRAS, 378:429–448, 2007. doi:10.1111/j.1365-2966.2007.11802.x. `arXiv:astro-ph/0703792`.

Finn, R. A., Desai, V., Rudnick, G., Poggianti, B., Bell, E. F., et al. Dust-obscured Star Formation in Intermediate Redshift Galaxy Clusters. ApJ, 720:87–98, 2010. doi:10.1088/0004-637X/720/1/87. `1010.5164`.

Fixsen, D. J., Dwek, E., Mather, J. C., Bennett, C. L., and Shafer, R. A. The Spectrum of the Extragalactic Far-Infrared Background from the COBE FIRAS Observations. ApJ, 508:123–128, 1998. doi:10.1086/306383. `arXiv:astro-ph/9803021`.

Förster Schreiber, N. M., van Dokkum, P. G., Franx, M., Labbé, I., Rudnick, G., et al. A Substantial Population of Red Galaxies at z ¿ 2: Modeling of the Spectral Energy Distributions of an Extended Sample. ApJ, 616:40–62, 2004. doi:10.1086/424838. `arXiv:astro-ph/0408077`.

Frayer, D. T., Ivison, R. J., Scoville, N. Z., Evans, A. S., Yun, M. S., et al. Molecular Gas in the Z = 2.565 Submillimeter Galaxy SMM J14011+0252. ApJ, 514:L13–L16, 1999. doi:10.1086/311940. `arXiv:astro-ph/9901311`.

Frayer, D. T., Ivison, R. J., Scoville, N. Z., Yun, M., Evans, A. S., et al. Molecular Gas in the Z = 2.8 Submillimeter Galaxy SMM 02399-0136. ApJ, 506:L7–L10, 1998. doi:10.1086/311639. `arXiv:astro-ph/9808109`.

Fruchter, A. S. and Hook, R. N. Drizzle: A Method for the Linear Reconstruction of Undersampled Images. PASP, 114:144–152, 2002. doi:10.1086/338393. `arXiv:astro-ph/9808087`.

Fu, H., Jullo, E., Cooray, A., Bussmann, R. S., Ivison, R. J., et al. A Comprehensive View of a Strongly Lensed Planck-Associated Submillimeter Galaxy. ApJ, 753:134, 2012. doi:10.1088/0004-637X/753/2/134. `1202.1829`.

Fu, H., Yan, L., Scoville, N. Z., Capak, P., Aussel, H., et al. Decomposing Star Formation and Active Galactic Nucleus with Spitzer Mid-infrared Spectra: Luminosity Functions and Co-evolution. ApJ, 722:653–667, 2010. doi:10.1088/0004-637X/722/1/653. `1008.2932`.

Fujita, Y. and Nagashima, M. Effects of Ram Pressure from the Intracluster Medium on the Star Formation Rate of Disk Galaxies in Clusters of Galaxies. ApJ, 516:619–625, 1999. doi:10.1086/307139. `astro-ph/9812378`.

Geach, J. E., Chapin, E. L., Coppin, K. E. K., Dunlop, J. S., Halpern, M., et al. The SCUBA-2 Cosmology Legacy Survey: blank-field number counts of 450-μm-selected galaxies and their contribution to the cosmic infrared background. MNRAS, 432:53–61, 2013. doi:10.1093/mnras/stt352. `1211.6668`.

Geach, J. E., Matsuda, Y., Smail, I., Chapman, S. C., Yamada, T., et al. A submillimetre survey of Lyman α haloes in the SA22 protocluster at z= 3.1. MNRAS, 363:1398–1408, 2005. doi:10.1111/j.1365-2966.2005.09538.x. `arXiv:astro-ph/0508357`.

Geach, J. E., Smail, I., Coppin, K., Moran, S. M., Edge, A. C., et al. CO interferometry of gas-rich spiral galaxies in the outskirts of an intermediate redshift cluster. MNRAS, 395:L62–L66, 2009. doi:10.1111/j.1745-3933.2009.00642.x. `0902.2780`.

Geach, J. E., Smail, I., Moran, S. M., MacArthur, L. A., Lagos, C. d. P., et al. On the Evolution of the Molecular Gas Fraction of Star-Forming Galaxies. ApJ, 730:L19, 2011. doi:10.1088/2041-8205/730/2/L19. `1102.3694`.

Giacconi, R., Zirm, A., Wang, J., Rosati, P., Nonino, M., et al. Chandra Deep Field South: The 1 Ms Catalog. ApJS, 139:369–410, 2002. doi:10.1086/338927.

Giallongo, E., D'Odorico, S., Fontana, A., Cristiani, S., Egami, E., et al. The Photometric Redshift Distribution and Evolutionary Properties of Galaxies up to Z ˜ 4.5 in the Field of the Quasar BR 1202-0725. AJ, 115:2169–2183, 1998. doi:10.1086/300361. `arXiv:astro-ph/9802340`.

Gilbank, D. G., Gladders, M. D., Yee, H. K. C., and Hsieh, B. C. The Red-sequence Cluster Survey-2 (RCS-2): Survey Details and Photometric Catalog Construction. AJ, 141:94, 2011. doi:10.1088/0004-6256/141/3/94. `1012.3470`.

Gilbank, D. G., Yee, H. K. C., Ellingson, E., Gladders, M. D., Barrientos, L. F., et al. Spectroscopy of Moderately High Redshift RCS-1 Clusters. AJ, 134:282–293, 2007. doi:10.1086/518561. `0705.0782`.

Gilbank, D. G., Yee, H. K. C., Ellingson, E., Hicks, A. K., Gladders, M. D., et al. A z = 0.9 Supercluster of X-Ray Luminous, Optically Selected, Massive Galaxy Clusters. ApJ, 677:L89–L92, 2008. `0803.1675`.

Gill, S. P. D., Knebe, A., and Gibson, B. K. The evolution of substructure - III. The outskirts of clusters. MNRAS, 356:1327–1332, 2005. doi:10.1111/j.1365-2966.2004.08562.x. `arXiv:astro-ph/0404427`.

Gioia, I. M., Maccacaro, T., Schild, R. E., Wolter, A., Stocke, J. T., et al. The Einstein Observatory Extended Medium-Sensitivity Survey. I - X-ray data and analysis. ApJS, 72:567–619, 1990. doi:10.1086/191426.

Gladders, M. D., Hoekstra, H., Yee, H. K. C., Hall, P. B., and Barrientos, L. F. The Incidence of Strong-Lensing Clusters in the Red-Sequence Cluster Survey. ApJ, 593:48–55, 2003. doi:10.1086/376518. `arXiv:astro-ph/0303341`.

Gladders, M. D. and Yee, H. K. C. A New Method For Galaxy Cluster Detection. I. The Algorithm. AJ, 120:2148–2162, 2000. `arXiv:astro-ph/0004092`.

—. The Red-Sequence Cluster Survey. I. The Survey and Cluster Catalogs for Patches RCS 0926+37 and RCS 1327+29. ApJS, 157:1–29, 2005. `arXiv:astro-ph/0411075`.

Gobat, R., Daddi, E., Onodera, M., Finoguenov, A., Renzini, A., et al. A mature cluster with X-ray emission at z = 2.07. A&A, 526:A133, 2011. doi:10.1051/0004-6361/201016084. `1011.1837`.

Goldader, J. D., Joseph, R. D., Doyon, R., and Sanders, D. B. Spectroscopy of Luminous Infrared Galaxies at 2 Microns. III. Analysis for Galaxies with log (L IR/L) 11.2. ApJ, 474:104, 1997. doi:10.1086/303448.

Gómez, P. L., Nichol, R. C., Miller, C. J., Balogh, M. L., Goto, T., et al. Galaxy Star Formation as a Function of Environment in the Early Data Release of the Sloan Digital Sky Survey. ApJ, 584:210–227, 2003. doi:10.1086/345593. `arXiv:astro-ph/0210193`.

Greve, T. R., Bertoldi, F., Smail, I., Neri, R., Chapman, S. C., et al. An interferometric CO survey of luminous submillimetre galaxies. MNRAS, 359:1165–1183, 2005. doi:10.1111/j.1365-2966.2005.08979.x. `astro-ph/0503055`.

Griffin, M. J., Abergel, A., Abreu, A., Ade, P. A. R., André, P., et al. The Herschel-SPIRE instrument and its in-flight performance. A&A, 518:L3, 2010. doi:10.1051/0004-6361/201014519. `1005.5123`.

Gunn, J. E. and Gott, J. R., III. On the Infall of Matter Into Clusters of Galaxies and Some Effects on Their Evolution. ApJ, 176:1, 1972. doi:10.1086/151605.

Gunn, J. E., Hoessel, J. G., and Oke, J. B. A systematic survey for distant galaxy clusters. ApJ, 306:30–37, 1986. doi:10.1086/164317.

Haines, C. P., Pereira, M. J., Sanderson, A. J. R., Smith, G. P., Egami, E., et al. LoCuSS: A Dynamical Analysis of X-Ray Active Galactic Nuclei in Local Clusters. ApJ, 754:97, 2012. doi:10.1088/0004-637X/754/2/97. `1205.6818`.

Haines, C. P., Pereira, M. J., Smith, G. P., Egami, E., Sanderson, A. J. R., et al. LoCuSS: The Steady Decline and Slow Quenching of Star Formation in Cluster Galaxies over the Last Four Billion Years. ApJ, 775:126, 2013. doi:10.1088/0004-637X/775/2/126. `1307.1135`.

Haines, C. P., Smith, G. P., Egami, E., Ellis, R. S., Moran, S. M., et al. LOCUSS: The Mid-Infrared Butcher-Oemler Effect. ApJ, 704:126–136, 2009. doi:10.1088/0004-637X/704/1/126. `0908.3003`.

Hainline, L. J., Blain, A. W., Greve, T. R., Chapman, S. C., Smail, I., et al. Observing Cold Gas in Submillimeter Galaxies: Detection of CO (1–0) Emission in SMM J13120+4242 with the Green Bank Telescope. ApJ, 650:614–623, 2006. doi:10.1086/507443. `astro-ph/0607089`.

Harrison, C. M., Alexander, D. M., Mullaney, J. R., Altieri, B., Coia, D., et al. No clear submillimetre signature of suppressed star formation amongst X-ray luminous AGNs. *ArXiv e-prints*, 2012. `1209.3016`.

Hasselfield, M., Hilton, M., Marriage, T. A., Addison, G. E., Barrientos, L. F., et al. The Atacama Cosmology Telescope: Sunyaev-Zel'dovich selected galaxy clusters at 148 GHz from three seasons of data. *Journal of Cosmology and Astroparticle Physics*, 7:008, 2013. doi:10.1088/1475-7516/2013/07/008. `1301.0816`.

Hauser, M. G., Arendt, R. G., Kelsall, T., Dwek, E., Odegard, N., et al. The COBE Diffuse Infrared Background Experiment Search for the Cosmic Infrared Background. I. Limits and Detections. ApJ, 508:25–43, 1998. doi:10.1086/306379. `arXiv:astro-ph/9806167`.

Hauser, M. G. and Dwek, E. The Cosmic Infrared Background: Measurements and Implications. ARA&A, 39:249–307, 2001. doi:10.1146/annurev.astro.39.1.249. `arXiv:astro-ph/0105539`.

Helou, G. The IRAS colors of normal galaxies. ApJ, 311:L33–L36, 1986. doi:10.1086/184793.

Hess, K. M. and Wilcots, E. M. Evolution in the H I Gas Content of Galaxy Groups: Pre-processing and Mass Assembly in the Current Epoch. AJ, 146:124, 2013. doi:10.1088/0004-6256/146/5/124. `1308.4646`.

Hickox, R. C., Wardlow, J. L., Smail, I., Myers, A. D., Alexander, D. M., et al. The LABOCA survey of the Extended Chandra Deep Field-South: clustering of submillimetre galaxies. MNRAS, 421:284–295, 2012. doi:10.1111/j.1365-2966.2011.20303.x. `1112.0321`.

Hicks, A. K., Ellingson, E., Bautz, M., Cain, B., Gilbank, D. G., et al. Chandra X-Ray Observations of the 0.6 ¡ z ¡ 1.1 Red-Sequence Cluster Survey Sample. ApJ, 680:1022–1041, 2008. `0710.5513`.

Hildebrand, R. H. The Determination of Cloud Masses and Dust Characteristics from Submillimetre Thermal Emission. QJRAS, 24:267, 1983.

Hoekstra, H., Yee, H. K. C., and Gladders, M. D. Constraints on Ω_m and σ_8 from Weak Lensing in Red-Sequence Cluster Survey Fields. ApJ, 577:595–603, 2002a. doi:10.1086/342120. `arXiv:astro-ph/0204295`.

Hoekstra, H., Yee, H. K. C., Gladders, M. D., Barrientos, L. F., Hall, P. B., et al. A Measurement of Weak Lensing by Large-Scale Structure in Red-Sequence Cluster Survey Fields. ApJ, 572:55–65, 2002b. doi:10.1086/340298. `arXiv:astro-ph/0202285`.

Hogg, D. W., Blanton, M. R., Brinchmann, J., Eisenstein, D. J., Schlegel, D. J., et al. The Dependence on Environment of the Color-Magnitude Relation of Galaxies. ApJ, 601:L29–L32, 2004. doi:10.1086/381749. `arXiv:astro-ph/0307336`.

Holder, G. P., Viero, M. P., Zahn, O., Aird, K. A., Benson, B. A., et al. A Cosmic Microwave Background Lensing Mass Map and Its Correlation with the Cosmic Infrared Background. ApJ, 771:L16, 2013. doi:10.1088/2041-8205/771/1/L16. `1303.5048`.

Holland, W. S., Bintley, D., Chapin, E. L., Chrysostomou, A., Davis, G. R., et al. SCUBA-2: the 10 000 pixel bolometer camera on the James Clerk Maxwell Telescope. MNRAS, 430:2513–2533, 2013. doi:10.1093/mnras/sts612. `1301.3650`.

Hollenbach, D. and Salpeter, E. E. Surface Recombination of Hydrogen Molecules. ApJ, 163:155, 1971. doi:10.1086/150754.

Hopkins, A. M. On the Evolution of Star-forming Galaxies. ApJ, 615:209–221, 2004. doi:10.1086/424032. `arXiv:astro-ph/0407170`.

Hopkins, A. M. and Beacom, J. F. On the Normalization of the Cosmic Star Formation History. ApJ, 651:142–154, 2006. doi:10.1086/506610. `arXiv:astro-ph/0601463`.

Houck, J. R., Schneider, D. P., Danielson, G. E., Neugebauer, G., Soifer, B. T., et al. Unidentified IRAS sources - Ultrahigh-luminosity galaxies. ApJ, 290:L5–L8, 1985. doi:10.1086/184431.

Howk, J. C. and Savage, B. D. A Search for Extraplanar Dust in Nearby Edge-on Spirals. AJ, 117:2077–2101, 1999. doi:10.1086/300857. `astro-ph/9902061`.

Hubble, E. and Humason, M. L. The Velocity-Distance Relation among Extra-Galactic Nebulae. ApJ, 74:43, 1931. doi:10.1086/143323.

Hubble, E. P. Extragalactic nebulae. ApJ, 64:321–369, 1926. doi:10.1086/143018.

Hughes, D. H., Serjeant, S., Dunlop, J., Rowan-Robinson, M., Blain, A., et al. High-redshift star formation in the Hubble Deep Field revealed by a submillimetre-wavelength survey. Nature, 394:241–247, 1998. `arXiv:astro-ph/9806297`.

Ibar, E., Cirasuolo, M., Ivison, R., Best, P., Smail, I., et al. Exploring the infrared/radio correlation at high redshift. MNRAS, 386:953–962, 2008. doi:10.1111/j.1365-2966.2008.13077.x. `0802.2694`.

Icke, V. Distant encounters between disk galaxies and the origin of S 0 spirals. A&A, 144:115–123, 1985.

Ivison, R. J., Greve, T. R., Dunlop, J. S., Peacock, J. A., Egami, E., et al. The SCUBA HAlf Degree Extragalactic Survey - III. Identification of radio and mid-infrared counterparts to submillimetre galaxies. MNRAS, 380:199–228, 2007. doi:10.1111/j.1365-2966.2007.12044.x. `arXiv:astro-ph/0702544`.

Ivison, R. J., Smail, I., Papadopoulos, P. P., Wold, I., Richard, J., et al. Gas, dust and stars in the SCUBA galaxy, SMMJ02399-0136: the EVLA reveals a colossal galactic nursery. MNRAS, 404:198–205, 2010. doi:10.1111/j.1365-2966.2010.16322.x. `0912.1591`.

Jee, M. J., Dawson, K. S., Hoekstra, H., Perlmutter, S., Rosati, P., et al. Scaling Relations and Overabundance of Massive Clusters at z ¿1 from Weak-lensing Studies with the Hubble Space Telescope. ApJ, 737:59, 2011. doi:10.1088/0004-637X/737/2/59. `1105.3186`.

Jenness, T., Berry, D., Chapin, E., Economou, F., Gibb, A., et al. SCUBA-2 Data Processing. In I. N. Evans, A. Accomazzi, D. J. Mink, and A. H. Rots, editors, *Astronomical Data Analysis Software and Systems XX*, volume 442 of *Astronomical Society of the Pacific Conference Series*, page 281. 2011. `1011.5876`.

Kauffmann, G. and Charlot, S. The K-band luminosity function at z=1: a powerful constraint on galaxy formation theory. MNRAS, 297:L23, 1998. doi:10.1046/j.1365-8711.1998.01708.x. `arXiv:astro-ph/9802233`.

Kauffmann, G., Heckman, T. M., White, S. D. M., Charlot, S., Tremonti, C., et al. Stellar masses and star formation histories for 10^5 galaxies from the Sloan Digital Sky Survey. MNRAS, 341:33–53, 2003a. doi:10.1046/j.1365-8711.2003.06291.x. `arXiv:astro-ph/0204055`.

—. The dependence of star formation history and internal structure on stellar mass for 10^5 low-redshift galaxies. MNRAS, 341:54–69, 2003b. doi:10.1046/j.1365-8711.2003.06292.x. `arXiv:astro-ph/0205070`.

Kauffmann, G., White, S. D. M., Heckman, T. M., Ménard, B., Brinchmann, J., et al. The environmental dependence of the relations between stellar mass, structure, star formation and nuclear activity in galaxies. MNRAS, 353:713–731, 2004. doi:10.1111/j.1365-2966.2004.08117.x. `arXiv:astro-ph/0402030`.

Kennicutt, R. C., Jr. Star Formation in Galaxies Along the Hubble Sequence. ARA&A, 36:189–232, 1998a. doi:10.1146/annurev.astro.36.1.189. `arXiv:astro-ph/9807187`.

—. The Global Schmidt Law in Star-forming Galaxies. ApJ, 498:541, 1998b. doi:10.1086/305588. `arXiv:astro-ph/9712213`.

Kennicutt, R. C., Jr., Hao, C.-N., Calzetti, D., Moustakas, J., Dale, D. A., et al. Dust-corrected Star Formation Rates of Galaxies. I. Combinations of H-alpha and Infrared Tracers. ApJ, 703:1672, 2009. doi:10.1088/0004-637X/703/2/1672. `0908.0203`.

Kirkpatrick, A., Pope, A., Alexander, D. M., Charmandaris, V., Daddi, E., et al. GOODS-Herschel: Impact of Active Galactic Nuclei and Star Formation Activity on Infrared Spectral Energy Distributions at High Redshift. ApJ, 759:139, 2012. doi:10.1088/0004-637X/759/2/139. `1209.4902`.

Kirkpatrick, A., Pope, A., Charmandaris, V., Daddi, E., Elbaz, D., et al. GOODS-Herschel: Separating High-redshift Active Galactic Nuclei and Star-forming Galaxies Using Infrared Color Diagnostics. ApJ, 763:123, 2013. doi:10.1088/0004-637X/763/2/123. `1212.2971`.

Knudsen, K. K., Barnard, V. E., van der Werf, P. P., Vielva, P., Kneib, J.-P., et al. An ultradeep submillimetre map: beneath the SCUBA confusion limit with lensing and robust source extraction. MNRAS, 368:487–496, 2006. `arXiv:astro-ph/0602131`.

Knudsen, K. K., van der Werf, P. P., and Kneib, J.-P. Probing the submillimetre number counts at $f_{850um} < 2$mJy. MNRAS, 384:1611–1626, 2008. doi:10.1111/j.1365-2966.2007.12820.x. `0712.1904`.

Kocevski, D. D., Lemaux, B. C., Lubin, L. M., Gal, R., McGrath, E. J., et al. Obscured Starburst Activity in High-redshift Clusters and Groups. ApJ, 736:38, 2011. doi:10.1088/0004-637X/736/1/38. `1009.2750`.

Kodama, T., Yamada, T., Akiyama, M., Aoki, K., Doi, M., et al. Down-sizing in galaxy formation at z˜ 1 in the Subaru/XMM-Newton Deep Survey (SXDS). MNRAS, 350:1005–1014, 2004. doi:10.1111/j.1365-2966.2004.07711.x. `arXiv:astro-ph/0402276`.

Koyama, Y., Kodama, T., Shimasaku, K., Hayashi, M., Okamura, S., et al. Panoramic Hα and mid-infrared mapping of star formation in a z = 0.8 cluster. MNRAS, 403:1611–1624, 2010. doi:10.1111/j.1365-2966.2009.16226.x. `0912.2786`.

Kravtsov, A. V. and Borgani, S. Formation of Galaxy Clusters. ARA&A, 50:353–409, 2012. doi:10.1146/annurev-astro-081811-125502. `1205.5556`.

Kroupa, P. On the variation of the initial mass function. MNRAS, 322:231–246, 2001. doi:10.1046/j.1365-8711.2001.04022.x. `arXiv:astro-ph/0009005`.

Kroupa, P., Tout, C. A., and Gilmore, G. The distribution of low-mass stars in the Galactic disc. MNRAS, 262:545–587, 1993.

Lacy, M., Storrie-Lombardi, L. J., Sajina, A., Appleton, P. N., Armus, L., et al. Obscured and Unobscured Active Galactic Nuclei in the Spitzer Space Telescope First Look Survey. ApJS, 154:166–169, 2004. doi:10.1086/422816. `arXiv:astro-ph/0405604`.

Lagache, G., Puget, J.-L., and Dole, H. Dusty Infrared Galaxies: Sources of the Cosmic Infrared Background. ARA&A, 43:727–768, 2005. doi:10.1146/annurev.astro.43.072103.150606. `arXiv:astro-ph/0507298`.

Landy, S. D. and Szalay, A. S. Bias and variance of angular correlation functions. ApJ, 412:64–71, 1993. doi:10.1086/172900.

Larson, R. B., Tinsley, B. M., and Caldwell, C. N. The evolution of disk galaxies and the origin of S0 galaxies. ApJ, 237:692–707, 1980. doi:10.1086/157917.

Le Floc'h, E., Papovich, C., Dole, H., Bell, E. F., Lagache, G., et al. Infrared Luminosity Functions from the Chandra Deep Field-South: The Spitzer View on the History of Dusty Star Formation at 0 ¡˜ z ¡˜ 1. ApJ, 632:169–190, 2005. doi:10.1086/432789. `arXiv:astro-ph/0506462`.

Leger, A. and Puget, J. L. Identification of the 'unidentified' IR emission features of interstellar dust? A&A, 137:L5–L8, 1984.

Leitherer, C. and Heckman, T. M. Synthetic properties of starburst galaxies. ApJS, 96:9–38, 1995. doi:10.1086/192112.

Li, I. H., Glazebrook, K., Gilbank, D., Balogh, M., Bower, R., et al. Dependence of star formation activity on stellar mass and environment from the Redshift One LDSS-3 Emission line Survey. MNRAS, 411:1869–1879, 2011. doi:10.1111/j.1365-2966.2010.17816.x. `1010.1447`.

Li, I. H., Yee, H. K. C., Hsieh, B. C., and Gladders, M. Evolution of Group Galaxies from the First Red-Sequence Cluster Survey. ApJ, 749:150, 2012. doi:10.1088/0004-637X/749/2/150. `1202.4767`.

Lidman, C., Iacobuta, G., Bauer, A. E., Barrientos, L. F., Cerulo, P., et al. The importance of major mergers in the build up of stellar mass in brightest cluster galaxies at z = 1. MNRAS, 433:825–837, 2013. doi:10.1093/mnras/stt777. `1305.0882`.

Lidman, C., Suherli, J., Muzzin, A., Wilson, G., Demarco, R., et al. Evidence for significant growth in the stellar mass of brightest cluster galaxies over the past 10 billion years. MNRAS, 427:550–568, 2012. doi:10.1111/j.1365-2966.2012.21984.x. `1208.5143`.

Lidman, C. E. and Peterson, B. A. An Optically Based Search for Distant Galaxy Clusters. AJ, 112:2454, 1996. doi:10.1086/118195.

Lilly, S. J., Eales, S. A., Gear, W. K. P., Hammer, F., Le Fèvre, O., et al. The Canada-United Kingdom Deep Submillimeter Survey. II. First Identifications, Redshifts, and Implications for Galaxy Evolution. ApJ, 518:641–655, 1999. doi:10.1086/307310. `arXiv:astro-ph/9901047`.

Lilly, S. J., Le Fevre, O., Hammer, F., and Crampton, D. The Canada-France Redshift Survey: The Luminosity Density and Star Formation History of the Universe to Z approximately 1. ApJ, 460:L1+, 1996. doi:10.1086/309975. `arXiv:astro-ph/9601050`.

Lilly, S. J., Le Fèvre, O., Renzini, A., Zamorani, G., Scodeggio, M., et al. zCOSMOS: A Large VLT/VIMOS Redshift Survey Covering 0 ¡ z ¡ 3 in the COSMOS Field. ApJS, 172:70–85, 2007. doi:10.1086/516589. `arXiv:astro-ph/0612291`.

Lonsdale, C. J., Smith, H. E., Rowan-Robinson, M., Surace, J., Shupe, D., et al. SWIRE: The SIRTF Wide-Area Infrared Extragalactic Survey. PASP, 115:897–927, 2003. doi:10.1086/376850. `arXiv:astro-ph/0305375`.

Lu, T., Gilbank, D. G., McGee, S. L., Balogh, M. L., and Gallagher, S. CFHT Legacy Ultraviolet Extension (CLUE): witnessing galaxy transformations up to 7 Mpc from rich cluster cores. MNRAS, 420:126–140, 2012. doi:10.1111/j.1365-2966.2011.20008.x. `1110.3336`.

Madau, P., Ferguson, H. C., Dickinson, M. E., Giavalisco, M., Steidel, C. C., et al. High-redshift galaxies in the Hubble Deep Field: colour selection and star formation history to z˜4. MNRAS, 283:1388–1404, 1996. `arXiv:astro-ph/9607172`.

Maddox, S. J., Dunne, L., Rigby, E., Eales, S., Cooray, A., et al. Herschel-ATLAS: The angular correlation function of submillimetre galaxies at high and low redshift. A&A, 518:L11, 2010. doi:10.1051/0004-6361/201014663. `1005.2406`.

Mahajan, S., Mamon, G. A., and Raychaudhury, S. The velocity modulation of galaxy properties in and near clusters: quantifying the decrease in star formation in backsplash galaxies. MNRAS, 416:2882–2902, 2011. doi:10.1111/j.1365-2966.2011.19236.x. `1106.3062`.

Mamon, G. A., Sanchis, T., Salvador-Solé, E., and Solanes, J. M. The origin of H I-deficiency in galaxies on the outskirts of the Virgo cluster. I. How far can galaxies bounce out of clusters? A&A, 414:445–451, 2004. doi:10.1051/0004-6361:20034155. `arXiv:astro-ph/0310709`.

Marchesini, D., van Dokkum, P. G., Förster Schreiber, N. M., Franx, M., Labbé, I., et al. The Evolution of the Stellar Mass Function of Galaxies from z = 4.0 and the First Comprehensive Analysis of its Uncertainties: Evidence for Mass-Dependent Evolution. ApJ, 701:1765–1796, 2009. doi:10.1088/0004-637X/701/2/1765. `0811.1773`.

Marriage, T. A., Acquaviva, V., Ade, P. A. R., Aguirre, P., Amiri, M., et al. The Atacama Cosmology Telescope: Sunyaev-Zel'dovich-Selected Galaxy Clusters at 148 GHz in the 2008 Survey. ApJ, 737:61, 2011. doi:10.1088/0004-637X/737/2/61. `1010.1065`.

Marsden, G., Ade, P. A. R., Bock, J. J., Chapin, E. L., Devlin, M. J., et al. BLAST: Resolving the Cosmic Submillimeter Background. ApJ, 707:1729–1739, 2009. doi:10.1088/0004-637X/707/2/1729. `0904.1205`.

Martini, P., Sivakoff, G. R., and Mulchaey, J. S. The Evolution of Active Galactic Nuclei in Clusters of Galaxies to Redshift 1.3. ApJ, 701:66–85, 2009. doi:10.1088/0004-637X/701/1/66. `0906.1843`.

McGee, S. L., Balogh, M. L., Bower, R. G., Font, A. S., and McCarthy, I. G. The accretion of galaxies into groups and clusters. MNRAS, 400:937–950, 2009. doi:10.1111/j.1365-2966.2009.15507.x. `0908.0750`.

Mehrtens, N., Romer, A. K., Hilton, M., Lloyd-Davies, E. J., Miller, C. J., et al. The XMM Cluster Survey: optical analysis methodology and the first data release. MNRAS, 423:1024–1052, 2012. doi:10.1111/j.1365-2966.2012.20931.x. `1106.3056`.

Ménard, B., Scranton, R., Fukugita, M., and Richards, G. Measuring the galaxy-mass and galaxy-dust correlations through magnification and reddening. MNRAS, 405:1025–1039, 2010. doi:10.1111/j.1365-2966.2010.16486.x. `0902.4240`.

Mihos, J. C. Morphology of galaxy mergers at intermediate redshift. ApJ, 438:L75–L78, 1995. doi:10.1086/187719.

Miller, G. E. and Scalo, J. M. The initial mass function and stellar birthrate in the solar neighborhood. ApJS, 41:513–547, 1979. doi:10.1086/190629.

Moore, B., Katz, N., Lake, G., Dressler, A., and Oemler, A. Galaxy harassment and the evolution of clusters of galaxies. Nature, 379:613–616, 1996. doi:10.1038/379613a0. `arXiv:astro-ph/9510034`.

Moore, B., Lake, G., and Katz, N. Morphological Transformation from Galaxy Harassment. ApJ, 495:139, 1998. doi:10.1086/305264. `arXiv:astro-ph/9701211`.

Moore, B., Lake, G., Quinn, T., and Stadel, J. On the survival and destruction of spiral galaxies in clusters. MNRAS, 304:465–474, 1999. doi:10.1046/j.1365-8711.1999.02345.x. `arXiv:astro-ph/9811127`.

Muzzin, A., Wilson, G., Demarco, R., Lidman, C., Nantais, J., et al. Discovery of a Rich Cluster at z = 1.63 using the Rest-Frame 1.6um "Stellar Bump Sequence" Method. *ArXiv e-prints*, 2013. `1301.5905`.

Muzzin, A., Wilson, G., Lacy, M., Yee, H. K. C., and Stanford, S. A. The Evolution of Dusty Star Formation and Stellar Mass Assembly in Clusters: Results from the IRAC 3.6, 4.5, 5.8, and 8.0 μm Cluster Luminosity Functions. ApJ, 686:966–994, 2008. doi:10.1086/591542. `0807.0227`.

Muzzin, A., Wilson, G., Yee, H. K. C., Gilbank, D., Hoekstra, H., et al. The Gemini Cluster Astrophysics Spectroscopic Survey (GCLASS): The Role of Environment and Self-regulation in Galaxy Evolution at z ˜ 1. ApJ, 746:188, 2012. doi:10.1088/0004-637X/746/2/188. `1112.3655`.

Muzzin, A., Wilson, G., Yee, H. K. C., Hoekstra, H., Gilbank, D., et al. Spectroscopic Confirmation of Two Massive Red-Sequence-Selected Galaxy Clusters at z ˜ 1.2 in the SpARCS-North Cluster Survey. ApJ, 698:1934–1942, 2009. doi:10.1088/0004-637X/698/2/1934. `0810.0005`.

Newman, A. B., Ellis, R. S., Andreon, S., Treu, T., Raichoor, A., et al. Spectroscopic Confirmation of the Rich z=1.80 Galaxy Cluster JKCS 041 Using the WFC3 Grism: Environmental Trends in the Ages and Structure of Quiescent Galaxies. *ArXiv e-prints*, 2013. `1310.6754`.

Nguyen, H. T., Schulz, B., Levenson, L., Amblard, A., Arumugam, V., et al. HerMES: The SPIRE confusion limit. A&A, 518:L5, 2010. doi:10.1051/0004-6361/201014680. `1005.2207`.

Noble, A. G., Geach, J. E., van Engelen, A. J., Webb, T. M. A., Coppin, K. E. K., et al. A submillimetre-bright z ˜ 3 overdensity behind a z ˜ 1 supercluster revealed by SCUBA-2 and Herschel. MNRAS, 436:L40–L44, 2013a. doi:10.1093/mnrasl/slt108. `1308.1119`.

Noble, A. G., Webb, T. M. A., Ellingson, E., Faloon, A. J., Gal, R. R., et al. Submillimetre source counts in the fields of high-redshift galaxy clusters. MNRAS, 419:1983–2013, 2012. doi:10.1111/j.1365-2966.2011.19854.x. `1109.5125`.

Noble, A. G., Webb, T. M. A., Muzzin, A., Wilson, G., Yee, H. K. C., et al. A Kinematic Approach to Assessing Environmental Effects: Star-forming Galaxies in a z ˜ 0.9 SpARCS Cluster Using Spitzer 24 μm Observations. ApJ, 768:118, 2013b. doi:10.1088/0004-637X/768/2/118. `1303.4997`.

Noeske, K. G., Weiner, B. J., Faber, S. M., Papovich, C., Koo, D. C., et al. Star Formation in AEGIS Field Galaxies since z=1.1: The Dominance of Gradually Declining Star Formation, and the Main Sequence of Star-forming Galaxies. ApJ, 660:L43–L46, 2007. doi:10.1086/517926. `arXiv:astro-ph/0701924`.

Nordon, R., Lutz, D., Shao, L., Magnelli, B., Berta, S., et al. The star-formation rates of 1.5 ¡ z ¡ 2.5 massive galaxies. A&A, 518:L24, 2010. doi:10.1051/0004-6361/201014621. `1005.1074`.

Oliver, S. J., Bock, J., Altieri, B., Amblard, A., Arumugam, V., et al. The Herschel Multi-tiered Extragalactic Survey: HerMES. MNRAS, 424:1614–1635, 2012. doi:10.1111/j.1365-2966.2012.20912.x. `1203.2562`.

Oliver, S. J., Wang, L., Smith, A. J., Altieri, B., Amblard, A., et al. HerMES: SPIRE galaxy number counts at 250, 350, and 500 μm. A&A, 518:L21, 2010. doi:10.1051/0004-6361/201014697. `1005.2184`.

Omont, A., Neri, R., Cox, P., Lupu, R., Guélin, M., et al. Observation of H_2O in a strongly lensed Herschel-ATLAS source at z = 2.3. A&A, 530:L3, 2011. doi:10.1051/0004-6361/201116921. `1107.4979`.

Ott, S. The Herschel Data Processing System — HIPE and Pipelines — Up and Running Since the Start of the Mission. In *Astronomical Data Analysis Software and Systems XIX*, volume 434 of *ASPCS*, page 139. 2010. `1011.1209`.

Page, M. J., Symeonidis, M., Vieira, J. D., Altieri, B., Amblard, A., et al. The suppression of star formation by powerful active galactic nuclei. Nature, 485:213–216, 2012. doi:10.1038/nature11096.

Paladini, R., Montier, L., Giard, M., Bernard, J. P., Dame, T. M., et al. A broadband study of galactic dust emission. A&A, 465:839–854, 2007. doi:10.1051/0004-6361:20065835. `astro-ph/0611606`.

Papovich, C., Dole, H., Egami, E., Le Floc'h, E., Pérez-González, P. G., et al. The 24 Micron Source Counts in Deep Spitzer Space Telescope Surveys. ApJS, 154:70–74, 2004. doi:10.1086/422880. `arXiv:astro-ph/0406035`.

Papovich, C., Momcheva, I., Willmer, C. N. A., Finkelstein, K. D., Finkelstein, S. L., et al. A Spitzer-selected Galaxy Cluster at z = 1.62. ApJ, 716:1503–1513, 2010. doi:10.1088/0004-637X/716/2/1503. `1002.3158`.

Partridge, R. B. and Peebles, P. J. E. Are Young Galaxies Visible? II. The Integrated Background. ApJ, 148:377, 1967. doi:10.1086/149161.

Patel, S. G., Holden, B. P., Kelson, D. D., Illingworth, G. D., and Franx, M. The Dependence of Star Formation Rates on Stellar Mass and Environment at z ˜ 0.8. ApJ, 705:L67–L70, 2009. doi:10.1088/0004-637X/705/1/L67. `0910.0837`.

Patel, S. G., Kelson, D. D., Holden, B. P., Franx, M., and Illingworth, G. D. The Star-formation-rate-Density Relation at 0.6 ¡ z ¡ 0.9 and the Role of Star-forming Galaxies. ApJ, 735:53, 2011. doi:10.1088/0004-637X/735/1/53. `1104.0934`.

Peeters, E., Spoon, H. W. W., and Tielens, A. G. G. M. Polycyclic Aromatic Hydrocarbons as a Tracer of Star Formation? ApJ, 613:986–1003, 2004. doi:10.1086/423237. `arXiv:astro-ph/0406183`.

Peng, Y.-j., Lilly, S. J., Kovač, K., Bolzonella, M., Pozzetti, L., et al. Mass and Environment as Drivers of Galaxy Evolution in SDSS and zCOSMOS and the Origin of the Schechter Function. ApJ, 721:193–221, 2010. doi:10.1088/0004-637X/721/1/193. `1003.4747`.

Pérez-González, P. G., Rieke, G. H., Villar, V., Barro, G., Blaylock, M., et al. The Stellar Mass Assembly of Galaxies from z = 0 to z = 4: Analysis of a Sample Selected in the Rest-Frame Near-Infrared with Spitzer. ApJ, 675:234–261, 2008. doi:10.1086/523690. `0709.1354`.

Pilbratt, G. L., Riedinger, J. R., Passvogel, T., Crone, G., Doyle, D., et al. Herschel Space Observatory. An ESA facility for far-infrared and submillimetre astronomy. A&A, 518:L1, 2010. doi:10.1051/0004-6361/201014759. `1005.5331`.

Planck Collaboration, Ade, P. A. R., Aghanim, N., Armitage-Caplan, C., Arnaud, M., et al. Planck 2013 results. XXIX. Planck catalogue of Sunyaev-Zeldovich sources. *ArXiv e-prints*, 2013. `1303.5089`.

Planck Collaboration, Ade, P. A. R., Aghanim, N., Arnaud, M., Ashdown, M., et al. Planck early results. I. The Planck mission. A&A, 536:A1, 2011. doi:10.1051/0004-6361/201116464. `1101.2022`.

Poggianti, B. M., Aragón-Salamanca, A., Zaritsky, D., De Lucia, G., Milvang-Jensen, B., et al. The Environments of Starburst and Post-Starburst Galaxies at z = 0.4-0.8. ApJ, 693:112–131, 2009. doi:10.1088/0004-637X/693/1/112. `0811.0252`.

Poggianti, B. M. and Barbaro, G. Indicators of star formation: 4000 Å break and Balmer lines. A&A, 325:1025–1030, 1997. `arXiv:astro-ph/9703067`.

Poggianti, B. M., Desai, V., Finn, R., Bamford, S., De Lucia, G., et al. The Relation between Star Formation, Morphology, and Local Density in High-Redshift Clusters and Groups. ApJ, 684:888–904, 2008. doi:10.1086/589936. `0805.1145`.

Poggianti, B. M., Smail, I., Dressler, A., Couch, W. J., Barger, A. J., et al. The Star Formation Histories of Galaxies in Distant Clusters. ApJ, 518:576–593, 1999. doi:10.1086/307322. `astro-ph/9901264`.

Poggianti, B. M. and Wu, H. Optical Spectral Signatures of Dusty Starburst Galaxies. ApJ, 529:157–169, 2000. doi:10.1086/308243. `astro-ph/9908180`.

Poglitsch, A., Waelkens, C., Geis, N., Feuchtgruber, H., Vandenbussche, B., et al. The Photodetector Array Camera and Spectrometer (PACS) on the Herschel Space Observatory. A&A, 518:L2, 2010. doi:10.1051/0004-6361/201014535. `1005.1487`.

Pope, A., Wagg, J., Frayer, D., Armus, L., Chary, R.-R., et al. Probing the Interstellar Medium of z ~ 1 Ultraluminous Infrared Galaxies through Interferometric Observations of CO and Spitzer Mid-infrared Spectroscopy. ApJ, 772:92, 2013. doi:10.1088/0004-637X/772/2/92. `1306.1831`.

Popesso, P., Magnelli, B., Buttiglione, S., Lutz, D., Poglitsch, A., et al. The effect of the high-pass filter data reduction technique on the Herschel PACS Photometer PSF and noise. *ArXiv e-prints*, 2012. `1211.4257`.

Postman, M., Lubin, L. M., Gunn, J. E., Oke, J. B., Hoessel, J. G., et al. The Palomar Distant Clusters Survey. I. The Cluster Catalog. AJ, 111:615, 1996. doi:10.1086/117811. `arXiv:astro-ph/9511011`.

Press, W. H. and Schechter, P. Formation of Galaxies and Clusters of Galaxies by Self-Similar Gravitational Condensation. ApJ, 187:425–438, 1974. doi:10.1086/152650.

Puget, J.-L., Abergel, A., Bernard, J.-P., Boulanger, F., Burton, W. B., et al. Tentative detection of a cosmic far-infrared background with COBE. A&A, 308:L5, 1996.

Quilis, V., Moore, B., and Bower, R. Gone with the Wind: The Origin of S0 Galaxies in Clusters. *Science*, 288:1617–1620, 2000. doi:10.1126/science.288.5471.1617. `arXiv:astro-ph/0006031`.

Regos, E. and Geller, M. J. Infall patterns around rich clusters of galaxies. AJ, 98:755–765, 1989. doi:10.1086/115177.

Reichardt, C. L., Stalder, B., Bleem, L. E., Montroy, T. E., Aird, K. A., et al. Galaxy Clusters Discovered via the Sunyaev-Zel'dovich Effect in the First 720 Square Degrees of the South Pole Telescope Survey. ApJ, 763:127, 2013. doi: 10.1088/0004-637X/763/2/127. `1203.5775`.

Rettura, A., Mei, S., Stanford, S. A., Raichoor, A., Moran, S., et al. Early-type Galaxies at z ~ 1.3. III. On the Dependence of Formation Epochs and Star Formation Histories on Stellar Mass and Environment. ApJ, 732:94, 2011. doi: 10.1088/0004-637X/732/2/94. `1103.0265`.

Rettura, A., Rosati, P., Nonino, M., Fosbury, R. A. E., Gobat, R., et al. Formation Epochs, Star Formation Histories, and Sizes of Massive Early-Type Galaxies in Cluster and Field Environments at z = 1.2: Insights from the Rest-Frame Ultraviolet. ApJ, 709:512–524, 2010. doi:10.1088/0004-637X/709/1/512. `0806.4604`.

Riechers, D. A., Walter, F., Carilli, C. L., Knudsen, K. K., Lo, K. Y., et al. CO(1-0) in z ¿ 4 Quasar Host Galaxies: No Evidence for Extended Molecular Gas Reservoirs. ApJ, 650:604–613, 2006. doi:10.1086/507014. `astro-ph/0606422`.

Rieke, G. H., Young, E. T., Engelbracht, C. W., Kelly, D. M., Low, F. J., et al. The Multiband Imaging Photometer for Spitzer (MIPS). ApJS, 154:25–29, 2004. doi:10.1086/422717.

Rodighiero, G., Cimatti, A., Gruppioni, C., Popesso, P., Andreani, P., et al. The first Herschel view of the mass-SFR link in high-z galaxies. A&A, 518:L25, 2010. doi:10.1051/0004-6361/201014624. `1005.1089`.

Romer, A. K., Viana, P. T. P., Liddle, A. R., and Mann, R. G. A Serendipitous Galaxy Cluster Survey with XMM: Expected Catalog Properties and Scientific Applications. ApJ, 547:594–608, 2001. doi:10.1086/318382.

Roseboom, I. G., Ivison, R. J., Greve, T. R., Amblard, A., Arumugam, V., et al. The Herschel Multi-tiered Extragalactic Survey: SPIRE-mm photometric redshifts. MNRAS, 419:2758–2773, 2012. doi:10.1111/j.1365-2966.2011.19827.x. `1109.2887`.

Rowan-Robinson, M. and Crawford, J. Models for infrared emission from IRAS galaxies. MNRAS, 238:523–558, 1989.

Saintonge, A., Tran, K.-V. H., and Holden, B. P. Spitzer/MIPS 24 μm Observations of Galaxy Clusters: An Increasing Fraction of Obscured Star-forming Members from z = 0.02 to z = 0.83. ApJ, 685:L113–L116, 2008. doi:10.1086/592730. `0806.2157`.

Sajina, A., Lacy, M., and Scott, D. Simulating the Spitzer Mid-Infrared Color-Color Diagrams. ApJ, 621:256–268, 2005. doi:10.1086/426536. `arXiv:astro-ph/0409597`.

Salim, S., Dickinson, M., Michael Rich, R., Charlot, S., Lee, J. C., et al. Mid-IR Luminosities and UV/Optical Star Formation Rates at z ¡ 1.4. ApJ, 700:161–182, 2009. doi:10.1088/0004-637X/700/1/161. `0905.0162`.

Salpeter, E. E. The Luminosity Function and Stellar Evolution. ApJ, 121:161, 1955. doi:10.1086/145971.

Savage, R. S. and Oliver, S. Bayesian Methods of Astronomical Source Extraction. ApJ, 661:1339–1346, 2007. doi:10.1086/515393. `arXiv:astro-ph/0512597`.

Sawicki, M. and Yee, H. K. C. Optical-Infrared Spectral Energy Distributions of z ¿ 2 Lyman Break Galaxies. AJ, 115:1329–1339, 1998. doi:10.1086/300291. `arXiv:astro-ph/9712216`.

Schade, D., Barrientos, L. F., and Lopez-Cruz, O. Evolution of Cluster Ellipticals at 0.2 ¡ Z ¡ 1.2 from Hubble Space Telescope Imaging. ApJ, 477:L17, 1997. doi:10.1086/310508. `arXiv:astro-ph/9612009`.

Schmidt, M. The Rate of Star Formation. ApJ, 129:243, 1959. doi:10.1086/146614.

Smail, I., Edge, A. C., Ellis, R. S., and Blandford, R. D. A statistical analysis of the galaxy populations of distant luminous X-ray clusters. MNRAS, 293:124–+, 1998. `arXiv:astro-ph/9707231`.

Smail, I., Ivison, R. J., and Blain, A. W. A Deep Sub-millimeter Survey of Lensing Clusters: A New Window on Galaxy Formation and Evolution. ApJ, 490:L5+, 1997. `arXiv:astro-ph/9708135`.

Smail, I., Ivison, R. J., Blain, A. W., and Kneib, J.-P. The nature of faint submillimetre-selected galaxies. MNRAS, 331:495–520, 2002. `arXiv:astro-ph/0112100`.

Sobral, D., Best, P. N., Smail, I., Geach, J. E., Cirasuolo, M., et al. The dependence of star formation activity on environment and stellar mass at z 1 from the HiZELS-Hα survey. MNRAS, 411:675–692, 2011. doi:10.1111/j.1365-2966.2010.17707.x. `1007.2642`.

Soifer, B. T., Helou, G., and Werner, M. The Spitzer View of the Extragalactic Universe. ARA&A, 46:201–240, 2008. doi:10.1146/annurev.astro.46.060407.145144.

Springel, V., White, S. D. M., Jenkins, A., Frenk, C. S., Yoshida, N., et al. Simulations of the formation, evolution and clustering of galaxies and quasars. Nature, 435:629–636, 2005. doi:10.1038/nature03597. `arXiv:astro-ph/0504097`.

Stanford, S. A., Brodwin, M., Gonzalez, A. H., Zeimann, G., Stern, D., et al. IDCS J1426.5+3508: Discovery of a Massive, Infrared-selected Galaxy Cluster at z = 1.75. ApJ, 753:164, 2012. doi:10.1088/0004-637X/753/2/164. `1205.3786`.

Stanford, S. A., Eisenhardt, P. R., Brodwin, M., Gonzalez, A. H., Stern, D., et al. An IR-selected Galaxy Cluster at z = 1.41. ApJ, 634:L129–L132, 2005. doi:10.1086/499045. `arXiv:astro-ph/0510655`.

Stasińska, G., Cid Fernandes, R., Mateus, A., Sodré, L., and Asari, N. V. Semi-empirical analysis of Sloan Digital Sky Survey galaxies - III. How to distinguish AGN hosts. MNRAS, 371:972–982, 2006. doi:10.1111/j.1365-2966.2006.10732.x. `arXiv:astro-ph/0606724`.

Stetson, P. B. DAOPHOT - A computer program for crowded-field stellar photometry. PASP, 99:191–222, 1987. doi:10.1086/131977.

Strateva, I., Ivezić, Ž., Knapp, G. R., Narayanan, V. K., Strauss, M. A., et al. Color Separation of Galaxy Types in the Sloan Digital Sky Survey Imaging Data. AJ, 122:1861–1874, 2001. doi:10.1086/323301. `arXiv:astro-ph/0107201`.

Surace, J. A., Shupe, D. L., Fang, F., Evans, T., Alexov, A., et al. Data Processing and Validation of the SWIRE Survey. In *American Astronomical Society Meeting Abstracts*, volume 37 of *Bulletin of the American Astronomical Society*, page 1246. 2005.

Tacconi, L. J., Genzel, R., Neri, R., Cox, P., Cooper, M. C., et al. High molecular gas fractions in normal massive star-forming galaxies in the young Universe. Nature, 463:781–784, 2010. doi:10.1038/nature08773. `1002.2149`.

Tacconi, L. J., Genzel, R., Smail, I., Neri, R., Chapman, S. C., et al. Submillimeter Galaxies at z ~ 2: Evidence for Major Mergers and Constraints on Lifetimes, IMF, and CO-H_2 Conversion Factor. ApJ, 680:246–262, 2008. doi:10.1086/587168. `0801.3650`.

Tamura, Y., Kohno, K., Nakanishi, K., Hatsukade, B., Iono, D., et al. Spatial correlation between submillimetre and Lyman-α galaxies in the SSA22 protocluster. Nature, 459:61–63, 2009. doi:10.1038/nature07947. `0905.0890`.

Tanaka, M., Finoguenov, A., and Ueda, Y. A Spectroscopically Confirmed X-ray Cluster at z = 1.62 with a Possible Companion in the Subaru/XMM-Newton Deep Field. ApJ, 716:L152–L156, 2010. doi:10.1088/2041-8205/716/2/L152. `1004.3606`.

Tielens, A. G. G. M. Interstellar Polycyclic Aromatic Hydrocarbon Molecules. ARA&A, 46:289–337, 2008. doi:10.1146/annurev.astro.46.060407.145211.

Tran, K.-V. H., Franx, M., Illingworth, G. D., van Dokkum, P., Kelson, D. D., et al. Field E+A Galaxies at Intermediate Redshifts (0.3 ¡ z ¡ 1). ApJ, 609:683–691, 2004. doi:10.1086/421237. `astro-ph/0403484`.

—. A Keck Spectroscopic Survey of MS 1054-03 (z = 0.83): Forming the Red Sequence. ApJ, 661:750–767, 2007. doi:10.1086/513738. `astro-ph/0702271`.

Tran, K.-V. H., Papovich, C., Saintonge, A., Brodwin, M., Dunlop, J. S., et al. Reversal of Fortune: Confirmation of an Increasing Star Formation-Density Relation in a Cluster at z = 1.62. ApJ, 719:L126–L129, 2010. doi:10.1088/2041-8205/719/2/L126. `1005.5126`.

Tran, K.-V. H., Saintonge, A., Moustakas, J., Bai, L., Gonzalez, A. H., et al. A Spectroscopically Confirmed Excess of 24 μm Sources in a Super Galaxy Group at z = 0.37: Enhanced Dusty Star Formation Relative to the Cluster and Field Environment. ApJ, 705:809–820, 2009. doi:10.1088/0004-637X/705/1/809. `0909.4079`.

Treu, T., Ellis, R. S., Kneib, J.-P., Dressler, A., Smail, I., et al. A Wide-Field Hubble Space Telescope Study of the Cluster Cl 0024+16 at z = 0.4. I. Morphological Distributions to 5 Mpc Radius. ApJ, 591:53–78, 2003. doi:10.1086/375314. `arXiv:astro-ph/0303267`.

van der Burg, R. F. J., Muzzin, A., Hoekstra, H., Lidman, C., Rettura, A., et al. The environmental dependence of the stellar mass function at z ˜ 1. Comparing cluster and field between the GCLASS and UltraVISTA surveys. A&A, 557:A15, 2013. doi:10.1051/0004-6361/201321237. `1304.5525`.

Vanderlinde, K., Crawford, T. M., de Haan, T., Dudley, J. P., Shaw, L., et al. Galaxy Clusters Selected with the Sunyaev-Zel'dovich Effect from 2008 South Pole Telescope Observations. ApJ, 722:1180–1196, 2010. doi:10.1088/0004-637X/722/2/1180. `1003.0003`.

Verheijen, M. A. W. The Ursa Major Cluster of Galaxies. V. H I Rotation Curve Shapes and the Tully-Fisher Relations. ApJ, 563:694–715, 2001. doi:10.1086/323887. `arXiv:astro-ph/0108225`.

Verley, S., Relaño, M., Kramer, C., Xilouris, E. M., Boquien, M., et al. Properties of compact 250 μm emission and H II regions in M 33 (HERM33ES). A&A, 518:L68, 2010. doi:10.1051/0004-6361/201014607.

Vieira, J. D., Marrone, D. P., Chapman, S. C., De Breuck, C., Hezaveh, Y. D., et al. Dusty starburst galaxies in the early Universe as revealed by gravitational lensing. Nature, 495:344–347, 2013. doi:10.1038/nature12001. `1303.2723`.

Viero, M. P., Ade, P. A. R., Bock, J. J., Chapin, E. L., Devlin, M. J., et al. BLAST: Correlations in the Cosmic Far-Infrared Background at 250, 350, and 500 μm Reveal Clustering of Star-forming Galaxies. ApJ, 707:1766–1778, 2009. doi:10.1088/0004-637X/707/2/1766. `0904.1200`.

Viero, M. P., Moncelsi, L., Quadri, R. F., Arumugam, V., Assef, R. J., et al. HerMES: The Contribution to the Cosmic Infrared Background from Galaxies Selected by Mass and Redshift. *ArXiv e-prints*, 2013. `1304.0446`.

Vulcani, B., Poggianti, B. M., Finn, R. A., Rudnick, G., Desai, V., et al. Comparing the Relation Between Star Formation and Galaxy Mass in Different Environments. ApJ, 710:L1–L6, 2010. doi:10.1088/2041-8205/710/1/L1. `0912.1180`.

Wagg, J., Pope, A., Alberts, S., Armus, L., Brodwin, M., et al. CO J = 2-1 Line Emission in Cluster Galaxies at z 1: Fueling Star Formation in Dense Environments. ApJ, 752:91, 2012. doi:10.1088/0004-637X/752/2/91. `1204.3897`.

Wardlow, J. L., Smail, I., Coppin, K. E. K., Alexander, D. M., Brandt, W. N., et al. The LABOCA survey of the Extended Chandra Deep Field-South: a photometric redshift survey of submillimetre galaxies. MNRAS, 415:1479–1508, 2011. doi:10.1111/j.1365-2966.2011.18795.x. `1006.2137`.

Webb, T. M., Eales, S. A., Lilly, S. J., Clements, D. L., Dunne, L., et al. The Canada-UK Deep Submillimeter Survey. VI. The 3 Hour Field. ApJ, 587:41–54, 2003. doi:10.1086/368109. `arXiv:astro-ph/0201180`.

Webb, T. M. A., O'Donnell, D., Yee, H. K. C., Gilbank, D., Coppin, K., et al. The Evolution of Dusty Star formation in Galaxy Clusters to z = 1: Spitzer Infrared Observations of the First Red-Sequence Cluster Survey. AJ, 146:84, 2013. doi:10.1088/0004-6256/146/4/84. `1304.3335`.

Werner, M. W., Roellig, T. L., Low, F. J., Rieke, G. H., Rieke, M., et al. The Spitzer Space Telescope Mission. ApJS, 154:1–9, 2004. doi:10.1086/422992. `arXiv:astro-ph/0406223`.

Wetzel, A. R., Tinker, J. L., and Conroy, C. Galaxy evolution in groups and clusters: star formation rates, red sequence fractions and the persistent bimodality. MNRAS, 424:232–243, 2012. doi:10.1111/j.1365-2966.2012.21188.x. `1107.5311`.

Wetzel, A. R., Tinker, J. L., Conroy, C., and van den Bosch, F. C. Galaxy evolution in groups and clusters: satellite star formation histories and quenching time-scales in a hierarchical Universe. MNRAS, 432:336–358, 2013. doi:10.1093/mnras/stt469. `1206.3571`.

White, S. D. M. and Frenk, C. S. Galaxy formation through hierarchical clustering. ApJ, 379:52–79, 1991. doi:10.1086/170483.

Wilson, G., Muzzin, A., Lacy, M., and FLS Survey Team. Detecting Clusters of Galaxies at High Redshift with the Spitzer Space Telescope. In L. Armus and W. T. Reach, editors, *Astronomical Society of the Pacific Conference Series*, volume 357 of *Astronomical Society of the Pacific Conference Series*, page 238. 2006. `arXiv:astro-ph/0503638`.

Wilson, G., Muzzin, A., Yee, H. K. C., Lacy, M., Surace, J., et al. Spectroscopic Confirmation of a Massive Red-Sequence-Selected Galaxy Cluster at z = 1.34 in the SpARCS-South Cluster Survey. ApJ, 698:1943–1950, 2009. doi:10.1088/0004-637X/698/2/1943. `0810.0036`.

Xu, C. Local Luminosity Function at 15 Microns and Galaxy Evolution Seen by ISOCAM 15 Micron Surveys. ApJ, 541:134–141, 2000. doi:10.1086/309401. `arXiv:astro-ph/0004216`.

Yee, H. K. C. A faint-galaxy photometry and image-analysis system. PASP, 103:396–411, 1991. doi:10.1086/132834.

Yee, H. K. C., Gladders, M. D., Gilbank, D. G., Majumdar, S., Hoekstra, H., et al. The Red-Sequence Cluster Surveys. In N. Metcalfe and T. Shanks, editors, *Cosmic Frontiers*, volume 379 of *Astronomical Society of the Pacific Conference Series*, page 103. 2007.

Yee, H. K. C. and López-Cruz, O. A Quantitative Measure of the Richness of Galaxy Clusters. AJ, 117:1985–1994, 1999. `arXiv:astro-ph/9902287`.

York, D. G., Adelman, J., Anderson, J. E., Jr., Anderson, S. F., Annis, J., et al. The Sloan Digital Sky Survey: Technical Summary. AJ, 120:1579–1587, 2000. doi:10.1086/301513. `arXiv:astro-ph/0006396`.

Zabludoff, A. I. and Mulchaey, J. S. The Properties of Poor Groups of Galaxies. I. Spectroscopic Survey and Results. ApJ, 496:39, 1998. doi:10.1086/305355. `arXiv:astro-ph/9708132`.

Zeimann, G. R., Stanford, S. A., Brodwin, M., Gonzalez, A. H., Snyder, G. F., et al. IDCS J1433.2+3306: An Infrared-selected Galaxy Cluster at z = 1.89. ApJ, 756:115, 2012. doi:10.1088/0004-637X/756/2/115. `1207.4793`.

Zwicky, F., Herzog, E., and Wild, P. *Catalogue of galaxies and of clusters of galaxies.* 1968.